2016

KINETICS OF MOLTEN METAL CAPILLARY FLOW IN NON-REACTIVE AND REACTIVE SYSTEMS

Hai Fu
University of Kentucky, hai.fu@uky.edu
Digital Object Identifier: http://dx.doi.org/10.13023/ETD.2016.163

STUDENT AGREEMENT:

I represent that my thesis or dissertation and abstract are my original work. Proper attribution has been given to all outside sources. I understand that I am solely responsible for obtaining any needed copyright permissions. I have obtained needed written permission statement(s) from the owner(s) of each third-party copyrighted matter to be included in my work, allowing electronic distribution (if such use is not permitted by the fair use doctrine) which will be submitted to UKnowledge as Additional File.

I hereby grant to The University of Kentucky and its agents the irrevocable, non-exclusive, and royalty-free license to archive and make accessible my work in whole or in part in all forms of media, now or hereafter known. I agree that the document mentioned above may be made available immediately for worldwide access unless an embargo applies.

I retain all other ownership rights to the copyright of my work. I also retain the right to use in future works (such as articles or books) all or part of my work. I understand that I am free to register the copyright to my work.

REVIEW, APPROVAL AND ACCEPTANCE

The document mentioned above has been reviewed and accepted by the student's advisor, on behalf of the advisory committee, and by the Director of Graduate Studies (DGS), on behalf of the program; we verify that this is the final, approved version of the student's thesis including all changes required by the advisory committee. The undersigned agree to abide by the statements above.

Hai Fu, Student

Dr. Dusan P. Sekulic, Major Professor

Dr. Haluk E. Karaca, Director of Graduate Studies

KINETICS OF MOLTEN METAL CAPILLARY FLOW IN NON-REACTIVE AND REACTIVE SYSTEMS

DISSERTATION

A dissertation submitted in partial fulfillment of the
requirements for the degree of Doctor of Philosophy in the
College of Engineering
at the University of Kentucky

By

Hai Fu

Lexington, Kentucky

Director: Dr. Dusan P. Sekulic, Professor of University of Kentucky

Co-Director: Dr. Kozo Saito, Professor of University of Kentucky

Lexington, Kentucky

2016

ABSTRACT OF DISSERTATION

KINETICS OF MOLTEN METAL CAPILLARY FLOW IN NON-REACTIVE AND REACTIVE SYSTEMS

Wetting and spreading of liquid systems on solid substrates under transient conditions, driven by surface tension and viscous forces along with the interface interactions (e.g., a substrate dissolution or diffusion and/or chemical reaction) is a complex problem, still waiting to be fully understood. In this study we have performed an extensive experimental investigation of liquid aluminum alloy spreading over aluminum substrate along with corroboration with theoretical modeling, performed in separate but coordinate study. Wetting and spreading to be considered take place during a transient formation of the free liquid surface in both sessile drop and wedge-tee mating surfaces' configurations. The AA3003 is used as a substrate and a novel self-fluxing material called Trillium^{TM} is considered as the filler metal. In addition, benchmark, non-reactive cases of spreading of water and silicon oil over quartz glass are considered. The study is performed experimentally by a high temperature optical dynamic contact angle measuring system and a standard and high speed visible light camera, as well as with infra read imaging. Benchmark tests of non-reactive systems are conducted under ambient environment's conditions. Molten metal experiment series featured aluminum and silicone alloys under controlled atmosphere at elevated temperatures. The chamber atmosphere is maintained by the ultra-high purity nitrogen gas purge process with the temperature monitored in real time *in situ*. Different configurations of the wedge-tee joints are designed to explore different parameters impacting the kinetics of the triple line movement process. Different power law relationships are identified, supporting subsequent theoretical analysis and simulation. Under ambient temperature conditions,

the non-reactive liquid wetting and spreading experiments (water and oil systems) were studied to verify the equilibrium triple line location relationships. The kinetics relationship between the dynamic contact angle and the triple line location is identified. Additional simulation and theoretical analysis of the triple line movement is conducted using the commercial computer software platform Comsol in a collaboration with a team from Washington State University within the NSF sponsored Grant #1235759 and # 1234581. The experimental work conducted here has been complemented by a verification of the Comsol phase-field modeling. Both segments of work (experimental and numerical) are parts of the collaborative NSF sponsored project involving the University of Kentucky and Washington State University. The phase field modeling used in this work was developed at the Washington State University and data are corroborated with experimental results obtained within the scope of this Thesis.

KEYWORDS: Kinetics, Wetting and Spreading, Wedge-tee, Trillium^{TM}, Model

Hai Fu

Apr. 15th, 2016

KINETICS OF MOLTEN METAL CAPILLARY FLOW IN NON-REACTIVE AND REACTIVE SYSTEMS

By

Hai Fu

Dr. Dusan P. Sekulic

Director of Dissertation

Dr. Kozo Saito

Co-Director of Dissertation

Dr.Haluk E. Karaca

Director of Graduate Studies

Apr. 15th, 2016

DEDICATION

DEDICATED TO MY PARENTS FOR SUPPORTING ME OVER THE YEARS UNCONDITIONALLY AND KENNETH TUBAUGH FOR STANDING BY MY SIDE THROUGH IT ALL

ACKNOWLEDGEMENTS

This dissertation and my PhD research work over the years were funded by multiple NSF projects. I want to thank my advisor Professor Dusan P. Sekulic for his generosity, resourceful insight and most of all, his kind support and encouragement. I would never have been able to finish my dissertation without his guidance and help. My deepest gratitude goes to Professor Dusan P. Sekulic for accepting me as his student when time was the hardest for me. The excellent research atmosphere in the ISM Brazing, Soldering and Heat Exchangers Research Laboratory will always be one of the best memories in my life.

I would like to thank my committee members, Dr. Kozo Saito, Dr. Y-T Cheng, Dr. Tianxiang Li and Dr. John Young, for their guidance and time during the defense process. Special thanks goes to Dr. Michael Winter for being willing for participating in my final defense committee at the last moment.

Many thanks to Dr. Mikhail Krivilev, Dr. Sinisa Mesarovic and Mohammad Dehsara for the continuous cooperation research in the NSF project. And many thanks to Dr. Fazleena Badurdeen, Dr. Robert Gregory, Dr. Margaret Schroder, Dr. Leslie Vincent, Dr. Gregory Luhan and Adam Brown for making the NSF funded course work a wonderful experience. Thanks to Dr. Doug Hawksworth and Daniel Busbaher for their support in the research work. Thanks to Dr. Haluk E. Karaca and his students Sayed M. Saghaian and Ali Turabi for allowing me to use his lab facilities to conduct several experiments. Thanks to Mechanical Engineering Department staff members, Charles Arvin, Heather-Michele Adkins, Peter Hayman and Steven Adkins, for their help and support during my PhD study.

Finally, I would like to thank my parents for being my parents with love and support no matter what. And I would like to thank Kenneth Tubaugh for being there for me through thick and thin.

TABLE OF CONTENTS

LIST OF TABLES

LIST OF FIGURES

CHAPTER 1: INTRODUCTION

1.1 Background Fundamentals

Surface tension driven flow has been studied both theoretically and experimentally for a long time (de Gennes, 1985; Voinov, 1976; Dussan, 1979.; Kistler, 1993; Eustathopoulos et al., 1999; Quéré, 2008; Bonn et al., 2009; Sui et al., 2014). The surface interactions play important role in many technologies. These include but are not restricted to oil recovery, pesticides deposition, water drainage, industrial cooling of reactors, etc. The associated phenomena manifest themselves at multiple scales, in microfluidics, nano-printing, coating technology, etc. Hence, they play an important role in almost every aspect of our lives, and are of key importance for many applications (Bonn et al., 2009).

Although the surface driven flow has been studied for a long time, only a limited number of high temperature studies were published before 1940s (Eustathopoulos et al. 1999). A new wave of wetting studies started to come out in the 1980s in the studies of metal joining, non-similar materials bonding, especially ceramic brazing and glazing (de Gennes, 1985; Eustathopoulos et al., 1999). In high temperature metal bonding, governed by the interfacial interactions, multiple parameters are relevant. These include constitutive species of the system, temperature, pressure, surface topography, background atmosphere, reaction processes, electric charges and gravity impact, among the others less dominant. The associated very complex phenomena are crucial to understanding of the structure, strength and durability of the bonded materials (Zhao et al., 2006; Busbaher et al., 2010).

In the brazing process, the materials involved are heated to temperatures above the filler metal melting temperature hence turning a solid metal into a liquid, forming the high temperature flow over the mating surfaces. Spreading of the liquid requires capillary action (Schwartz, 2003). The metallurgical bond is ultimately formed after solidification of the filler metal. The temperatures involved in brazing are, according to a widely adopted convention (Sekulic, 2013) above 450°C (liquidus temperature above 450°C but below the solidus temperature of the bonding metals, Schwartz, 2003).

In automotive industry and many aerospace applications, aluminum is normally preferred for its superior physical and economical properties over, say, copper. Motivated by these applications, this work focusses on aluminum alloy both used as mating surfaces substrates and filler metals. Associated materials processing require stringent processing conditions, including the liquid phase, imposed by novel designs of the components of engineering systems in those applications (Sekulic, 2011).

The kinetics of the molten metal flow has a direct impact on the solidified metal properties, notably strength and durability. The liquid metal wetting assumes often chemically inert atmosphere (as well as in a limit vacuum). Due to a high sensitivity in reaction of the involved materials, in particular at the elevated temperatures, formation of oxides is present. (Eustathopoulos et al. 1999). The oxide film formed during the process has to be eliminated to allow the free flow of the molten metal around the joint areas. For example, for high production rate joining of automobile heat exchanger assemblies, the Controlled Atmosphere Brazing (CAB) became the state-of-the-art manufacturing process (Sekulic, 2013). Furthermore, in various aerospace applications, vacuum brazing is a standard process. The low moisture level and drastically reduced oxygen level are

benefits of the desired atmosphere filled with inert gas (or vacuum) to ensure the controllable minimal oxidation layer formation on the surfaces of the metal. In controlled atmosphere traditionally, the molten metal at elevated temperatures is covered with a flux coating, so that the flux can react to disrupt the oxide film. Analogously, addition of a getter (Mg) in vacuum brazing serves a similar supporting role. Under this circumstance, the flux reaction at the elevated temperature in the controlled atmosphere can disrupt the aluminum oxide layer and provide the free flow of the molten metal, driven into the joint by the capillary force.

Recently, a novel aluminum alloy, Trillium^{TM} (US Patent US20100206529), was introduced. Trillium features the potassium fluoroaluminate flux imbedded into the solid filler (Hawksworth et al., 2012; Fu et al., 2013; Yu et al., 2013; Sekulic, 2013). This "fluxless" brazing (actually an absence of the flux coating) achieves the same or better results than the traditional brazing with a flux, and decreases the complexity and expenses at the same time (Sekulic, 2013). In this dissertation, the kinetics of the joint formation involving this material is the subject of this study.

It is well understood that the kinetics of the wetting process is controlled by factors like temperature, atmosphere composition, surface properties, reaction rates, in addition to the materials systems properties. Controlling different variables to study the kinetics process helps better understand of the brazing process, hence getting ultimately a better quality of brazing. The interest of the study is to analyze and understand the kinetics of the wetting processes in brazing aluminum. Both, reactive (molten aluminum on aluminum) and non-reactive systems (water and silicon oil on glass) were considered.

1.2 Scope of the research

Wetting and spreading of liquid systems on solid substrates under transient conditions, driven by surface tension and retarded by viscosity, under both non-reactive and reactive conditions at liquid/solid interface are being investigated. The study was performed experimentally and is supported by theoretical modeling simultaneously developed by a collaborating team. Wetting and spreading to be considered takes place during a transient formation of the free liquid surface in a so called wedge-tee configuration, using AA3003 metal as a substrate. In addition, non-reactive benchmark cases of spreading of water and silicon oil over quartz glass as a substrate were considered. Measurements were obtained by using a high temperature optical dynamic contact angle measuring system equipped by both low and high speed visible light and infra-red cameras. Benchmark tests of non-reactive systems were be conducted under ambient environment's conditions. In a high temperature reactive (or more precisely, a weak-reactive) molten metal liquid experiment series, aluminum and silicone alloys were used. The atmosphere was controlled by the ultra-high purity nitrogen gas purge process with the temperature monitored in real time *in situ*. Different configurations of the wedge-tee joints are designed to explore the different parameters impacting the kinetics of the triple line movement process. Power law relationships are identified in the experiments, supporting the subsequent theoretical analysis and simulation. The set of non-reactive liquid wetting and spreading experiments has been performed at the ambient temperatures. Water and silicon oil systems were studied to verify the contact angles equilibrium triple line location relationships. The kinetics between the dynamic contact angle and the triple line location relation was

identified. An empirical best fit model was determined for benchmarking the high temperature reactive wetting and spreading tests.

Additional simulation and theoretical analysis of the triple line movement prediction were performed.

The main objectives of the study were to explore, explain, model and ultimately understand the dynamics of the wetting process in both reactive and non-reactive systems and at both high and low temperatures. The main research hypothesis of the experimental work is that a novel liquid metal (Al-Si eutectic + $K_xF_yAl_z$) spreading kinetics, driven by surface tension, can be modeled by a Washburn type correlation (power law), regardless of the reactive nature of the solid-liquid substrate.

1.3 Organization of the dissertation

Following the introduction in Chapter 1, Chapter 2 reviews the literature involving the fundamental knowledge and most recent research related to the non-reactive, and reactive surface tension driven wetting and spreading on smooth surfaces. High temperature wetting, especially in brazing will also be reviewed.

As a benchmark study, the capillary flow of the non-reactive liquid systems is studied experimentally. Two material systems: water and silicone oil are considered in Chapter 3.

Chapter 4 introduces the high temperature brazing experimental facility, namely the Optical Contact Angle analyzer (OCA), as well as specific procedures that were adopted for different experiments for the near reactive surface driven capillary molten metal flow on different wetting surfaces.

Chapter 5 explores the weak-reactive surface driven capillary flow of the molten metal on the wetting surface. The specific wedge-tee joint configuration, topographically similar to the non-reactive experiment configuration, is introduced in the experiments to study the reaction impacted triple line kinetics. Different power law relationships have been discovered in different stages of the process.

A similar configuration of wedge-tee joint with a non-wetting horizontal surface is presented in Chapter 6 to further explore the reactive capillary flow kinetics of the molten metal. The method of surface tension measurement of the molten metal on the non-wetting surface is also introduced in this chapter.

Conclusion and further discussion of the results are presented in Chapter 7, with future research objectives as well as existing problems presented in the last chapter.

In the Appendices section, Appendix A discusses the error analysis from the benchmark experiments. Appendix B extends the molten clad metal wetting on the non-wetting surface with the measurement of surface tension of the molten clad metal. Appendix C gives the review of aluminum alloy surface tension in the known literature to compare with the measured molten clad metal surface tension. Appendix D quantifies the meniscus curvature of the wedge-tee joint area from molten clad metal. Appendix E includes the phase field model discussion, physical parameters, phase field model parameters and the steps to determine the parameters.

CHAPTER 2: LITERATURE REVIEW

2.1 Overview

Related research on the scope of this dissertation is reviewed in this chapter. A broader view of the wetting phenomenon in general is discussed here.

The literature is grouped into two parts. The first part summarizes the research on the non-reactive surface tension driven flow at low temperatures, including the brief presentation of fundamental theories of the wetting and spreading. The approach to the basic experimental methods for the study of wetting and spreading is addressed. Different theoretical models for the non-reactive spreading are presented in this part. The second part of the literature review provides the controlled atmosphere brazing optical contact angle analyzer furnace description used for design of the high temperature experimental methods for surface tension driven flow. The text offers a review of relevant studies on surface tension driven flow at elevated temperatures for reactive flows. Finally, the aluminum brazing process related joint formation featuring interaction between the filler metal and substrate is covered in this part as well. The introduction of some fundamental concepts in this review is not intended to be either complete or rigorous. Such reviews are available (De Gennes, 1985) and would not be repeated here. Rather, only key concept relevant for this study will be summarized.

2.2 Wetting and spreading

Wetting phenomenon is one of the basic physical phenomena in nature. As stated by de Gennes (1985), the wetting of a solid is based on physical chemistry which involves the concept of wettability, including the interpretation of surface forces as van der Waals forces and fluid dynamics. Spreading of a liquid is the ultimate result of wetting of the liquid (Myers, 1999). Wetting and spreading implies an involvement of chemistry, physics and engineering insights (Bonn et al., 2009). The surface chemistry is the key factor influencing the wetting and spreading phenomena (Bonn et al., 2009). Along with surface chemistry, surface forces like van der Waals and electrostatic forces are also controlling the wetting and spreading phenomena in general (Bonn et al., 2009). Application of wetting and spreading are numerous and span from painting, lubrication, dye and printing up to oil industry, power generation, biochemical deposition of pesticides, skin care, etc. In recent years, wetting and spreading phenomena applications in designing super hydrophobic surfaces has triggered an increasing interest, leading to such applications as self-cleaning, nanofluidics, and electro-wetting (Yuan et al., 2013).

2.2.1 The Concept of Contact Angle

Contact angle is one of the major physical entities in any study of wetting and spreading processes. It represents a quantitative measure of the wetting process. When a drop of liquid contacts a solid surface, the liquid either spreads more or less unconstraint across the surface to form a thin film, or spreads to a limited extent to form a drop (e.g., sessile drop) on the surface (Myers, 1999). Contact angle as a wetting metric indicates the degree of wetting. For example, it is well known that if the contact angle, say θ, is larger

than 90°, the surface is considered as a wetting surface; if the contact angle θ is less than 90°, the surface is considered as non-wetting surface. More specifically, a partially wetting can be attributed to the surface/liquid couples featuring contact angles between 30° to 89°. The contact angle considered here is referring to the so called apparent contact angle, as opposed to the dynamic contact angle. The contact angle of the liquid on the other condensed phases is the primary characteristics of any immiscible, two or three phase system containing two condensed phases (Myers, 1999). The contact angle can be defined as the angle between two planes tangent to the liquid and solid surfaces geometrically, see Fig. 2.1.

Fig. 2.1 Contact angle concept schematics

2.2.2 Dynamic contact angle

The contact angle that was mentioned above is the equilibrium contact angle. Before the liquid spreading reaches its equilibrium state, the contact angle featured by the progressing front is the dynamic contact angle. Depending on the moving direction, e.g., if the liquid is advancing across the surface, the dynamic contact angle is equal to the advancing contact angle θ_A; if the liquid is receding from the wetted surface, the contact angle is the receding contact angle θ_R. The apparent contact angle (θ) is less than θ_A but

larger than θ_R, see Fig. 2.2. It is found that in the dynamic systems, θ_A and θ_R would vary depending on the velocity of the wetting line, with θ_A increasing applied by smaller velocity and θ_R decreasing applied by larger velocity (Blake et al., 1973; Johnson et al., 1977; Rillaerts et al., 1980; Seebergh et al., 1992; Myers, 1999). The dynamic contact angle is apparently relevant to the dynamic process of the wetting and spreading. The phenomenon associated with the difference between the advancing contact angle and the receding contact angle is called hysteresis and can be measured by the difference in contact angles (H), see Fig. 2.2. The hysteresis increases with surface roughness, and/or surface heterogeneity (Blake et al., 1973; Joanny et al., 1984; Yuan et al., 2013):

$$H = \theta_A - \theta_R \tag{2.1}$$

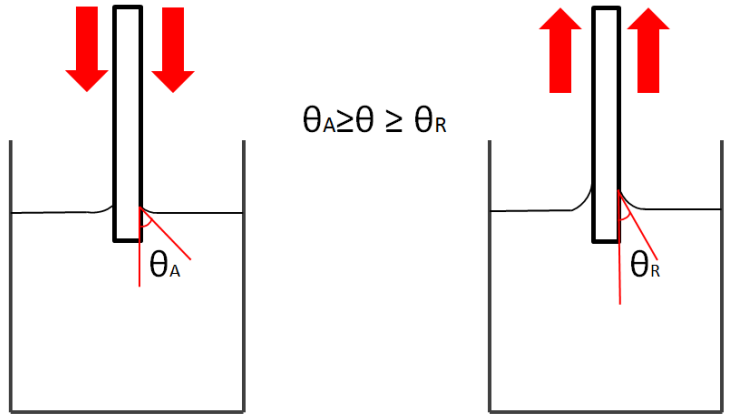

Fig. 2.2 Advancing contact angle (left) and receding contact angle (right) comparison

The contact angle hysteresis is one of the most important phenomena involving wetting of a liquid droplet system (Eral et al., 2013).

2.2.3 Triple line location (TLL)

The triple line location, namely three-phase zone or three-phase contact line (TCL), is the location where solid, liquid and the gas phases meet.

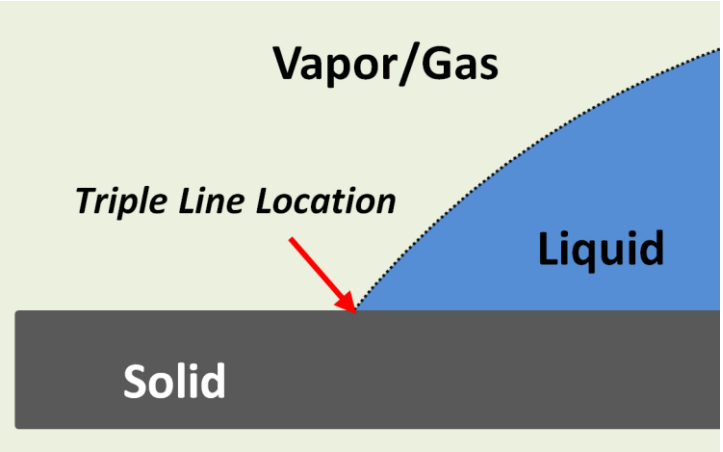

Fig. 2.3 Triple line location schematics

2.2.4 Surface energy and Young's equation

Surface tension is caused by the unbalanced forces of liquid molecules at the surface of the liquid (Yuan et al., 2013), and it is interpreted as an intermolecular force. It's well known (Myers, 1999; Bonn et al., 2009) that if a drop of liquid is placed on a smooth flat surface, it will spread and most likely form a contact angle eventually. In the equilibrium state, three different phases presented will form a balance with surface tensions of solid-liquid, liquid-gas and solid-gas, see Fig.2.4. The balance is given by Young's equation (Young, 1805) as:

$$\gamma_{SV} = \gamma_{SL} + \gamma_{LV} \cos\theta \tag{2.2}$$

where γ_{SV} is the surface energy, also known as surface tension at the solid vapor interface, γ_{SL} is the surface energy at the solid liquid interface, and γ_{LV} is the surface tension at the vapor liquid surface. The surface energy is an energy per unit area, equivalent to a force per unit length acting on the contact line (Bonn et al., 2009)

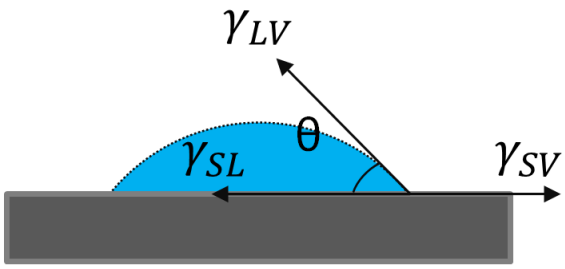

Fig. 2.4 Force balance of the three-phase contact line

Based on Young's equation, if $\gamma_{SV} < \gamma_{SL} + \gamma_{LV}$, a partial wetting can be observed; if $\gamma_{SV} = \gamma_{SL} + \gamma_{LV}$, a complete wetting with contact angle being zero can be achieved. Although the thermodynamic definition of the contact angle and surface energies are provided by Young's equation, γ_{SV} and γ_{SL} cannot be determined directly from experiments (Myers, 1999).

2.2.5 Capillary number, capillary length and Bond number

The dimensionless number, the Capillary number (*Ca*), is the ratio of viscous to surface energy, expressed as:

$$Ca = U\eta/\gamma_{LV} \tag{2.3}$$

where U is the moving speed of the contact line, also known as triple line, and η is the dynamic viscosity of the liquid. When $Ca \ll 1$, the spreading of the liquid is dominated by

the surface tension rather than the viscous effects. Bonn et al. (2009) shows that, in that case, $Ca \approx 10^{-5} - 10^{-3}$. Capillary length, however, is the ratio of surface tension to gravitational force, expressed as:

$$l_c = \sqrt{\gamma_{LV}/\rho g} \tag{2.4}$$

Note that when the drop radius is smaller than the capillary length, gravity can be neglected (Bonn et al., 2009).

Another dimensionless number to measure the importance of surface tension and the body force is known as Bond number or Eötvös number ($Bo = \frac{\Delta\rho g L^2}{\gamma_{LV}}$, where $\Delta\rho$ is the two phases of liquid or gas density difference, L is is the characteristic length) (Hager, 2012).

2.3 Experimental evidence of non-reactive wetting and spreading

The dynamics of the surface driven flow has been studied for over a century and much of the study was focused mostly on ambient temperature and non-reactive liquid systems. Back in the early 20th century, by using capillary tube of uniform internal circular cross-section throughout, Washburn (1921) has studied the kinetics of capillary flow of mercury, water and oil systems, and presented the Washburn type of flow with liquid penetration distance obeying the square root relationship to time. Compared to the spontaneous, natural wetting and spreading, for the forced wetting, the apparent dynamic contact angle has been the focus of the research (Kistler, 1993). The distinction between the two will be explained below, see Section 2.3.2. Common experimental methods for the forced wetting case include sessile drop configuration and the capillary displacement

configuration (Washburn, 1921; Tanner, 1979; Šikalo et al., 2005; Han et al., 2014), and Wilhelmy plate configuration or wetting-balance method (Johnson et al., 1977; Ström et al., 1990). The contact angles can be directly measurement as the tangent angle at the triple line contact point by a contact angle goniometer (Yuan et al., 2013). Alternately, they may be determined by a measurement of the tangent angle at the triple line contact point from the extracted images from a video camera (Han et al., 2014). The liquid systems in the studies mostly involve, as mentioned earlier, water, mercury, oils and organic chemical compounds. Based on the experimental data, the dynamic contact angle $\theta_D$can be correlated with the triple line movement kinetics, mostly represented by the capillary number *Ca* (Kistler, 1993).

2.3.1 Sessile drop experiments

One of the most common experimental studies of the surface tension driven flow is the sessile drop setup, see Fig.2.1. In this type of setup, the liquid drop is placed on a horizontal surface, so that the drop can spread over the surface due to the surface tension force. Different roughness of the surfaces can be used in these tests to study the surface topography impact on the spreading. The dynamic contact angle, equilibrium contact angle and the triple line movement can all be recorded. There are many studies regarding this form of testing with different liquid systems (Schwartz et al., 1972; Tanner, 1979; Hocking et al., 1982; Biance et al., 2004; Lee et al., 2011). The dominating force presented on the spreading is an inertial force and the surface tension during the dynamic phase of the process. The drops can be generated by a syringe, either with/without the automatic dispenser (Yuan et al., 2013). A microscope with either CMOS camera, CCD camera or high speed camera is used to record the images of the spreading process, so

that the contact angles and triple line movement can be measured through an image of a drop's profile, interpreted as the cross-section region of the sessile drop. Such tests are mostly done at ambient temperature, under constant pressure.

2.3.2 Capillary displacement experiments

The capillary displacement method for a surface tension driven flow dynamic study is also commonly used as testified by the studies in the past decades (Washburn, 1921; Rillaerts et al., 1980; Fermigier et al., 1991; Kistler, 1993; Sobolev et al., 2000), see Fig. 2.5.

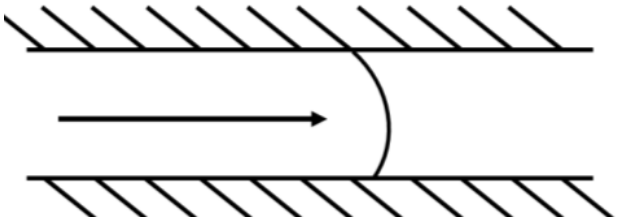

Fig. 2.5 Capillary displacement measurement of apparent contact angle (Kistler, 1993)

In this type of setup, since the capillary tube is of the order of several millimeters or micrometers or even smaller, gravity and inertial effects can be neglected. Thus the dominating force is the surface tension type of capillary force. This type of experiment can either be a spontaneous, natural spreading (Stokes et al., 1990; Calvo et al., 1991) or forced spreading (Fermigier et al., 1991), depending on whether the liquid is being pumped through the tubes. In the natural spreading method, two reservoirs are connected by a capillary tube (Calvo, 1991), thus the pressure difference in two reservoirs will push the liquid through the tube. If the radius compared to the reservoir radius is rather small, then the liquid variation in location and speed, in the tube can be neglected. Capillary

displacement experiments are similar to the sessile drop experiments in a way that the microscope with camera and liquid dispenser with syringe can also be used. If the spreading is a forced spreading, then pumps can be used to pump liquid through the capillary tubing. With the aid of microscope and camera, the images of each action in the spreading process can be recorded, thus the contact angles and the triple line movement can be measured.

According to Washburn (1921), for the vertical capillaries, the capillary spontaneous natural rise, h, can be calculated as:

$$h = \frac{2\gamma_{LV}\cos\theta}{\Delta\rho g r} \tag{2.5}$$

where r is the capillary radius, g is the gravitational acceleration, $\Delta\rho$ is the density difference between liquid and vapor, θ is the equilibrium contact angle, and γ_{LV} is the surface tension between liquid and vapor.

For the horizontal capillaries, a similar correlation can be found as:

$$l^2 = \frac{rt\gamma_{LV}\cos\theta}{2\eta} \tag{2.6}$$

where l is the capillary distance, r is capillary radius, η is the liquid viscosity, θ is the equilibrium contact angle, γ_{LV} is the surface tension between liquid and vapor, and t is the time required for the capillary intrusion.

2.3.3 Wilhelmy plate balance experiments

In the forced spreading experiments, the Wilhelmy plate configuration (Wilhelmy, 1863) is very common , see Fig. 2.2 and Fig.2.6.

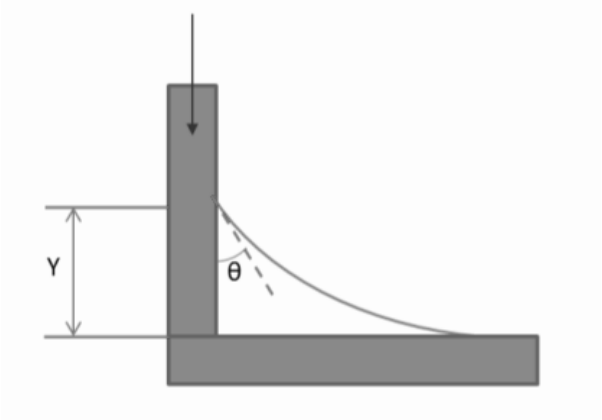

Fig. 2.6 Wilhelmy plate configuration

The contact angle can be measured on a solid plate surface with both advancing contact angle and receding contact angle. When a vertical plate is intruding the liquid pool, a balance can detect weight change of the pool. The detected force is a combination of buoyancy and wetting (Yuan et al., 2013). From force balance, we can have the following equation:

$$F = \gamma_{LV} p \cos\theta_D - V\Delta\rho g \tag{2.7}$$

where F is the force combination of wetting and buoyancy, γ_{LV} is the surface tension between liquid and vapor, p is the perimeter of contact line, θ_D is the dynamic contact angle, g is the gravitational acceleration, $\Delta\rho$ is the density difference between liquid and vapor, and V is the displaced liquid volume.

If the plate stops moving (see Fig. 2.2), when the kinetics of the wetting process completes by reaching the equilibrium for the triple line, based on Laplace equation (Cain, 1983), the equilibrium contact angle can be determined from the capillary rise on the vertical plate as:

$$sin\,\theta = 1 - \frac{\Delta\rho g y^2}{2\gamma_{LV}} \tag{2.8}$$

where θ is the equilibrium contact angle, g is the gravitational acceleration, $\Delta\rho$ is the density difference of the liquid and vapor, y is the capillary rise height, γ_{LV} is the surface tension between liquid and vapor.

The Wilhelmy plate balance method is a fairly accurate method widely used to determine the dynamic contact angle and the relationship between the dynamic contact angle and the wetting speeds. It should be noted that a sufficient quantity of liquid should be used to avoid the impact of the liquid level change approaching the equilibrium.

Based on the Wilhelmy plate balance method, a combined advancing and receding contact angle measurement method can be established as the plunge tank method (Kistler, 1993), as seen in Fig. 2.7.

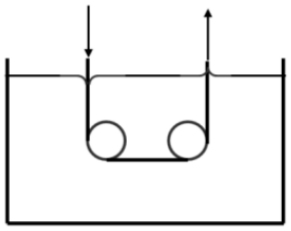

Fig. 2.7 Plunge tank configuration (Kistler, 1993)

The continuous strand of plastic film is moving in and out of the liquid reservoir. The type of configuration is convenient to measure the dynamic contact angle and wetting speed relationship (Bracke, 1989) based on the force that is applied on the film.

2.3.4 Tilting plate experiments

Adam (1925) developed the tilting plate method to measure the contact angle relatively simply but accurately. In this method, a solid plate is placed in the liquid pool to form the meniscus on both sides of the plate. The plate is tilted slowly until the meniscus on one side of the plate becomes horizontal, see Fig.2.8. The angle between the plate and the horizontal liquid surface is the contact angle of interest.

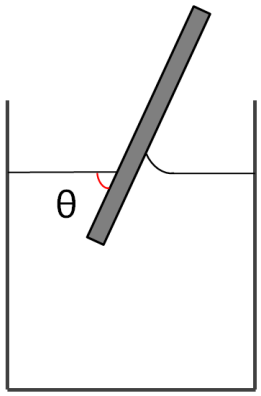

Fig. 2.8 Tilting plate method configuration

As the configuration suggests, due to the fact that the contact angle needs to be measured when it's stable, the measure contact angle is only equilibrium contact angle. Microscopes are normally used to measure the contact angle (Fowkes et al., 1940). The accuracy of the measured contact angle can be further improved by applying scanning laser beams of ray tracing (Smedley et al., 2005). In the improved method, the velocity and dynamic contact angle correlation can be determined.

2.3.5 Capillary bridge experiments

Vagharchakian et al. (2008) and Restagno et al. (2009) developed the capillary bridge method to measure the contact angle. In this method, a transparent convex surface (such as a watch glass) with a radius of curvature R of a few centimeters is used on a liquid bath with test liquid. The meniscus forms at the contact line around the curvature of the spherical surface. By measuring the changes of the wetted area and the distance between the surface and the liquid, the dynamic contact angle can be determined based on Young's equation. The capillary bridge method offers the way to measure both advancing and receding contact angle with precise results (Vagharchakian et al., 2008; Retsgno et al., 2009). However, due to the high sensitivity of the method, liquid evaporation may impose negative impact on the accuracy of the results.

2.4 Non-reactive wetting kinetics models

The kinetics of the liquid spreading has been studied over the past decades, as emphasized in the opening sections of this chapter. It is suggested (Kistler, 1993) based on dimensional analysis that the dynamic contact angle, θ_D, should be related to the contact angle, θ, capillary number, Weber number We ($We = \frac{\rho U^2 L_c}{\gamma}$, L_c is characteristic length), Bond number Bo ($Bo = \frac{\Delta \rho g L_c^2}{\gamma}$), viscosity ratio, density ratio, species L, and surface properties (such as roughness ε, porosity ξ and electric charges χ).

$$\theta_D = f\left(\theta, Ca, We, Bo, \frac{\mu_2}{\mu_1}, \frac{\rho_2}{\rho_1}, \frac{L_i}{L}, \varepsilon, \xi, \chi\right) \tag{2.9}$$

Two different approaches to the wetting modeling the kinetics of spreading on a solid surface deserve our attention. One is the hydrodynamic model (Seebergh et al., 1992). Let us assume, based on the scaling implied by Eq. (2.9), that the surface tension and viscosity are the dominant forces. The other approach is the molecular-kinetic model, focusing on the behavior/interactions of liquid and the solid molecules (Eral et al., 2013).

In the hydrodynamic models, an important variable is the wetting velocity *U*, (Hoffman et al., 1975). Also, wetting is characterized by the contact angle. The variation of the contact angle with respect to time or wetting velocity reflects the kinetics of the wetting process.

Most of the kinetics models are based on the correlation between contact angle, dynamic contact angle and the wetting velocity. As shown in Eq. (2.3), wetting velocity can also be represented by the capillary number relationship, as $Ca = U\eta/\gamma_{LV}$. Washburn (1921) developed the correlations of triple line movement kinetics, see Eq. (2.5) and Eq. (2.6). In the 70s, Hoffman et al. (1975), Voinov et al. (1976) and Tanner (1979) have presented the Hoffman-Voinov-Tanner law, describing the empirical correlation between contact angles and wetting velocity. Later experiments have verified this correlation in different forms, such as Jiang's model (Jiang et al., 1979), Bracke's model (Bracke et al., 1989), Seebergh's model (Seebergh et al., 1992), etc.

2.4.1 Hoffman-Voinov-Tanner law

Hoffman (1975) first brought up the correlation between the experimental data by plotting the contact angle and the capillary number for low capillary numbers, measured via capillary displacement measurement. 5 different liquids were used in his experiment.

It should be noted that the kinetics process is dominated by the interfacial and viscous forces. Voinov (1976) also demonstrated that for a small Reynolds number, there is a dependence of the contact angle on wetting velocity. It wasn't until Tanner (1979) who derived the $\theta_D \sim Ca^{1/3}$ power law hydrodynamic theory correlation based on his experiments. The correlation, *Hoffman-Voinov-Tanner Law*, has been formulated as follows.

$$\theta_D^3 - \theta^3 = c_T Ca \tag{2.10}$$

Where c_T is a constant based on the solid-vapor-liquid selection, θ_D is the dynamic contact angle, and θ is the equilibrium contact angle. In order to apply the law correctly, the capillary number has to be much smaller than 1, and $\theta_D \leq 135°$. It also has be noted that the liquids tested in this interpretation are the oil-based liquids, such as silicone oil. The correlation between dynamic contact angle and the capillary number is independent of the measurement configuration (Kisler, 1993).

2.4.2 Jiang's Correlation Model

Based on Hoffman et al. (1975) experiment data, the fitting correlation between contact angle and the capillary number was presented by Jiang et al. (1979), Eq. (2.11). The correlation was also applied to other systems, Schwartz et al. (1970).

$$\frac{cos\,\theta - cos\,\theta_D}{cos\,\theta + 1} = tanh(4.96 Ca^{0.702}) \tag{2.11}$$

It should be noted the Jiang's correlation model is a different form of *Hoffman-Voinov-Tanner Law*, with the dominant forces being still surface tension and viscosity. The

correlation was verified with other sources of experiment data, as long as $Bo < 10^{-1}$ and $We < 10^{-3}$where

$$Bo = \frac{\rho g L^1}{\gamma_{LV}} \tag{2.12}$$

$$We = \frac{\rho U^2 L}{\gamma_{LV}} \tag{2.13}$$

The Bond number, *Bo*, is the ratio of gravity to interfacial forces, and the Weber number, *We*, is the ratio of inertial forces to interfacial forces at the liquid-gas interface; *L* is the characteristic length, *U* is the wetting velocity. Based on the empirical results, it is known that if inertia and gravity are negligible, Jiang's correlation model would be valid for different liquid-gas-solid systems.

2.4.3 Bracke's Correlation Model

Based on his own experiment data, Bracke et al. (1989) obtained the equation as follows.

$$\frac{\cos\theta - \cos\theta_D}{\cos\theta + 1} = 2Ca^{0.5} \tag{2.14}$$

The Wilhelmy plate configuration was used in Bracke's experiment to obtain the date of θ_D and *U*. The correlation model was also verified with other experiments data source from different measurement configurations with different organic liquid systems. Bracke confirms Eq. (2.14) as well as Eq. (2.10) is comparable for small capillary numbers. It is also presented that the correlation is applicable for clean and dry plates as the rate of wetting is much faster for the prewetted plate. Similar to Jiang's model, Bracke's model shows the correlation is valid for small Bo number when the gravity effect can be ignored.

The model can also be applied for small drop spreading on a solid, as verified with experiments from other sources (Bracke, 1989).

2.4.4 Seebergh's Correlation Model

The previous empirical correlation models are limited by the capillary number, namely they are valid for $Ca < 0.01$. The universal function can be expressed as:

$$H = \frac{\cos\theta - \cos\theta_D}{\cos\theta + 1} = ACa^B \tag{2.15}$$

For low and high capillary numbers, Hoffman's data deviate from the models presented by Jiang et al. (1979). By studying the acid-based experiments, Seebergh et al. (1992) obtained a more universal correlation model as:

$$\frac{\cos\theta - \cos\theta_D}{\cos\theta + 1} = 2.24Ca^{0.54};\ 10^{-3} \leq Ca < 0.01 \tag{2.16}$$

$$\frac{\cos\theta - \cos\theta_D}{\cos\theta + 1} = 4.47Ca^{0.42};\ Ca \leq 10^{-3} \tag{2.17}$$

It is noticed that for the larger capillary number regime, Seeburgh's model is comparable to Bracke's model. However, as the capillary number reduces, different constants are used to fit the experiment data.

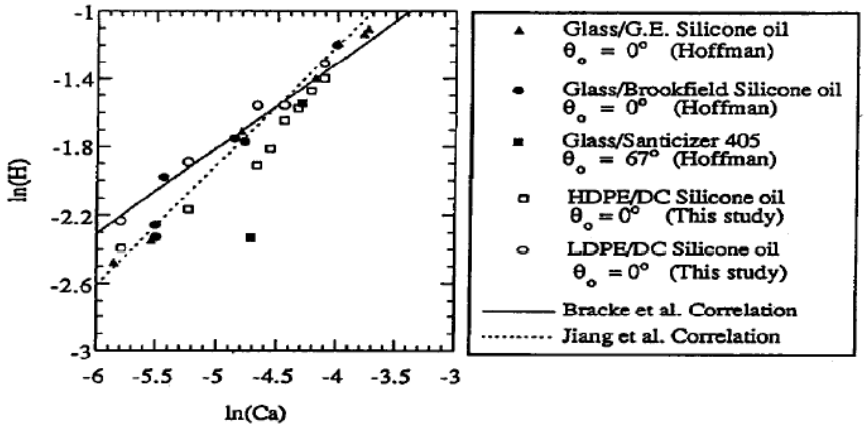

(a)

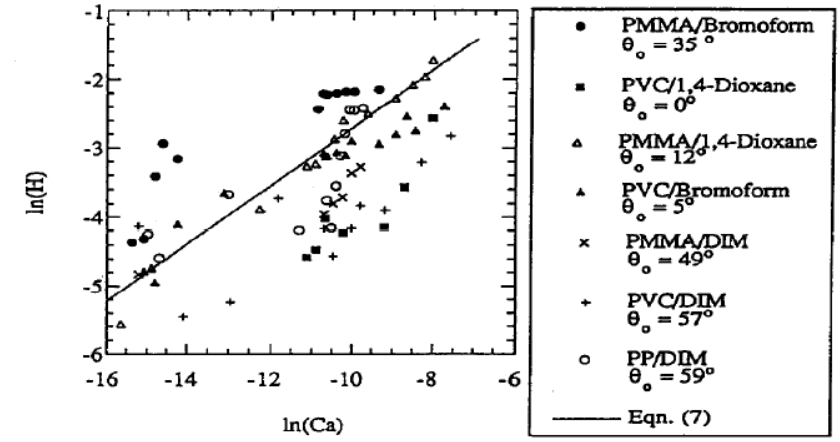

(b)

Fig. 2.9 (a) Comparison between empirical correlations and Hoffman's data for $Ca > 10^{-3}$ (Seebergh et al., 1992), (b) Comparison between Seeburgh's model and all the low capillary number data (Seebergh et al., 1992)

2.4.5 Blake's Molecular Model

By applying the molecular kinetic theory, ignoring the hydrodynamic effects such as viscous dissipation near the wetting line (Blake et al., 1995), the molecular-kinetic

models take the solid-surface characteristics into account. In this type of model, the contact line motion is determined by the statistical dynamics of the molecules at the triple line location (Eral et al., 2013). Two important fitting parameter factors are introduced here: κ^0, the equilibrium frequency of the random molecular displacements occurring at the triple line location, and λ, the average distance between the adsorption/desorption sites on the solid surface, see Equ. (2.18 and 2.19). It is assumed that the dynamic contact angle velocity is depending on the disturbance of the liquid adsorption equilibrium and the changes in the local surface tension when the wetting line moves across the solid surface (Eral et al., 2013). Therefore, the driving force for the triple line motion is expressed as:

$$F_w = \gamma_{LV}(cos\,\theta - cos\,\theta_D) \tag{2.18}$$

The resulting from the driving force relationship between contact angle and the wetting velocity is:

$$U(\theta) = 2\kappa^0\lambda\,\sinh[\,\gamma_{LV}(cos\,\theta - cos\,\theta_D)\lambda^2/2k_BT] \tag{2.19}$$

where k_B is the Boltzmann constant, and T is the absolute temperature. Eq. (2.19) can also be expressed as:

$$cos\,\theta_D = cos\,\theta - \frac{2k_BT}{\gamma_{LV}\lambda^2}sinh^{-1}(\frac{U}{2\kappa^0\lambda}) \tag{2.20}$$

2.5 Near-reactive (molten metal) case: CAB Technology description

Liquid metal wetting and spreading is essential for many technological processes, e.g., spreading of the solder/braze over/between the substrate materials. It is customary to

specify that the contact angle must be below 90° for metal bonding (Eustathopoulos et al., 1999). The triple line movement, defined as a movement of the locus of points between solid-liquid-gas phases, is the central phenomenon in the manifestation of the kinetics of a wetting process in liquid metal systems. The mechanical strength and durability of a solder/braze joint directly rely on the wetting and spreading kinetics process over the mating surfaces that precede solidification. The wetting (the ability of a liquid to maintain contact with a solid surface) and spreading (the ability of a liquid to spread on another liquid or solid) processes in the liquid metal systems mostly involve reactive interaction across the liquid/solid interface, and the kinetics of the process is not only a function of viscosity, density, species composition, surface properties, such as roughness, porosity and electric charges, but also of diffusion, dissolution, convection, deoxidation, and interfacial reaction (Eustathopoulos et al., 1999; Meier et al., 1999; Saiz et al., 1998; Contreras et al., 2003; Meier et al., 1998; Rado et al., 2000). The empirical models are established in most cases by fitting experimental data on triple line movement distance as a function of time $r(t)$ (Mortensen et al., 1997; Bailey et al., 1951; Li et al., 1992), or time dependent contact angle $\theta(t)$ (Dezellus et al., 2002). Common experimental methods are known as sessile drop experiments, wetting balance technique (Eustathopoulos et al., 1999) and hot stage microscopy experiments (Thorsen et al., 1984). In the manufacturing process, in order to prevent the formation of the oxide layers on the surface of liquid metals, inert gaseous environment is generally required in the process setups. For aluminum brazing, the wetting in the inert gaseous (usually nitrogen) environment is known as the controlled atmosphere brazing process (CAB process). Figure 2.10 offers an illustration of the CAB facility used in this study.

Fig. 2.10 Transparent high temperature CAB laboratory furnace system

To accomplish the CAB process, the aluminum surface is normally deposited with a layer of flux consisting of potassium fluoro-aluminate compounds ($KAlF_4$) to break down the aluminum oxide layer, so that the molten clad metal driven by the capillary force can be drawn into the joint area (Zhao, 2005). Certain other criteria have to be met for the CAB process. These include primarily: (i) the oxygen content in the controlled atmosphere has to be lower than 100 ppm and (ii) the dew point less than -40°C (Zhao, 2005). In contrast to the CAB, in the vacuum-brazing technology, Mg is added in the clad alloy and/or exposed to the background vacuum atmosphere (Mg as “getter”) so that the evaporated magnesium at elevated temperatures can interfere with the formation of the oxide layers on the molten metal. Although the flux could be eliminated in the vacuum-brazing process, the requirement for the specialized vacuum equipment imposes a higher demand which increases the cost and maintenance. Thanks to the CAB technology, production savings are possible for mass production manufacturers, and the CAB technology is

considered as the state-of-the-art manufacturing process for high-volume mass production of most automobile heat exchanger assemblies process (Sekulic, 2013). This is the reason why this material system and this materials processing technology are considered in this work. So, the CAB technology can achieve the continuous flow for the high volume at lower costs with less limits on the dimensions of the product, see Fig. 2.11.

Fig. 2.11 CAB continuous production line (SECO/WARWICK GROUP, http://www.secowarwick.com/en/products/cab-controlled-atmosphere-brazing-furnaces/ (accessed on Sept.5th, 2015))

As the brazing technology is evolving, flux loadings have been reduced for the CAB process. Self-fluxing (that is, flux is not eliminated but it is added to the clad, (Ogilvy et al., 2014)) brazing of aluminum has also currently being developed some earlier solutions in this direction were also subject of development and applications (James G et al., 1968;

Humpston et al., 1995), but will not be considered here. By adopting the self-fluxing technology, the cost and maintenance for CAB process technology can be further reduced, making the CAB play an even more important role in the growing market for brazed aluminum condensers in the heating, ventilation, air conditioning and refrigeration sector (Sekulic, 2013). By modifying the brazing sheet, clad metal and flux material compositions, the self-fluxing material has been developed by Sapa Group (Ogilvy et al., 2014). Three different brazing systems have been considered in our work: 1. Surface-modified brazing sheet; 2. Filler (clad) metal alloy modifications and 3. Composite filler (clad) metal-flux materials (Sekulic, 2013). The surface-modified brazing systems are close to the traditional systems where the flux is applied to the components. Ogilvy et al. (2014) has produced the self-fluxing composite filler metal-flux materials by spray forming the composite that can be further fabricated into a liner plate for cladding onto brazing sheet. The alloy used is a eutectic Al-Si filler with finely dispersed flux particles within the alloy matrix. Sapa AB and Sandvik Osprey invented this metal matrix composite consisting of a eutectic aluminum-silicon alloy within which small particles of potassium alumino-fluoride salt are dispersed (Sekulic, 2013; Ogilvy et al., 2014). The use of the composite materials for brazing is registered as Trillium^{TM} Technology (Sekulic, 2013). At elevated temperatures, the added salt melts within the molten metal clad (Fig. 2.12). The fluxing action is initiated from within the clad layer and acts on the interface between the clad and the oxide. The fluxing activity starts when the clad filler metal starts to melt and the molten salt segregates towards the surface. Before the melting, the oxide prevents the flux from reacting with the atmosphere and other surface contaminants. After melting, the molten flux disrupts and/or detaches the oxide from the

clad to allow the molten clad to wet and spread and flow into the void spaces by surface tension force to form the joints upon cooling. The differential scanning calorimetry tests indicate the salt endotherm of 550°C (Sekulic, 2013; Ogilvy et al., 2014) while the eutectic of aluminum-silicon alloy endotherm of 577°C (Sekulic, 2013; Ogilvy et al., 2014).

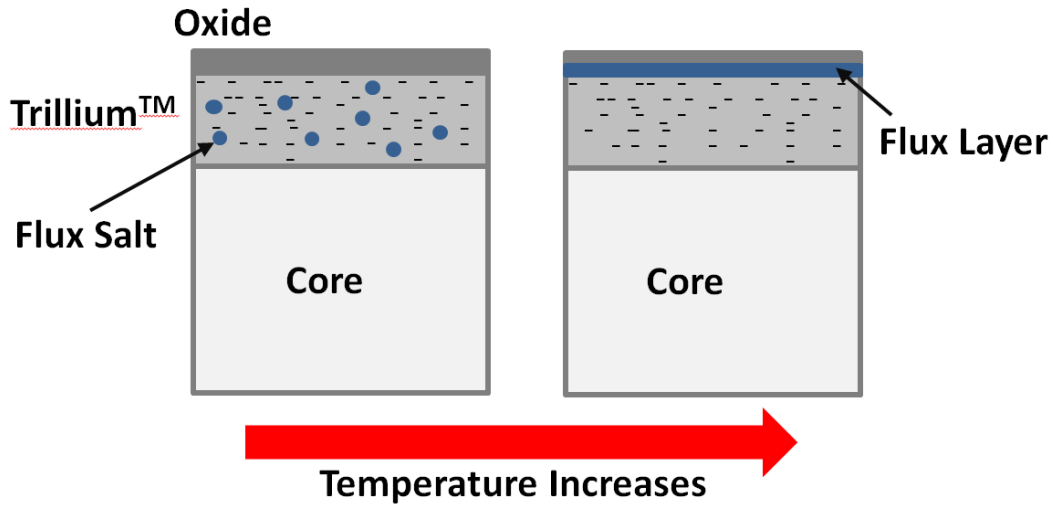

Fig. 2.12 Schematic of composite-clad brazing sheet (Trillium™) brazing process

It is reported (Yu et al, 2013) that the Trillium™ clad brazing sheet has much greater resilience to increased oxygen levels and humidity content than traditional clad brazing sheet coated with brazing flux.

2.5.1 Sessile drop experiment

The sessile drop experiment is a simple and most common method to study the wetting behavior at elevated temperatures for both reactive and non-reactive systems. In general,

the experiment is designed to permit a drop of liquid to spread over a horizontal solid substrate until the equilibrium state is reached, see Fig. 2.13.

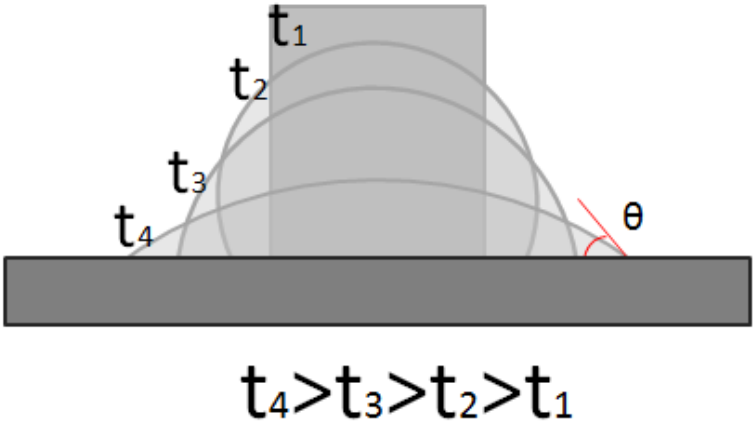

Fig. 2.13 Schematic of the profiles as the solid cube melts to wet and spread during the sessile drop experiment

The rate of the liquid front (triple line location) advances over the substrate is the characteristic of the kinetics of the liquid metal wetting to study. Liquid surface tension γ_{LV} can also be evaluated from the sessile drop experiments (Keene et al., 1993; Anson et al., 1999, Fu et al., 2013). To measure the accurate contact angle, smaller sizes of the drops are recommended, while the surface tension measurement requires larger drops so that the gravitational force would have impact on the shape of the drop. For the sessile drop experiment, different forms of the experiment setups could apply, but the common requirements include the horizontal stage, a furnace chamber to provide either vacuum or controlled atmosphere condition, heating facility and the measurement facility (Eustathopoulos, 1999). In order to prevent the oxide layer formation at the elevated temperature, the test furnace chamber normally is gas tight, so that the chamber can be

purged with inert gas or be vacuumed to required level. The common inert gases purged include helium, nitrogen or argon, and the oxygen level contained is normally lower than 20 ppm. Hydrogen gas might be mixed in the inert gas to further reduce the oxide layer formation. As mentioned earlier, as long as the key requirement is met for the sessile drop experiment, different forms of setups can achieve the same goal to measure triple line growth, contact angles or surface tensions, see Fig. 2.14.

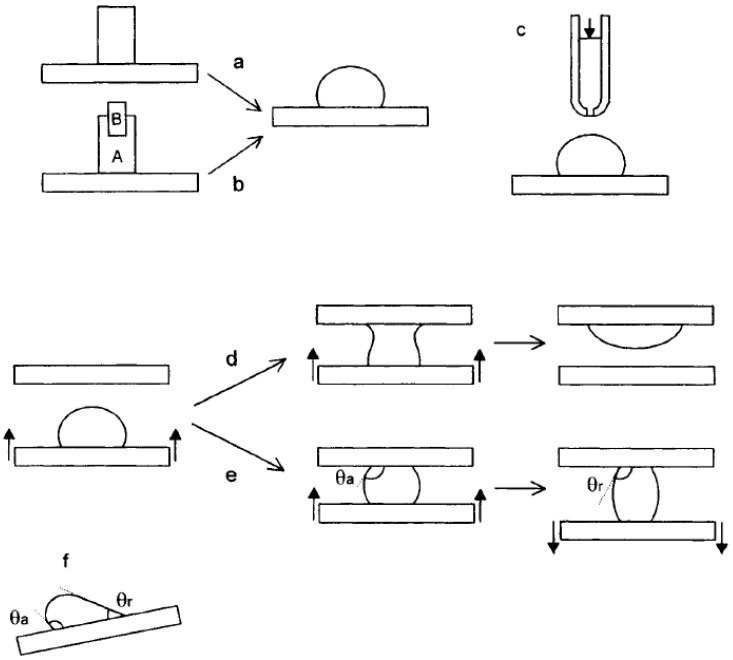

Fig. 2.14 Methods of sessile drop experiments: (a) traditional method, (b) *in situ* formation of the alloy, (c) dispensed drop, (d) transferred drop, (e) double substrate, (f) tilted plate (Eustathopoulos et al., 1999)

A typical sessile drop experimental setup is shown in Fig. 2.15 of the boron nitride and molten aluminum system and Fig. 2.16 of aluminum wetting on sapphire. An optical

contact angle analyzer with the furnace is also a typical sessile drop experiment setup (Fu et al., 2013; Fu et al., 2016), see Section 4.2 in this thesis manuscript for more details.

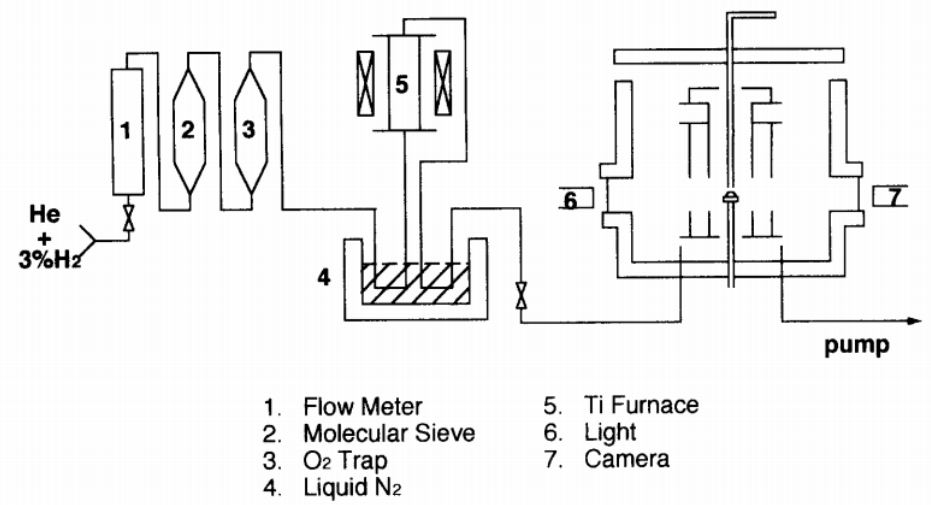

Fig. 2.15 Sessile drop experiment setup schematic diagram for the boron nitride and molten aluminum system (Fujii et al., 1993)

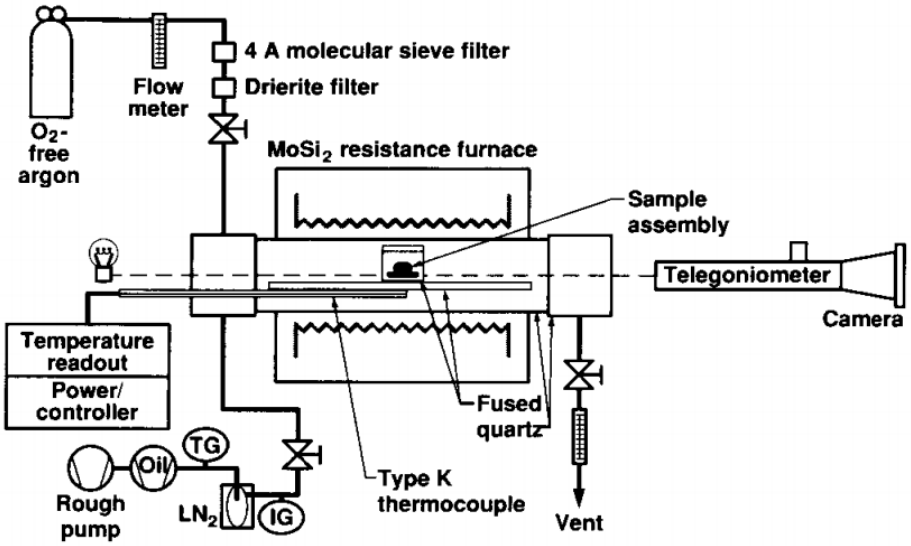

Fig. 2.16 Sessile drop experiment setup schematic diagram for aluminum wetting on sapphire (Weirauch et al., 1990)

The spherical drop volume v can be calculated based on the following equation (Eustathopoulos et al., 1999) :

$$v = \frac{\pi R^3}{3} \frac{(2-3cos\theta+cos^3\theta)}{sin^3\theta} \tag{2.21}$$

where *R* is the radius of the drop, θ is the contact angle.

Since R has to be measure after the experiment is completed, alternatively, one can also use the Bashforth and Adams tables (1883) to calculate the volume as:

$$v = \pi R^2 \left(\frac{2b}{\beta} - \frac{2b^2 sin\theta}{x_{90}\beta} + H\right);$$

$$\beta = \frac{b^2 \rho g}{\gamma_{LV}} \tag{2.21}$$

where H is the drop height, ρ is the liquid density, g is the gravitational force, γ_{LV} is the surface tension and x_{90} is the constant from Bashforth and Adams tables.

The wetting kinetics can be presented from the sessile drop experiments by measuring the triple line locations and time relationships (Fu et al., 2013; Fu et al., 2016). Further discussion will be made in later chapters.

2.5.2 Wetting balance experiment

The wetting balance experiment is referring to the pulling or inserting an object into the liquid surface to measure the surface tension (Eustathopoulos et al., 1999), corresponding the Wilhelmy plate configuration in the non-reactive experiments. As was described by Chappius et al. (1982), the wetting balance method consists of continuously monitoring the force acting on a solid, cylinder or blade, moving into and out of a liquid bath during

an immersion-emersion cycle (Eustathopoulos et al., 1999). High temperature study apparatus was developed by Rivollet et al. (1990), see Fig. 2.17.

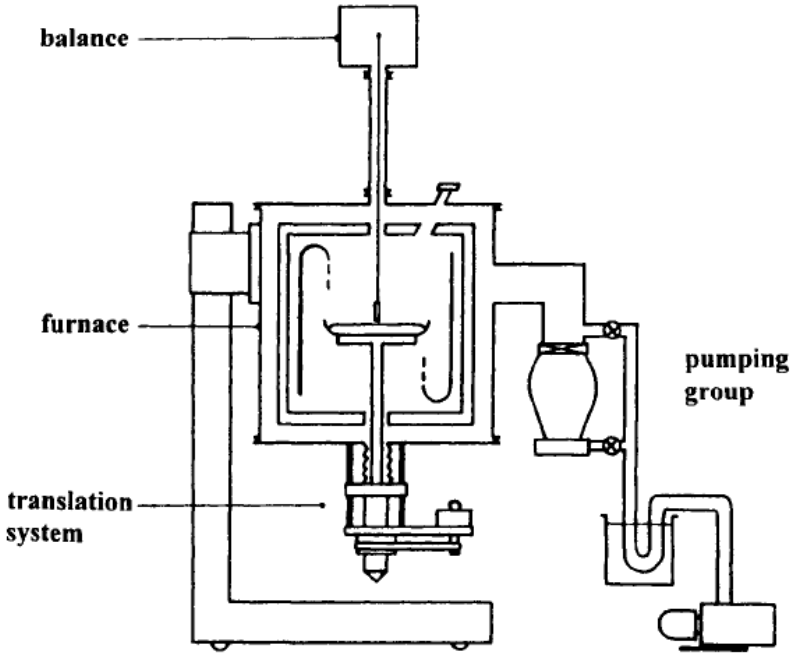

Fig. 2.17 Schematic diagram of the wetting balance experiment (Rivollet et al., 1990)

The experimental setup consists of a furnace chamber, a pumping system, a translation system providing the displacement of the crucible at a constant rate and the electronic microbalance. This method allows the simultaneous measurement of the surface tension of the liquid and the contact angles. Both advancing and receding contact angles can be measured from the immersion and emersion process. It is recommended the force inserted into the liquid to be "infinitely" slow, so that the force *f* is equal to the weight of the meniscus and the buoyancy force:

$$f = w_m + \Omega \rho g z_b;$$

$$w_m = P\gamma_{LV} \cos\varphi \tag{2.22}$$

where w_m is the weight of the meniscus, Ω is the solid base area, ρ is the liquid density, g is the gravitational acceleration, P is the liquid base perimeter, φ is the joining angle of the liquid meniscus on the solid surface, defined by the tangent to the liquid surface at the triple line location (Eustathopoulos et al., 1999), γ_{LV} is the surface tension and z_b is the solid based height from the liquid horizontal surface of the liquid. It should be noted that $\emptyset$ is only equal to contact angles at certain points when the force is in and out of the liquid process, referring to the immersion-emersion curve f(z_b) (Eustathopoulos et al., 1999), namely, when the solid is completely into the liquid, $\emptyset$ is equal to the contact angles, see Fig.2.18. The wetting balance technique is not only used as a method to measure the dynamic contact angles, but also as a method to study the liquid kinetics of the spreading.

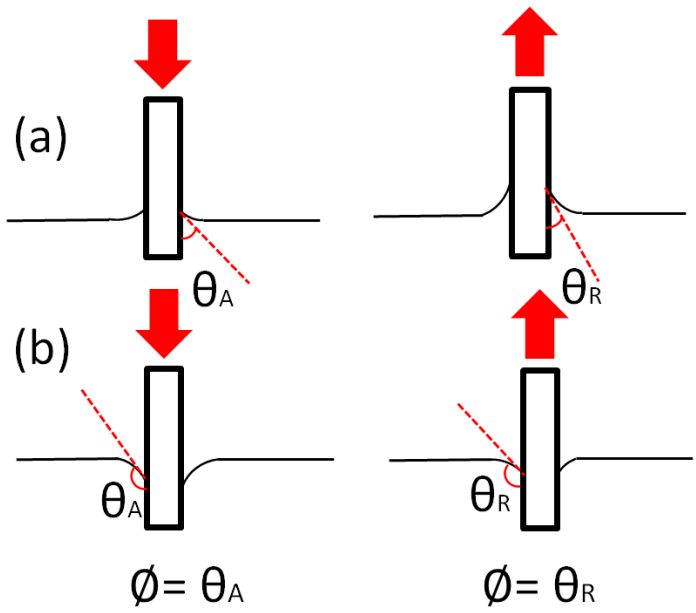

Fig. 2.18 Schematic diagram of meniscus formed with the immersed vertical plate for (a) wetting and (b) non-wetting liquid

2.5.3 Optical hot stage microscopy

The controlled atmosphere or vacuum optical hot stage microscopy is a direct method to study the spreading kinetics of the molten liquid on a solid substrate. Thorsen et al.(1984) reported the experiment setup in the 80s, see Fig.2.19. Dusan Sekulic's lab at University of Kentucky also published multiple experiment results using the optical hot stage microscopy apparatus; see Fig. 2.20 (Zhao et al., 2006; Zhao et al., 2009; Liu et al., 2011; Liu et al., 2012) and Fig. 2.21.

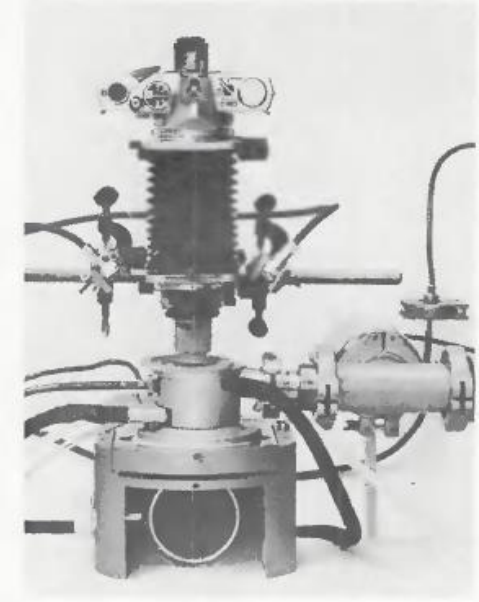

Fig. 2.19 Leitz hot stage 1750 (Thorsen et al., 1984)

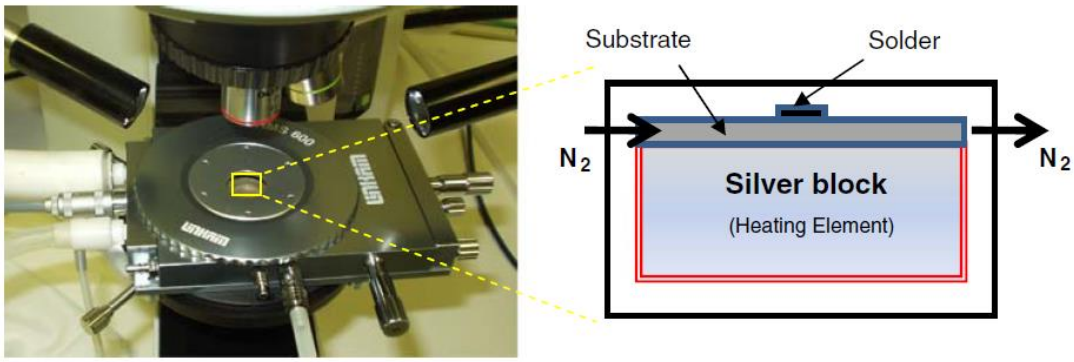

Fig. 2.20 Linkam THMS 600 hot stage system (Zhao et al., 2009)

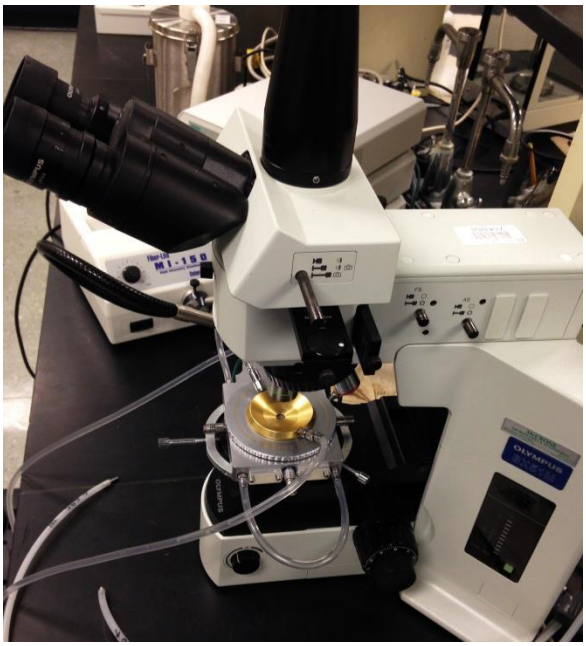

Fig. 2.21 Linkam THMS 600 hot stage installed on an Oplympus BX51M optical microscopy system

The optical hot stage microscopy system normally consists of the hot stage providing high temperatures, an observation chamber providing controlled atmosphere or vacuum condition, a cooling system for rapid quench and an optical microscope connected to data acquisition systems. Due to the miniature size of the chamber, it's possible to apply very

fast heating rate and cooling at fast recording speed. It has been reported the heating rate can reach to 100°C/min and the cooling ramp of 80°C/min (Zhao et al., 2009). Inert gas can be purged into the test chamber or vacuum condition. Due to its small volume, multiple gas volume replacement can take place in a certain period of time. Since the real time video can be captured by the video camera mounted on the microscope, wetting kinetics can be investigated frame by frame with professional image analysis software. Such experiment setup is used to study the molten metal fast spreading process in a short period of time, and offers the direct understanding of kinetics features for different molten metal systems. The surface roughness impact on wetting was also investigated (Wen et al., 2012). The contact angles cannot be measured in this method (the field of vision is from the top). It is also not recommended to study a non-wetting/spreading molten metal on a solid substrate.

2.6 Wetting kinetics theories and models at elevated temperatures

The near non-reactive wetting of molten metals and oxides on molybdenum was studied by Saiz et al. (2007) as an initial step to analyze more complex reactive systems. Without interfacial reactions, the spreading is dominated by dissipation at the triple line location caused by the much stronger atomic interactions compared to organic liquids at low temperatures. As investigated by Voytovych et al. (2007), at high temperatures, the reactive wetting is controlled by compound formation at the interface. Lee et al. (2003) also pointed out that wetting is impacted by both the interfacial reactions and the compound formation at the interface. The spreading can be categorized into three regimes: (i) impact, (ii) inertial and (iii) capillary regime. In the impact regime, the drop hits the substrate (if impacting the substrate at the onset of spreading) and the subsequent flow is

driven by the dynamic pressure and resisted by inertia. In the inertial regime, the flow is driven by the capillary force and retarded by the inertia force. In the capillary regime, the kinetics is controlled by the kinetic energy of the drop, viscosity and surface tension (Saiz et al., 2007). For the high temperature non-reactive systems, stronger interatomic forces cause the increased role of triple line friction and viscous dissipation in the liquid.

For the reactive wetting and spreading at elevated temperatures, common reaction is expected to be observed in the process. As is studied by many (Saiz et al., 1998; Meier et al., 1999; Dezellus et al., 2002; Eustathopoulos et al., 2005; Fu et al., 2016), in the reactive wetting process, not only surface tension and viscosity are dominating, but also more importantly several other physical phenomena, such as chemical reaction, ridging, inter-diffusion, de-oxidation and dissolution of the solid substrate by the molten metal, are also playing significant roles, especially at the triple line location (Eustaphopoulos et al., 1998; Saiz et al., 1998; Saiz et al., 2005; Benhassine et al., 2009; Champion et al., 1969; Drevet et al., 2012). It was pointed out by Eustaphopoulos (1998) that the reactive systems of metal/ceramic or metal/metal systems feature either linear or non-linear spreading, corresponding to reaction-controlled or diffusion-controlled regimes, respectively. Factors like interfacial reaction at the triple line location should be taken into consideration. As shown in Fig. 2.22, the Al-Mg alloy droplet on SiC substrate involves multiple physical phenomena, including dissolution of metal/metal systems, interaction between Al and Si in the interface for metal/ceramic systems, SiO_2 layer forming known as the halo, Mg evaporation off the droplet, Mg and Al diffusion across the surface oxide layer on the SiC as well as chemical reaction between Al and SiC as:

$$4Al + 3SiC \rightarrow Al_4C_3 + 3Si \quad \Delta G^{\theta} = -88.5\ kJ/mol$$

Because of the mass change during the spreading process, the real contact angle should be reduced to the new final contact angle as θ_F, see Fig. 2.23.

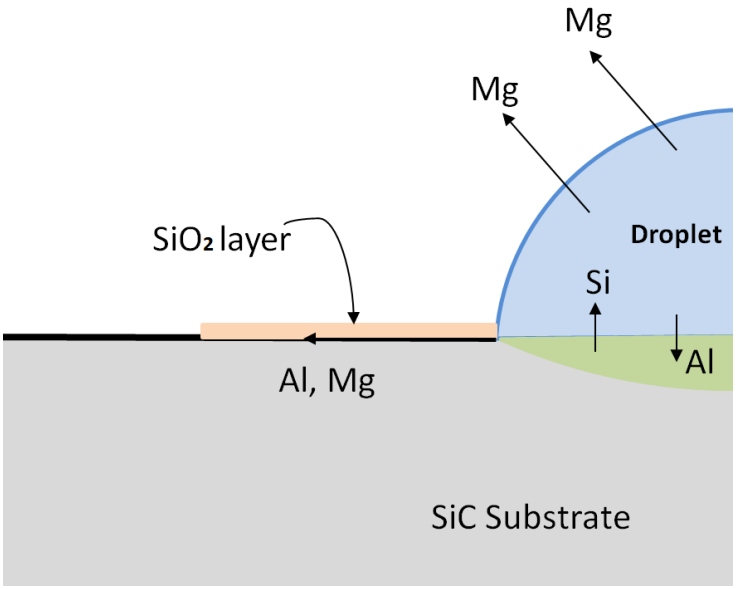

Fig. 2.22 Schematic diagram of interaction mechanism for Al-Mg alloy droplet on SiC substrate (Candan et al., 2011)

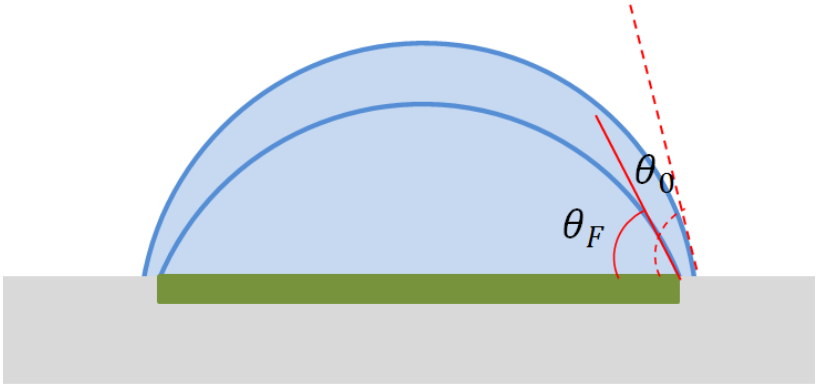

Fig. 2.23 Schematic representation of Al-Mg alloy droplet final contact angle θ_F on reactive substrate compared to unreactive substrate contact angle θ_0 (Dezellus et al., 2010)

As is pointed out by Dezellus et al. (2010), at elevated temperatures for the reactive wetting, spreading kinetics is not limited by viscous dissipation but by the rate of interfacial reaction at the triple line location. The interfacial reaction rate is controlled by the slower of two successive phenomena that happen in the reaction process: diffusive transport of reacting species to or from the triple line location and local reaction kinetics at the triple line location (Dezellus et al., 2010). The new compound formed at the interfacial layer due to reaction can either improve wetting or reduce wetting, depending on wettability by molten metal of new compound compared to the wettability of the initial solid substrate.

2.6.1 Diffusion-controlled wetting of metal/ceramic systems model

In a sessile drop experiment configuration on metal/ceramic systems, the metal drop forms on a solid substrate, and when starts deforming rapidly controlled by viscous force, the initial contact angle θ_D equals the same contact angle of the liquid on the original unreacted substrate. Then as the droplet spreads with the reaction proceeding between metal and the substrate, the final contact angle θ_F will form after a longer period of time. During the spreading process, a reactive penetration of species normally occurs (Saiz et al., 1998). As was pointed out by Saiz et al. (2005), the formed ridge at the triple line location, formed due to local diffusion or solution precipitation, can hinder the spreading of the triple line. It is known that the final contact angle is not related to capillary force dominated spreading, but rather to the reaction product layer formed and droplet volume. Namely, the reaction at the triple line location (Dezellus et al., 2002) a key process. Two spreading regimes can be observed during the process, known as the first linear regime and the second diffusion dominated non-linear regime. For the wetting of metal/ceramic

systems without dissolution, Mortensen et al. (1997) modeled the diffusion-controlled wetting. According to the model, the isothermal spreading kinetics is proportional to the dynamic contact angle:

$$\frac{dR}{dt} = \frac{2DF(t)}{en_v}(C_0 - C_e)\theta_D \tag{2.23}$$

where D is the diffusion coefficient in the liquid, n_v is the number of moles of reactive solute per unit volume of the reaction product, e is the reaction product thickness at the triple line location, $F(t)$ is a function of time which can be considered as a constant of 0.04 for most sessile drop experiments, C_0 is the nominal drop reactive solute concentration, C_e is the concentration of reactive solute in equilibrium with the reactive product, R is the perimeter of the droplet and θ_D is the dynamic contact angle (Mortensen et al., 1997).

The isothermal spreading by metal/ceramic systems limited by solute diffusion at the triple line location showed good agreement with experimental results for AgCuSn-Ti/Cu systems (Dezellus et al., 2010). For Cu-Cr/Cu systems, certain modification to the contact angle is needed for the validity of Eq. (2.23) (Dezellus et al., 2010).

2.6.2 Dissolutive wetting model

Similar to the metal/ceramic systems, wetting for the metal/metal systems is controlled by compound formation at the interface (Voytovych et al., 2007). Four stages of wetting in metal/metal systems can be observed (Yin et al., 2009). The first stage is the initial regime where the liquid spreads with no obvious reaction dominated by the capillary force; the second stage is a highly reactive regime where reaction and the morphological and chemical changes can take place at the liquid and solid interface; the third stage is a

kinetic roughening regime where a solid phase grows the interface between solid and liquid; the fourth stage is the last time regime where the interface equilibrates by solid state diffusion (Yin et al., 2009). For the molten metal spreading on a metal substrate, inter-diffusion can cause partial dissolution of the substrate and/or formation of intermetallic phases (Warren et al., 1998). Warren et al. (1998) proposed an isothermal diffusion/fluid flow analysis to kinetics of the triple line location for the metal/metal systems spreading as:

$$\frac{dR}{dt} = -\frac{DC'}{C}\frac{tan\theta_t + tan\theta_b}{tan\theta_b} \tag{2.24}$$

where R is the perimeter of the droplet, θ_t and θ_b are the upper and lower liquid contact angles, see Fig. 2.24, D is the diffusion coefficient in the liquid, C is the triple line location concentration and C' is the derivative of the triple line location concentration with respect to droplet height.

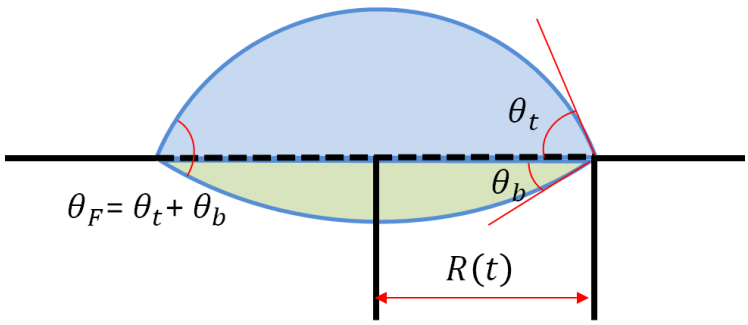

Fig. 2.24 Schematic diagram of the sessile drop final contact angle with relationship to the upper and lower liquid contact angles (Warren et al., 1998)

The dissolution spreading process can also be relevant in some metal/ceramic systems such as AuNi/ZrB_2 (Voytovych et al., 2007) and Ni/C systems (Eustaphopoulos, 1999).

A quasi-linear reactive stage empirical correlation is also modeled by Dezellus et al. (2002). This correlation is valid for the triple line location kinetics that is controlled by the process of atom transfer occurring at the substrate/liquid alloy interface. The correlation is as follows:

$$\frac{U}{F(\theta_D)} = k\left(\frac{3v}{\pi}\right)(cos\theta - cos\theta_D);$$

$$F(\theta_D) = \frac{cos\theta\left(2-3cos\theta_D+cos^3\theta_D\right)-sin^4\theta_D}{sin\theta_D(2-3cos\theta_D+cos^3\theta_D)^{4/3}} \quad (2.25)$$

where U is the triple line movement velocity, v is the droplet volume, k is the constant proportional to the kinetics constant of the dissolution process and to the driving force of the dissolution process, θ_D is the dynamic contact angle, θ is the contact angle. This type of empirical model was well verified by Calderon et al. (2010) using experimental data for Al-Si alloys on carbon substrates. The spreading kinetics increases with temperature and Si content in the alloy, and it is sensitive to the carbon substrate structure (Calderon et al., 2010). However, this model is not valid for the later stage of the spreading kinetics which is limited by the diffusion of reactive species in the reactive layer.

This dissolution spreading model has a good agreement for the Sn/Bi system (Calderon et al., 2010), however, more work and study are needed to have a systematic understanding of this type of reactive wetting in the future.

CHAPTER 3: BENCHMARK STUDY OF THE KINETICS ON A CAPILLARY FLOW OF NON-REACTIVE LIQUID SYSTEMS

In order to establish the reproducibility of the methods used for the experimental data collection of Al-Si (Trillium) systems, a series experiments with non-reactive systems (water and silicon oil on a glass) has been performed. This data were also used to verify the validity of numerical phase field modeling conducted in the collaborative project.

3.1 Overview

In this chapter, the non-reactive wetting experimental procedure is developed for optical evaluation of the contact angle in order to generate empirical data sets needed for theoretical modeling as a benchmark reference involving the reactive wetting evaluation at elevated temperatures. Two types of liquid systems, namely water and silicone oil, at ambient temperature are investigated by developing the wedge-tee configuration spreading. The wedge tee pre-cleaned glasses forming a Wilhelmy-type plate configuration (a single substrate in contact with the pool of liquid). Both equilibrium states of the triple line location and the triple line kinetics are studied for verification of the empirical correlation form derived by various sources, corresponding to Washburn's Law (Washburn, 1921) type of power law. The surface tension driven spreading, retarded by viscosity, at the ambient temperature is considered to be wetting without chemical reactions. The experimental data and procedures are validated by comparing to the theoretical triple line spreading height (upon reaching the equilibrium state), as well as empirical spreading kinetics correlations. This chapter provides a benchmark foundation

upon which later chapters involving molten metal reactive spreading kinetics can be based.

This chapter consists of two parts, (i) the static study of the triple line equilibrium spread, and (ii) the kinetics study of triple line spreading. The static contact angle of both liquid systems was proved to obey the theoretical prediction (Seebergh et al., 1992) of the equilibrium triple line location. The Neumann (1972) theoretical prediction based on Young's equation confirms the agreement with data excellently. In the second part of this chapter, the kinetics of the triple line prediction are verified by different empirical correlations using the capillary number and dynamic contact angle. The dynamic contact angle and capillary number of silicone oil system agree with the existing correlation models, however, the water on glass system showed the deviations to a certain degree from those known models. A new correlation model was established for the water on glass system. The liquids wetting on the vertical slides also showed the Washburn flow pattern in the initial capillary-viscous stage. Hence the wetting was initially driven by surface tension and retarded by viscosity. The subsequent stage showed a clearly 5th power law relationship, thus surface tension and viscosity showed a less dramatic impact on the wetting process.

3.2 Experimental setup and procedure

3.2.1 Material preparation

In order to study the spreading process of non-reactive liquid, the Wilhelmy plate configuration is adopted in this investigation. Two types of liquids are chosen for the study of the kinetics of non-reactive liquid systems: deionized water (DI water) and silicone oil. The properties of the liquids can be found in Table 3.1.

Two microscope glass slides perpendicular to each other are used as the Wilhelmy plate configuration, see Fig. 3.1. The substrates are 25×75×1mm, pre-cleaned manufactured by Thermo Scientific (Thermo Scientific, #2950-001) (Thermo Scientific Website). The gap between two slides is set initially to be 1mm±0.5mm before the vertical plate starts to move down to the liquid surface.

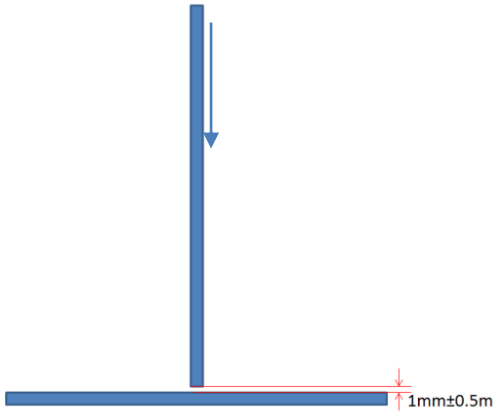

Fig. 3.1 Glass slides Wilhelmy plate configuration with the fixed horizontal plate and moving vertical plate

Table 3.1 Properties of Liquids

Liquids	Density (kg/m3)	Surface Tension (N/m)	Dynamic Viscosity (Pa·s)	Apparent Contact Angle on Horizontal Glass Substrate (deg)
DI water (25°C) (Song, 2009)	997	0.07197	0.0008937	0
Silicone Oil S159-500 (25°C)	960	0.02089	0.0096	0

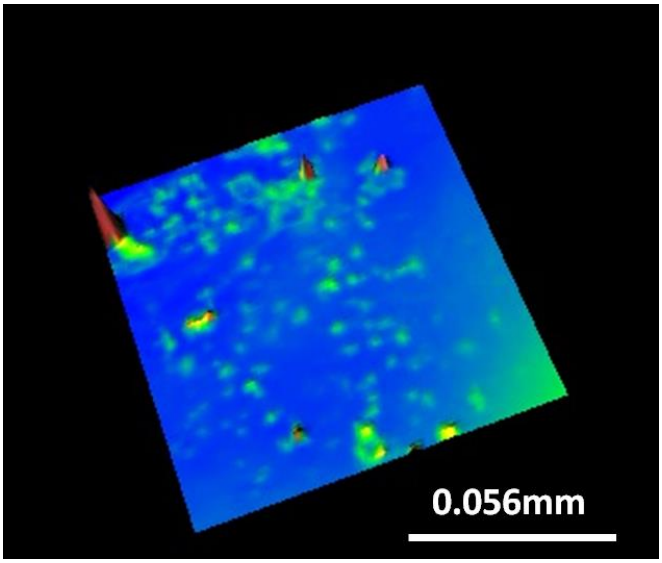

Fig. 3.2 3D scanning image of topography of Thermo Scientific, #2950-001 microscope glass, measured by Zygo New View TM 7300 3D Optical Surface Profiler, (from blue to red color, the level increases)

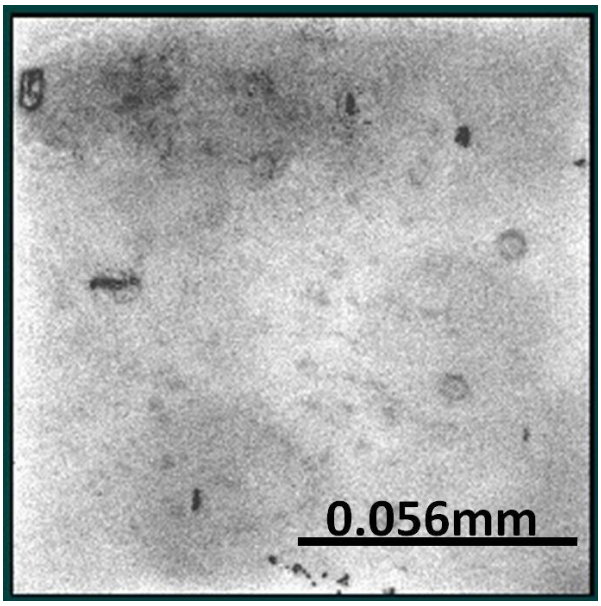

Fig. 3.3 3D scanning intensity map of topography of Thermo Scientific, #2950-001 microscope glass, measured by Zygo New View TM 7300 3D Optical Surface Profiler

The surface can be considered as smooth, see Fig. 3.2. The surface roughness of the glass substrate was measured by Zygo New View TM 7300 3D Optical Surface Profiler. A total of 20 measurements were conducted at random locations on the substrate leading to the average roughness of 0.0014 ± 0.0009 μm (hence considered as perfectly smooth), see Table 3.2. In order to eliminate any potential contamination of the wetted surface and to eliminate the related impact on the kinetics of the liquids, for each test, a new virgin glass plate is used for both vertical and horizontal plates in each test run.

Table 3.2 Thermo Scientific, #2950-001 microscope glass surface roughness measurement data

Measurement	Surface Area (mm^2)	Surface Roughness *Ra* (μm)	Average Surface Roughness *Ra* (μm)
1	0.0121	0.002	0.0014 ± 0.0009
2	0.0121	0.001	
3	0.0121	0.002	
4	0.0121	0.002	
5	0.0121	0.001	
6	0.0121	0.002	
7	0.0121	0.003	
8	0.0121	0.002	
9	0.0121	0.002	
10	0.0121	0.002	
11	0.0121	0.001	
12	0.0121	0	
13	0.0121	0.003	
14	0.0121	0.001	
15	0.0121	0.001	
16	0.0121	0.001	
17	0.0121	0	
18	0.0121	0.001	
19	0.0121	0	
20	0.0121	0	

3.2.2 Experiment configuration

As is introduced previously in Section 2.2.3, the Wilhelmy plate configuration is used in the experiment study. This study has been performed to verify the phase field modeling formulation (to be addressed later) before it is implemented in the simulation of the liquid metal triple line kinetics. All tests were conducted under the lab environmental conditions (air at 22℃ ± 2℃ and humidity less than 60%). In the benchmark testing, the non-reactive liquid layers of different thicknesses were formed on the horizontal surface to form the surface tension driven meniscus in the wedge-tee corner upon levering the vertical substrate, see Fig. 3.1. In the benchmark testing, the non-reactive liquid layers of different thicknesses were formed on the horizontal surface to form the surface tension driven meniscus in the wedge-tee corner. The vertical glass slide was held on an adjustable clamp which was fixed on an optical mounting post with the precisely adjustable laboratory jack. The adjustable laboratory jack was controlled manually to provide a slow motion of the vertical plate moving towards the liquid layer, see Fig. 3.4. It should be added that the considered subsequent wetting phenomenon has the time scale of the multiple orders of magnitude faster vs. the vertical plate surface movement at the onset of a test; consequently that experimentation feature has negligible impact on the results involving kinetics of the triple line movement. The movement impact will be discussed in later sections. The vertical glass maintained the vertical position of 1 ± 0.5 mm above the horizontal glass slide for the purpose of executing experimental runs with different thicknesses of liquid layers, see Fig. 3.5.

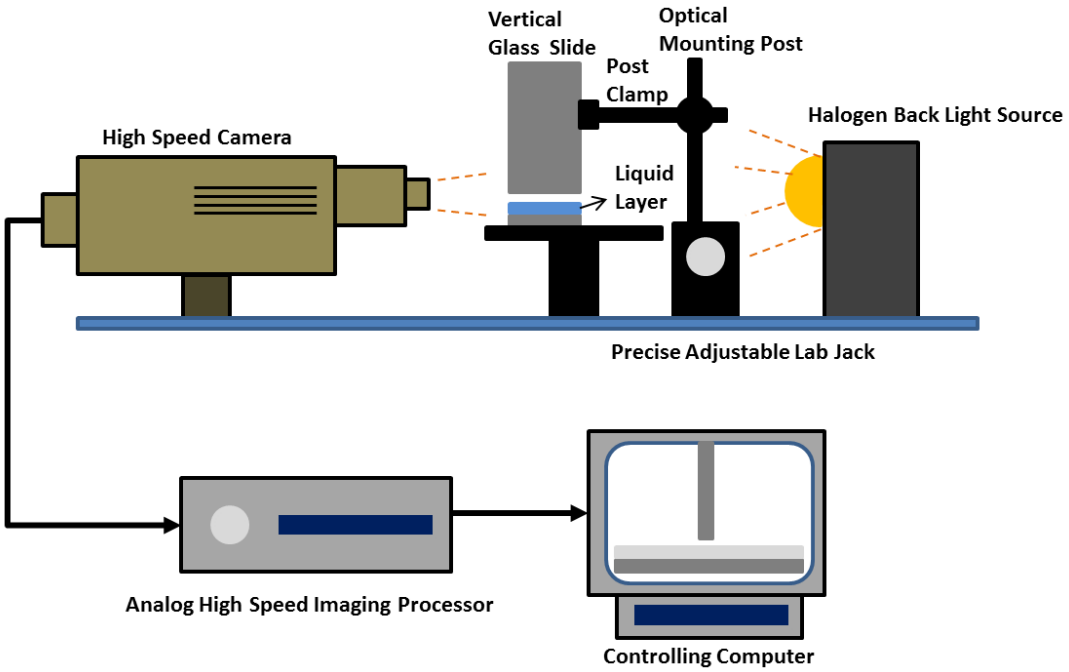

Fig. 3.4 Schematic diagram of the non-reactive liquid kinetics experiment configuration

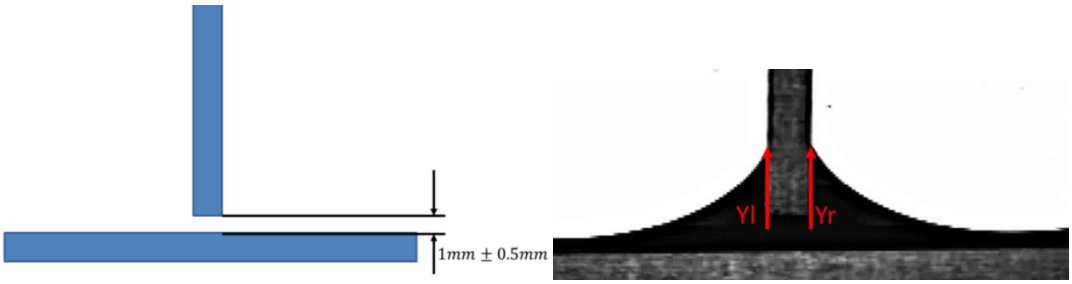

(a) (b)

Fig. 3.5 (a) Wedge-tee glass slides configuration (Wilhelmy plate configuration) and (b) triple line location on both left side (Yl) and right side (Yr)

As is shown in Fig. 3.5 (b), when the vertical plate inserts into the liquid surface, a meniscus forms along two sides of the vertical plate. The kinetics of the to be formed meniscus and its evolution was triggered after a gradual downward movement of the vertical glass slide at a very low speed until the edge of the vertical glass slide intrudes

the surface of the liquid layer. A halogen back-light source was lit to provide the counter-light for the high-speed imaging. The meniscus formation process was captured by a high speed analog camera (Kodak, EktaPro) at 1000 frames per second for water and 500 frames per second for silicone oil, well within the range of time instants needed for capturing instantaneous frames over the meniscus formation period. The analog signals were captured by the analog high speed imaging processor (Kodak, EktaPro Hi-Spec Processor) and eventually converted to digital high speed video files on the controlling computer. The videos were decomposed into multiple frames of images and analyzed using the Image-Pro© software for image data acquisition. As is shown in Fig. 3.5 (b), the meniscus profile can be presented clearly, and the triple line locations for both left side and right sides can be identified and measured. The length calibration during each measurement provides the proper length vs. time scales.

3.2.3 Experiment procedures

In this benchmark experiments, both water and silicone oil on glass systems are tested using Wilhelmy plate configuration. The initial experiment is to verify the relationship between the contact angle and vertical triple line location in the equilibrium state. The follow-up experiment is to record the triple line as well as contact angle kinetics. In order to ensure reaching the equilibrium state of the water meniscus, after the vertical glass slide slowly advanced to the horizontal plate to form the liquid meniscus on the vertical/horizontal substrate, each video was recorded for a total of 5 minutes, well after the triple line location movement was completed. The extended period of time was imposed to identify also whether liquid evaporation impacts the process. No impact of the phase change was identified. At least three identical experiments (under the same

conditions) were executed for both water and silicone oil systems. Each test was performed with a new set of pre-cleaned glass substrates. It was found that the already used glass features surface conditions that may impact the kinetics of the process regardless of an implemented cleaning treatment in the previous preliminary tests. The liquid meniscuses of both water and silicone oil were formed well within 2 seconds. As the videos of the kinetics of both water and silicone oil were recorded by the high speed camera, images of different frames from the video can be exported to Image-Pro© to measure the instantaneous dynamic contact angle and the triple line location, see Fig.3.6. In the case of the water system, the whole kinetics process lasts for the order of magnitude of 10^3 ms, whereas the process lasts a bit longer (the same order of magnitude, $2x\ 10^3$ ms) in the case of the silicone oil system. For each experiment measurement, a new calibration of the meareument is required in Image-Pro© before a new measurement.

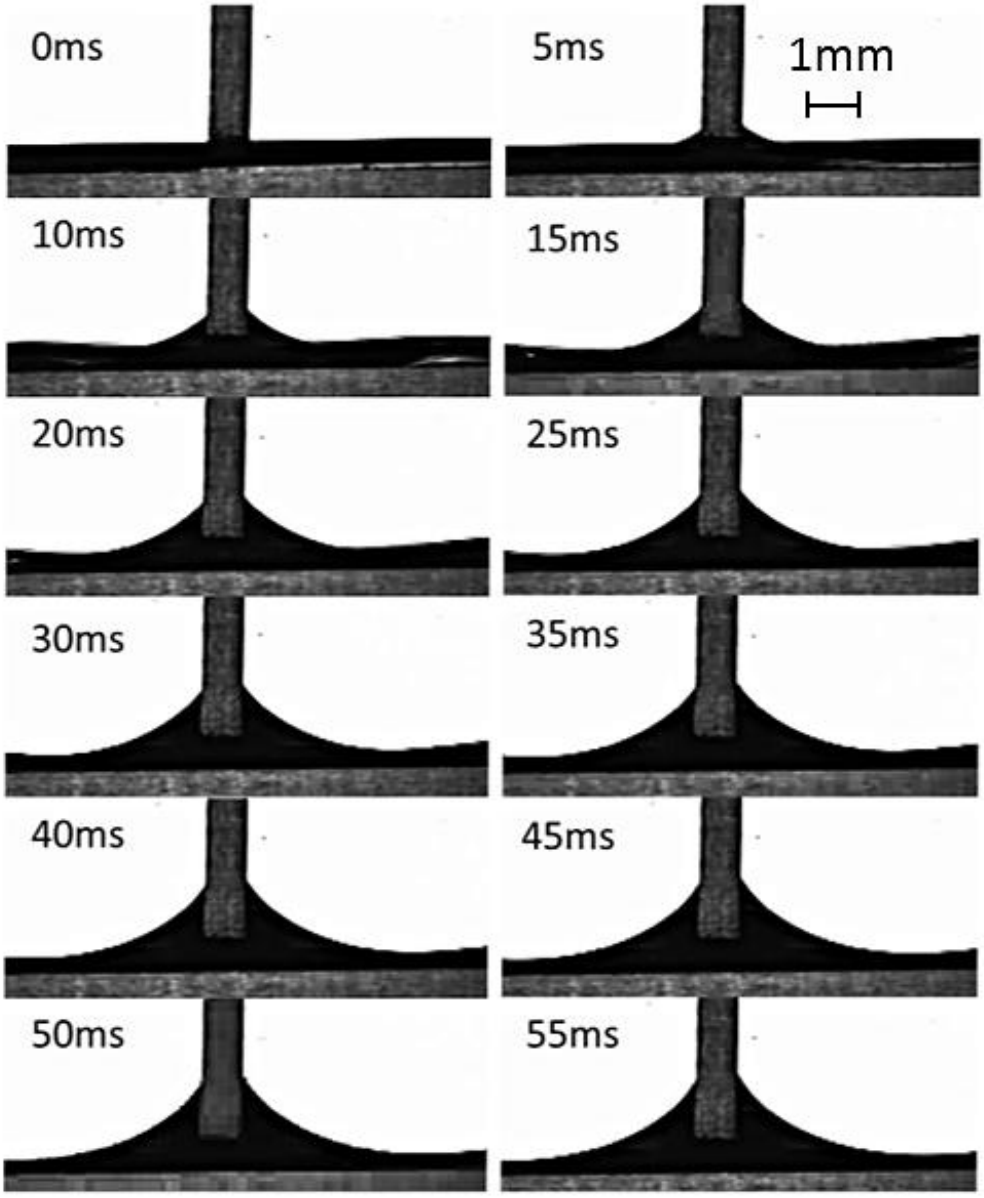

Fig. 3.6 Water meniscus formation process profile

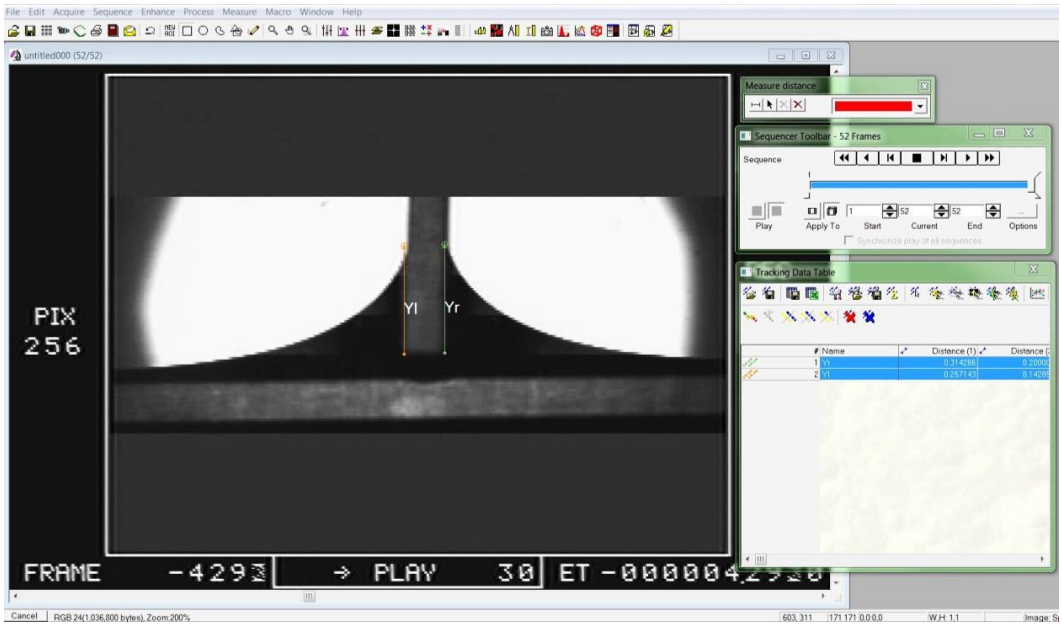

Fig. 3.7 Screenshot of Image-Pro© tracking object measurement method

Different frames of images are imported to Image-Pro©, and the "tracking object" function is used to track triple line location and dynamic contact angle in each and single frame manually, Fig. 3.7. The measured triple line location and dynamic contact angle can be exported to the Excel file for further analysis.

As shown in Fig. 3.8 and Fig. 3.9, the water kinetics profiles are overlapped so that the triple line location changes are shown in the same scale.

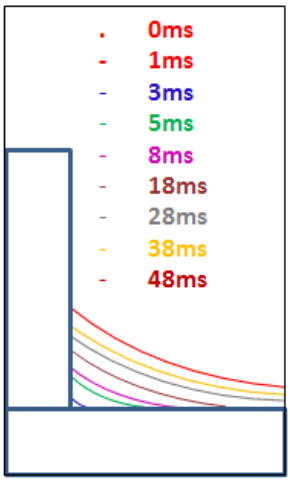

Fig. 3.8 Experimental water meniscus growth lengths profiles in 9 time frames

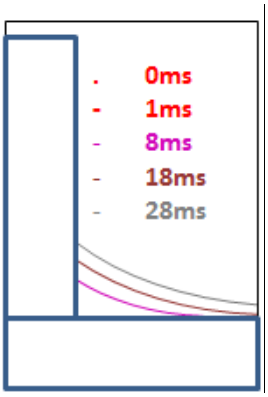

Fig. 3.9 Experimental water meniscus growth lengths profiles in 5 time frames

For the water on glass system, different thicknesses of water layers are tested, see Table 3.3. The thicknesses were measured from the middle point of the vertical plate cross section vertically to the bottom of the water layer. After the video was converted to individual frame images, each image constitutes the time data point of 1ms. The meniscus of the water evolves and the triple line on the surfaces of the vertical glass slide in 20ms. A thinner layer point on the horizontal water layer was observed in the process as the triple line location grows vertically. The thinnest horizontal liquid layer free surface location spreads out away from the vertical glass slide (see Fig. 3.6). The similar

processes are observed in all other cases of different initial (steady) thicknesses of the water layers. As seen in Table 3.3, 9 independent different silicone oil layer thicknesses, and 3 repeating measurements were applied to each layer thickness. Three of those tests are chosen randomly for kinetics analysis with three repeating measurements for each layer thickness.

Table 3.3 Different initial thicknesses of water layer data

Experiment	Thickness (mm)	Standard Deviation (mm)
a	0.528	0.028
b	0.542667	0.028501
c	0.495333	0.043753
d	0.457333	0.028501
e	0.263	0.026
f	0.306667	0.0306
g	0.324	0.015588
h	0.666667	0.015588
i	0.667	0.066425

For the silicone oil on glass system, the images were extracted from different frames from the video, see Fig. 3.10. The same experimental and measurement procedures are used for the determining the equilibrium contact angle and the instantaneous triple line locations as well as the kinetics of triple line location.

Table 3.4 Different initial thicknesses of silicone oil layer data

Experiment	Thickness (mm)	Standard Deviation (mm)
a	0.2451	0.044909
b	0.342667	0.042336
c	0.324	0.042226
d	0.416667	0.027502
e	0.357667	0.014434
f	0.119333	0.015011
g	0.127667	0.025502

As is shown in Table 3.4, 7 independent, different silicone oil layer thickness, and 3 repeating measurements were applied in each layer thickness. Three of those tests are chosen for kinetics analysis with three repeating measurements for each layer thickness.

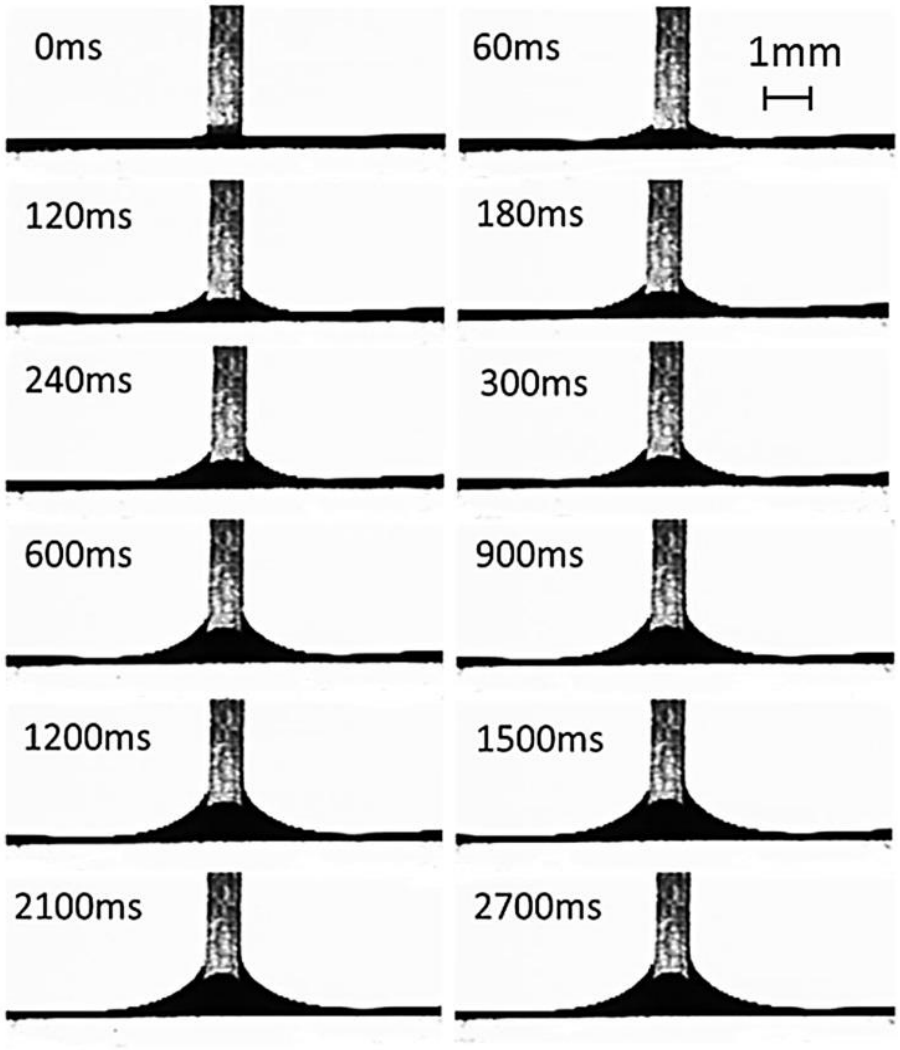

Fig. 3.10 Silicone oil meniscus formation process profile

3.3 Experiment results and discussion

3.3.1 Validation of the equilibrium relationship between the contact angle and the triple line location

In order to verify the measurement of the equilibrium contact angle in the subsequent experiments, a theoretical relationship between the triple line location and the contact angle is compared to the experiment data. The solution is based on the model developed by Neumann (1972) who employed the capillary rise of a liquid in contact with the heterogeneous surface, see Fig. 3.11. The relationship between the contact angle θ and the triple line location y in equilibrium can be expressed as:

$$y = \pm\sqrt{\frac{2\gamma_{LG}}{\rho g}(1-\sin\theta)}, \tag{3.1}$$

where a positive value of y corresponds to $0 \leq \theta \leq 90°$ and a negative value to $90° \leq \theta \leq 180°$. γ_{LV} is the liquid-gas surface tension, ρ is the liquid mass density (gas mass density is neglected), and g is the gravitational acceleration.

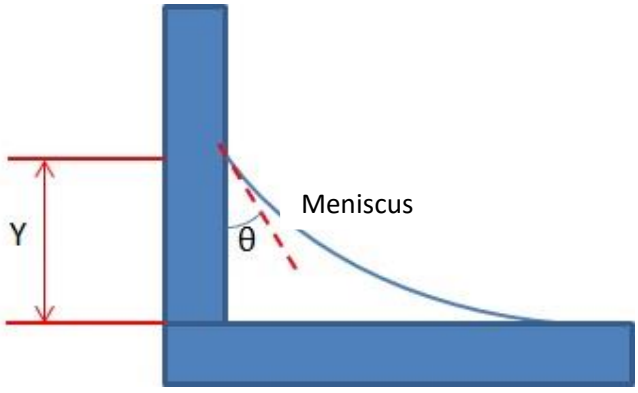

Fig. 3.11 Meniscus triple line location height and contact angle

As was mentioned earlier, in order to ensure reaching the equilibrium state of the water meniscus, after the vertical glass slide slowly advanced to the horizontal plate to form the liquid meniscus on the vertical/horizontal substrate, each video was recorded for a total of 5 minutes, well after the triple line location movement was completed. As shown in Fig. 3.12, a total of 9 experiments are conducted with measurements of 3 times each.

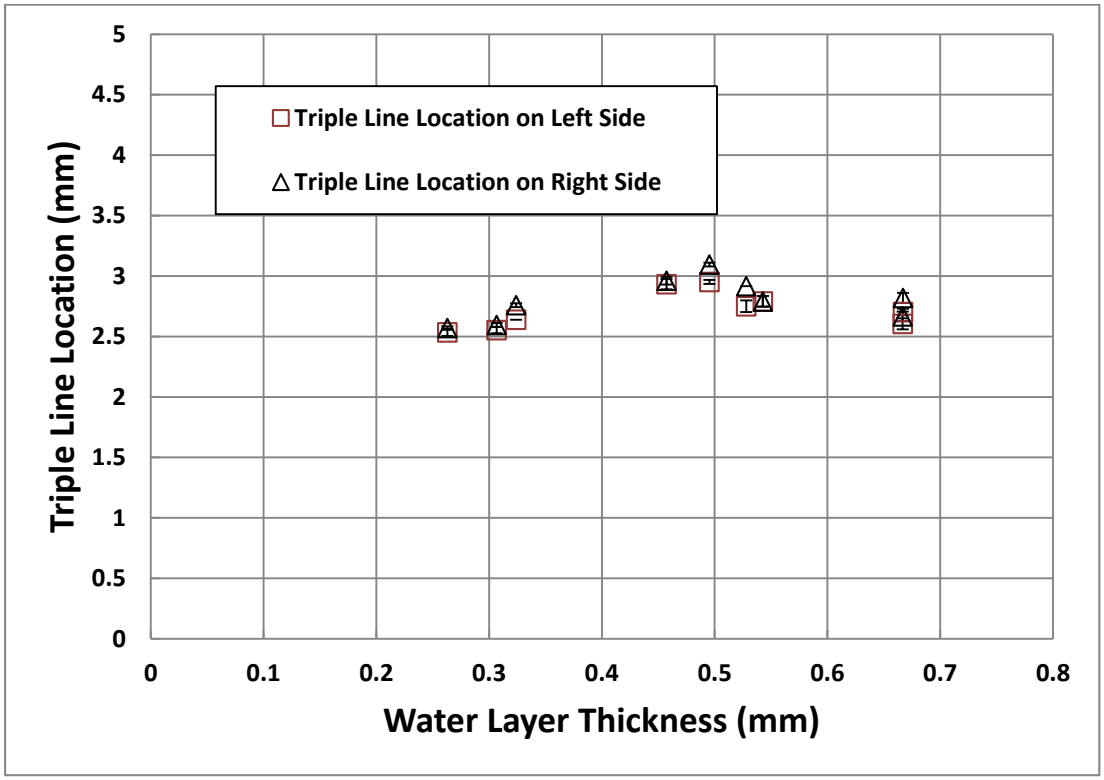

Fig. 3.12 Water layer thickness and vertical distance relationship with error bars comparison

Fig. 3.12 shows that water triple line location is independent of the water layer thickness, given enough water for the triple line to grow. Both left and right sides of the meniscus are measured for the same set of experiment. It can be seen from the figure that for the same set of experiments, both left and right locations have very close values of the triple

line equilibrium location height. The average triple line height at equilibrium state is 2.758 mm ± 0.016mm. It should be noted that if the liquid layer is not enough to form the fully grown meniscus, the triple line location height will be lower than the measured data, what did not happen. Hence, the data set is valid.

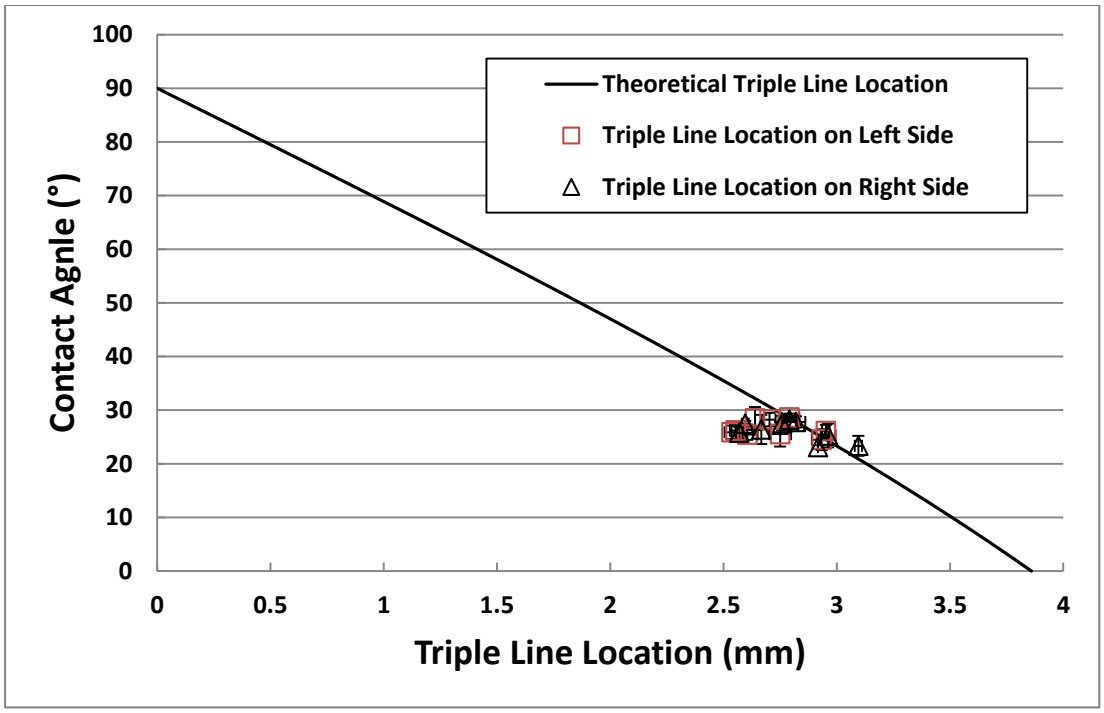

Fig. 3.13 Theoretical prediction and experimental comparison of the contact angle and triple line location relationship in water on glass system

Both left and right triple line location with equilibrium contact angle are measured with an assessment of the associated error bars. The result is plotted against the theoretical line from Equation 3.1, see Fig. 3.13. It can be seen that both left and right triple line location and equilibrium contact angle are close to each other in the same experiment set. Between different experiments of different water initial layer thicknesses, the data points are clustered. The result shows a good agreement with the theoretical prediction from

Neumann (1972). The average equilibrium contact angle for water is 26.3°±1.7°. The water equilibrium correlation between contact angle and triple line location proves that the current experiment configuration and experiment procedures for studying the near-reactive liquid spreading on the wedge-tee joint configuration is valid and applicable.

In a similar way, silicone oil S159-500 system (Fischer Scientific, LOT 116611) was chosen to extend the triple line location benchmarking testing. Seven sets of experiments with the same procedures as for the water experiments were conducted, and 3 of those are chosen for the kinetics study. After the vertical plate immerges into the silicone oil surface, the meniscus forms within 2 seconds at the wedge-tee joint area. The video stops recording after 5 minutes when the equilibrium of the triple line location is ensured to be reached. Images of the whole process are imported to Image-Pro© for analysis.

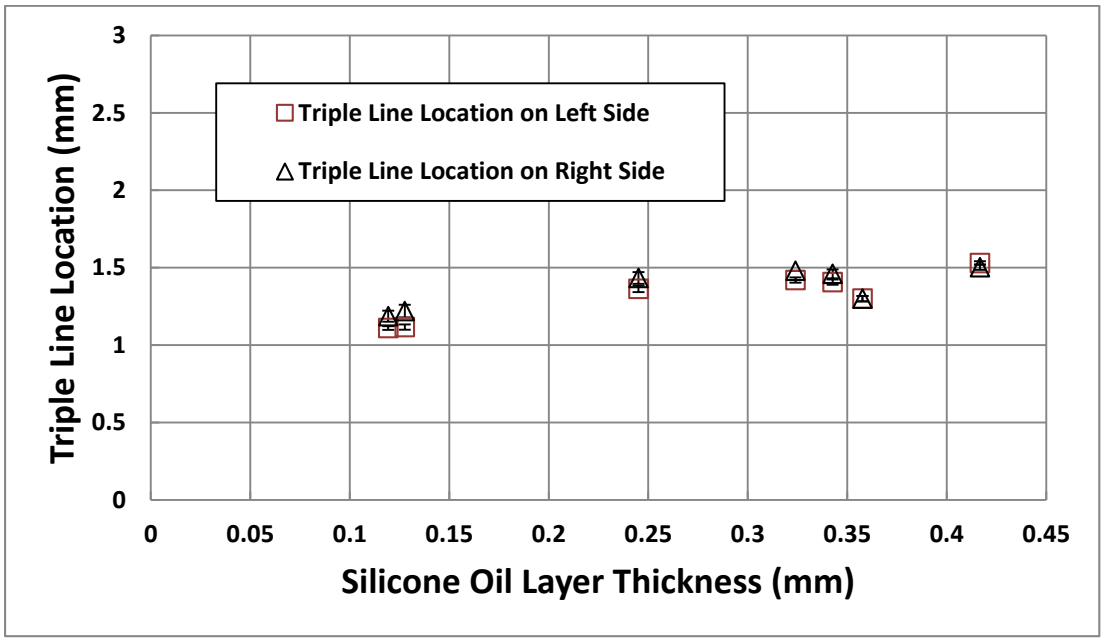

Fig. 3.14 Silicone oil layer thickness and vertical distance relationship with error bars comparison

The thickness and triple line location equilibrium height are plotted in Fig. 3.14. The average triple line location height is 1.34 mm±0.14 mm with the average thickness of 0.28 mm±0.12 mm. The similar result for silicone oil can also be observed as both left and right triple line location heights are very close to each. Therefore, the menisci on both sides can be considered as symmetric. Within the range of 0.1mm to 0.45mm silicone oil thickness, the triple line location heights are very close with a small deviation. This result shows that for the enough silicone oil liquid provided, the layer thickness does not impact the triple line location height. A slight tendency of the triple line location decreases with the decrease of the silicone oil thickness.

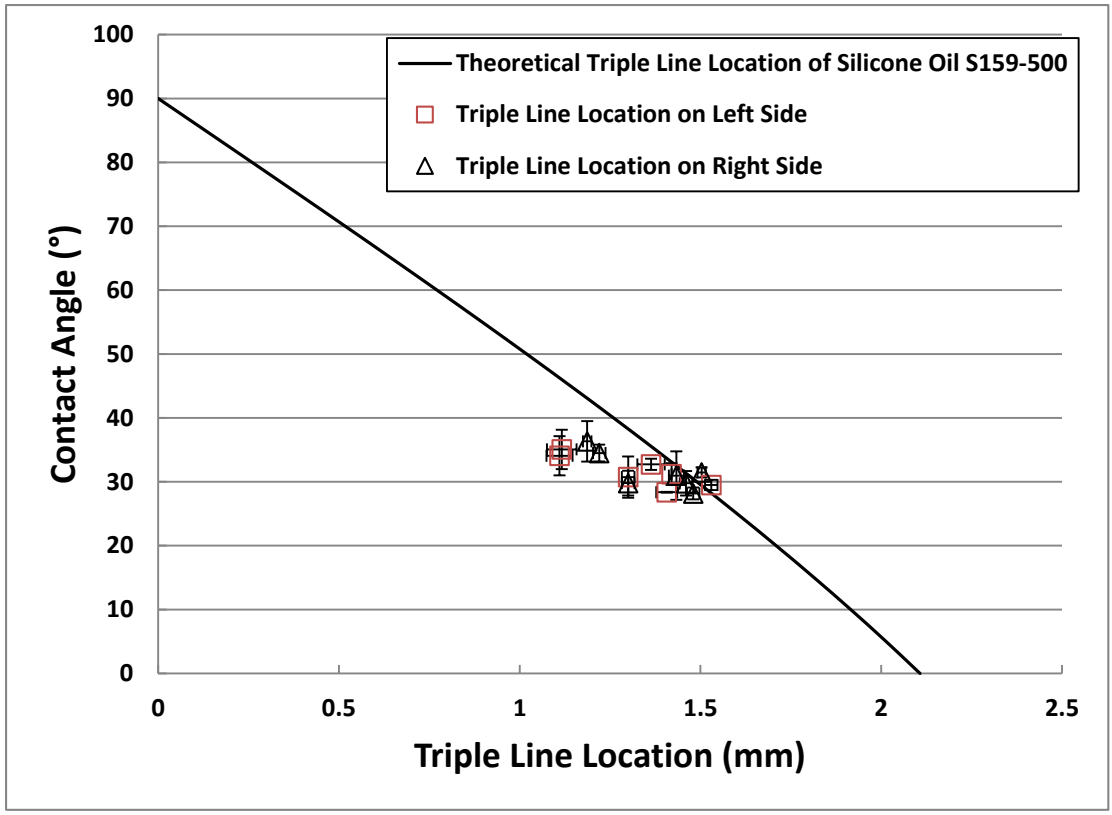

Fig. 3.15 Theoretical prediction and experimental comparison of the contact angle and triple line location relationship in silicone oil on glass system

As shown in Fig. 3.15, the equilibrium triple line location height and the equilibrium contact angle are plotted with error bars against the Equation 3.1 (a theoretical prediction line). All the experimental data from 7 sets of experiments are mostly clustered in the approximately same area. The average contact angle is 31.6°±2.6°. The experiment result for silicone oil, therefore, shows a good agreement with the correlation by Neumann (1972) in Equation 3.1.

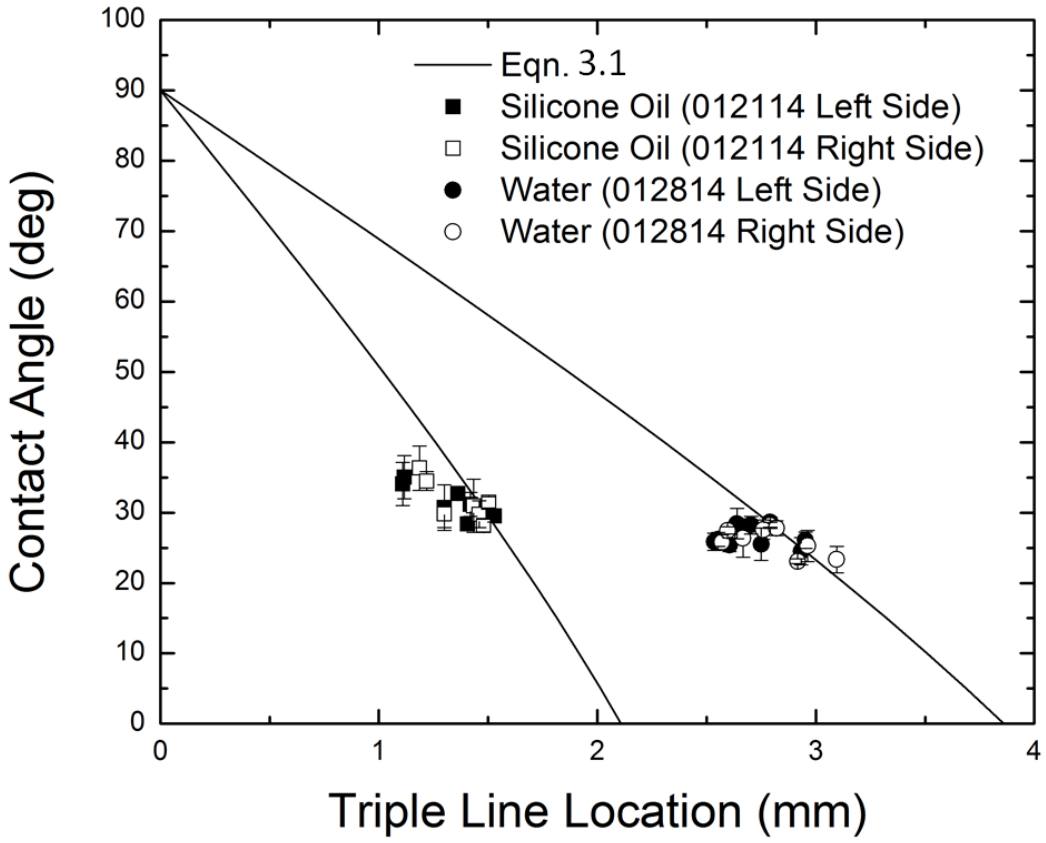

Fig. 3.16 Water and silicone oil systems comparison of theoretical prediction with experiment data for contact angle and triple line location correlation

In Fig. 3.16, a comparison between the two liquid systems made with both experiments data and the theoretical prediction lines. It can be seen that in equilibrium, the liquid

systems fully agree with the traditional Young-Neumann theory and verify fully the agreement with the experimental data. Note again that multiple experiments were conducted in each system case on both left and right sides of the joint zone, and multiple measurements were taken to minimize the errors potentially caused during the measurement procedure. The generated data sets show the consistency regardless of different liquid layer thicknesses with small standard deviations. Hence, the theoretical and experimental results agreement is satisfactorily verified and the validity of the measurements of the contact angle and the triple line location has been established.

3.3.2 Dynamic contact angle experimental correlation

As mentioned in Chapter 2, many sources have reported the relationships between dynamic contact angle and the capillary number ($Ca = \frac{\mu U}{\gamma}$, μ is the liquid viscosity, γ is the liquid surface tension and U is the triple line movement speed). Jiang et al. (1979) proposed an empirical, universal function for the model, applicable for silicone type of liquid at the ambient temperature:

$$\frac{\cos\theta - \cos\theta(t)}{\cos\theta + 1} = tanh(4.96Ca^{0.702}) \tag{3.2}$$

where θ is the static contact angle, $\theta(t)$ is the dynamic contact angle.

Similar empirical models were also reported by Brake et al. (1973) and Seeberg et al. (1992). Seebergh et al. (1992) found that the models have a good agreement for high capillary numbers ($10^{-3} \leq Ca \leq 3 \cdot 10^{-2}$), but not for low capillary numbers. In our case, the water system capillary number is low enough to be considered as the capillary number. The functions are expressed as follows (Seebergh et al., 1992):

$$\frac{\cos\theta - \cos\theta(t)}{\cos\theta + 1} = 2.24Ca^{0.54} \quad (3.3a)$$

$$\text{for } Ca \leq 10^{-3}, \frac{\cos\theta - \cos\theta(t)}{\cos\theta + 1} = 4.47Ca^{0.42} \quad (3.3b)$$

Due to the fact that both left and right side of the menisci are close to each other, see Fig. 3.16, presenting a symmetric trend, to clearly show the total set of experiment data, both of left side and the right side of the two menisci were chosen to compare with the empirical correlations. The linear scale comparison of the experiment data and Jiang's (1979) empirical correlation shows good agreement. As shown in Fig. 3.17, the experiment data only presents dynamic contact angle from 20° to 60°, this is only partially covered in the empirical correlation. This result can be explained by the limitation of the current Wilhelmy plate configuration, see Fig. 3.18. The last dynamic contact angle is always larger than the equilibrium contact angle of the specific liquid system, whereas the initial contact angle is never larger than 90°.

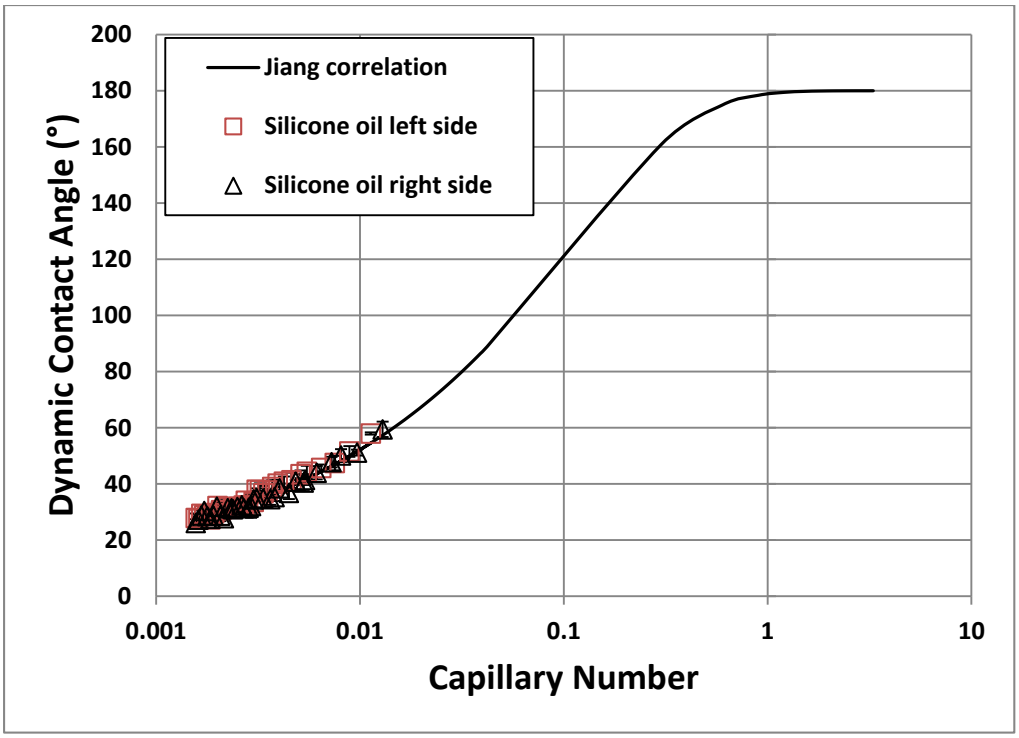

Fig. 3.17 Experiment and empirical correlation comparison of dynamic contact angle and capillary number relationship for silicone oil system in linear scale

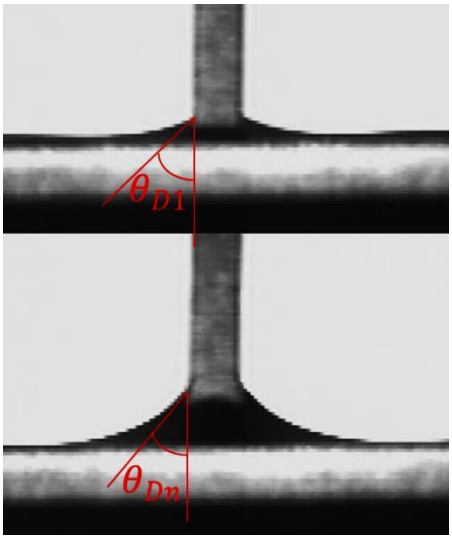

Fig. 3.18 Schematic screenshot of the initial dynamic contact angle θ_{D1} and the last dynamic contact angle θ_{Dn} in Wilhelmy plate configuration

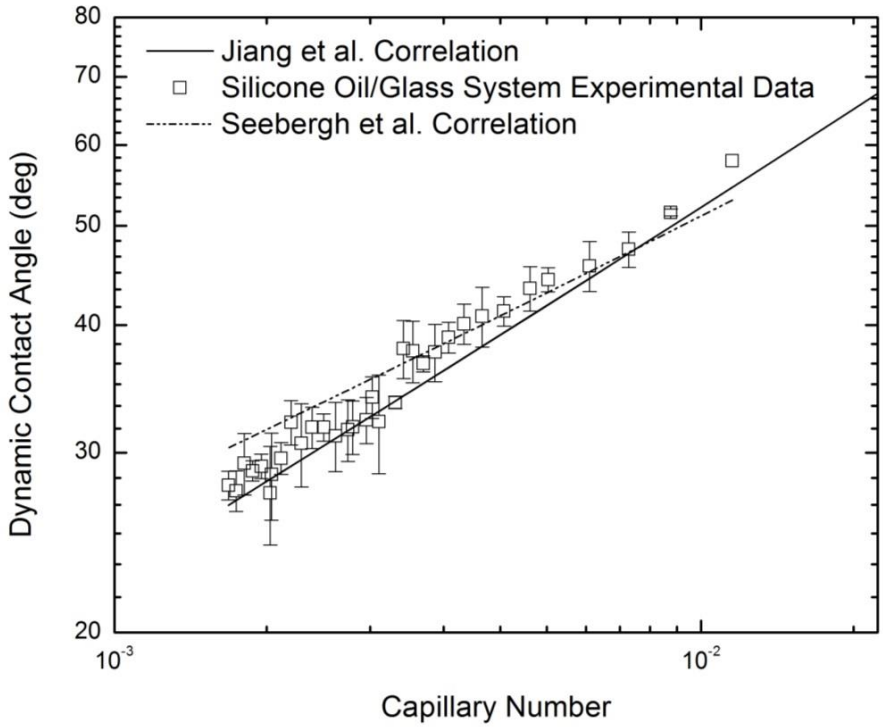

Fig. 3.19 Silicone oil dynamic contact angle correlation models and experimental data comparison in log-log scale

With both empirical correlations from Jiang et al. (1979) and Seeberg et al. (1992), an average of 3 sets of experiments with error bars are shown in Fig. 3.19. The experimental results show that for silicone oil on glass system, the result agrees well with Jiang's universal function model prediction and Seebergh's correlation. For different empirical correlation models, a deviation can be observed starting from the early stage. The experiment data land within the range of both models.

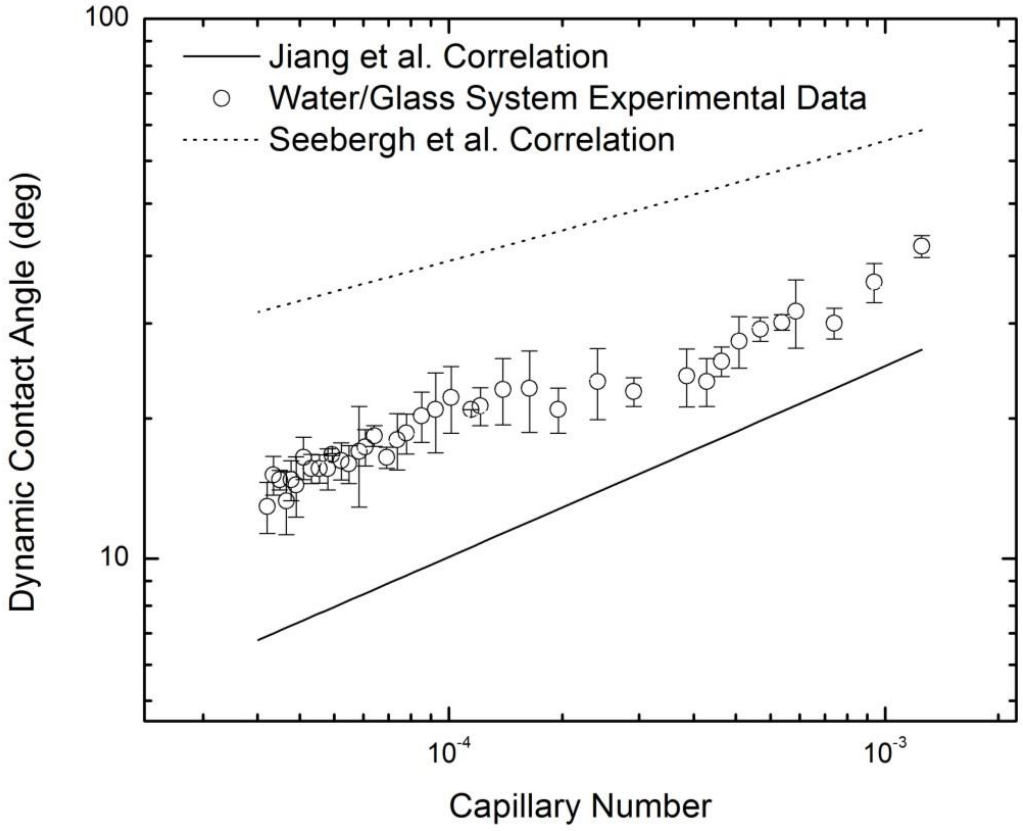

Fig. 3.20 Water dynamic contact angle correlation models and experimental data comparison in log-log scale

As mentioned by Seebergh (1992), his correlation model doesn't apply for low capillary numbers, and the same is true for Jiang's (1979) correlation model. Therefore, since water has a lower capillary number-lower than 10^{-3}, their empirical correlation models don't match with experiment data, see Fig. 3.20. Six independent sets of experiments with error bars for the dynamic contact angle and capillary number relationship are plotted against the two models by Seebergh et al. (1992) and Jiang et al. (1979). The experiment data are generally in linear line dependence in the log-log scale, however, the experiment data land in between the two empirical models with deviation from both models. It should be noticed that in Seebergh's experiments, the water was spreading on

mica with static contact angle as 5°. In our experiments, the water was spreading on a glass slide with static contact angle as 0°. Therefore, the surface state/properties play(s) a role impacting the dynamic contact angle. Based on the water on glass system experimental data, a modified Seebergh correlation of the square fit of the data yields:

$$\frac{\cos\theta - \cos\theta(t)}{\cos\theta + 1} = 2.44Ca^{0.5} \tag{3.4}$$

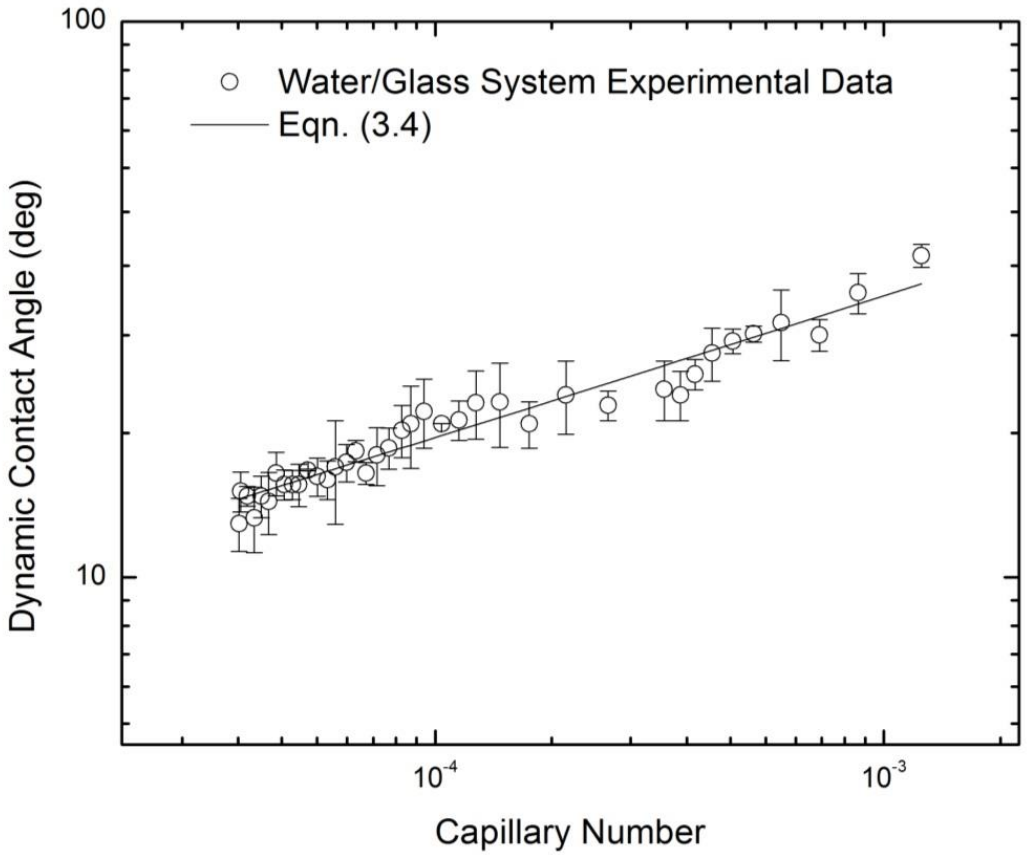

Fig. 3.21 Modified empirical correlation and water on glass system experiment data comparison

The fitting equation matches the experimental data as is shown in Fig. 3.21 with an R square value of 0.94. The current function shows the same form as Equation 3.3a

developed by Seebergh (1992), however the constants are modified to better represent the dynamic contact angle behavior of the water on glass system.

3.3.3 Kinetics of two liquid systems

Three sets of triple line kinetics experiments for each liquid system were conducted following the established experimental procedures. Data for the triple line location vs. time taken randomly from one side of the wedge-tee joint were compared since the left and right side of the kinetics are relatively close to each other.

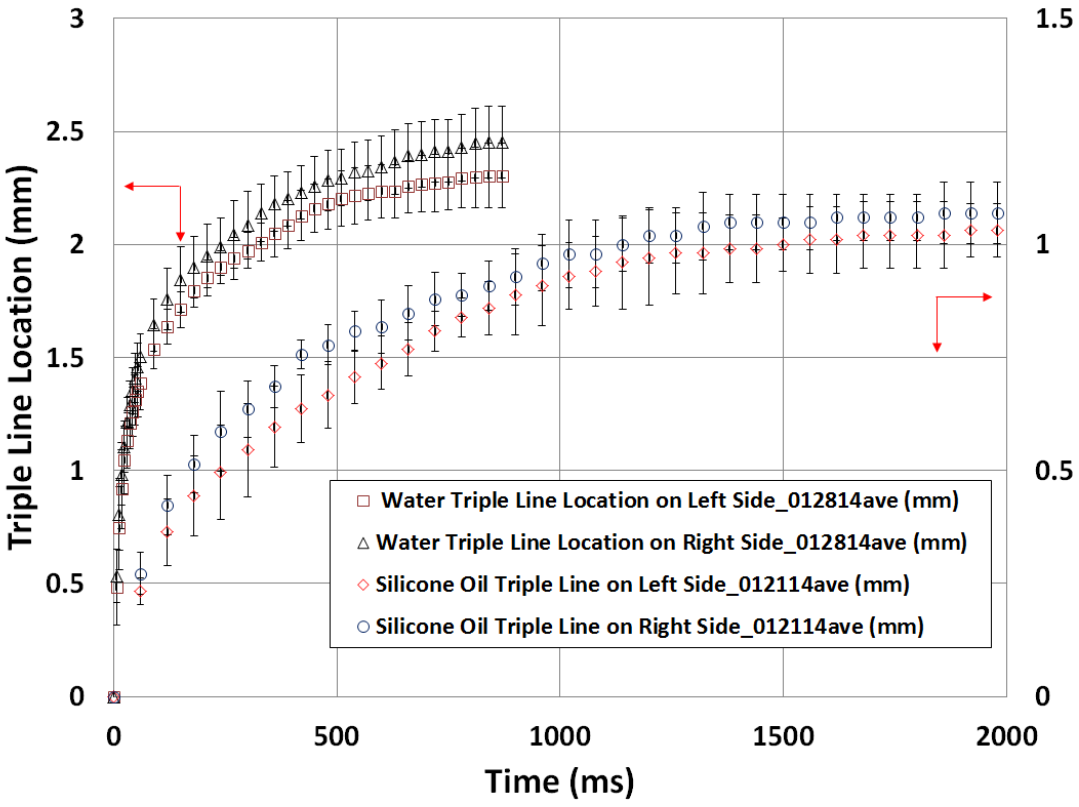

Fig. 3.22 Averaged water and silicone oil systems triple line kinetics comparison with error bars

As shown in Fig. 3.22, both water and silicone oil systems triple line kinetics are plotted against each other for comparison. Due to a much higher viscosity for silicone oil system,

the surface tension driven kinetics is more impacted by the viscosity, thus causing a lower kinetics process (by a factor 2, 2 seconds for silicone oil and 1 second for water). It can be seen that for both water and silicone oil systems, the initial rate is higher due to inertia force, and subsequently driven by surface tension, retarded by viscosity in the rest of the process.

Based on Neumann and Good 1972, in the equilibrium state, the vertical distance of the triple line location has a relationship with the contact angle as follows:

$$L_{E,i} = \pm \left(\frac{2\gamma_{LV,i}}{\rho_{0,i} g}\right)^{1/2} (1 - sin\theta_i)^{1/2} \tag{3.7}$$

Where θ_i is the equilibrium contact angle of the triple line location of liquid i.

Based on the experiments, the right side of the contact angles (Fig. 3.5 for water and Fig. 3.9 for silicone oil) are: $\theta_{silicone\ oil}$ =31.6°, and θ_{water} =26.1°. The measured triple line equilibrium heights on the right side are: $L_{E,silicone\ oil}$ =1.37mm and $L_{E,water}$ =2.80mm. Therefore, the characteristic time can be calculated from Eq. (3.6) as $t_{silicone\ oil}$ =0.2112 s for silicone oil and t_{water} =8.2562 s for water.

The triple line location divided by the final triple line location height can normalize the triple line location height, with time divided by t_i in Eq. 3.6 to the scaled time t/t_i, a new log-log scale can also be plotted in Fig. 3.23.

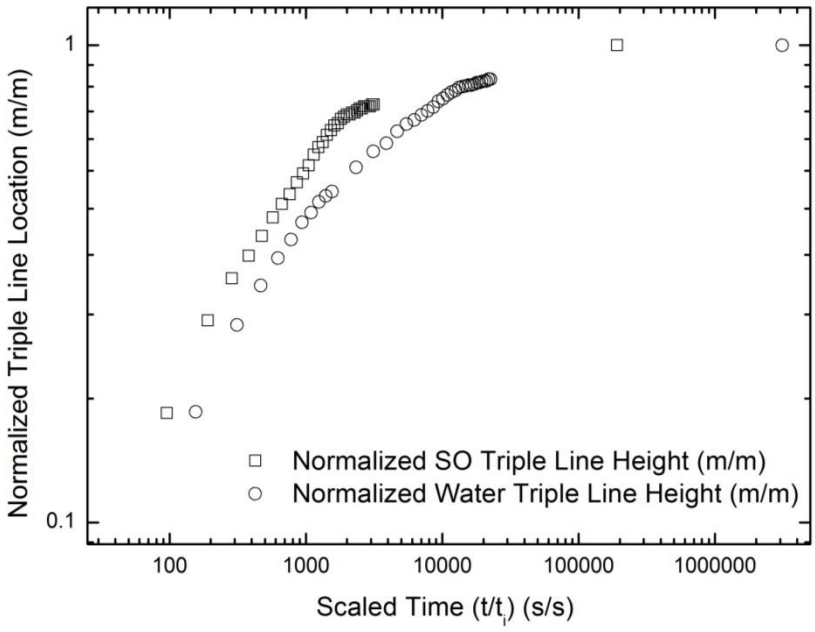

Fig. 3.23 Silicone oil and water scaled time kinetics

It should be noted that the kinetics experiment measurement of triple line location and the equilibrium triple line location are slightly different, see Fig. 3.22, because for water system, the kinetics measurement ends at 1 second for water, and 2 seconds for silicone oil. However, after 1 second for water and 2 seconds for silicone oil, the triple line location still increases slightly in the next a few hundreds of seconds. The equilibrium triple line location height is assumed to be reached earlier than after 5 minutes (when the equilibrium height is considered to be reached). The terminal period of growth of the triple line location, it is assumed, doesn't impact the triple line spreading kinetics since the last stage has passed the capillary-viscous-asymptotic stage (Liu et al., 2011).

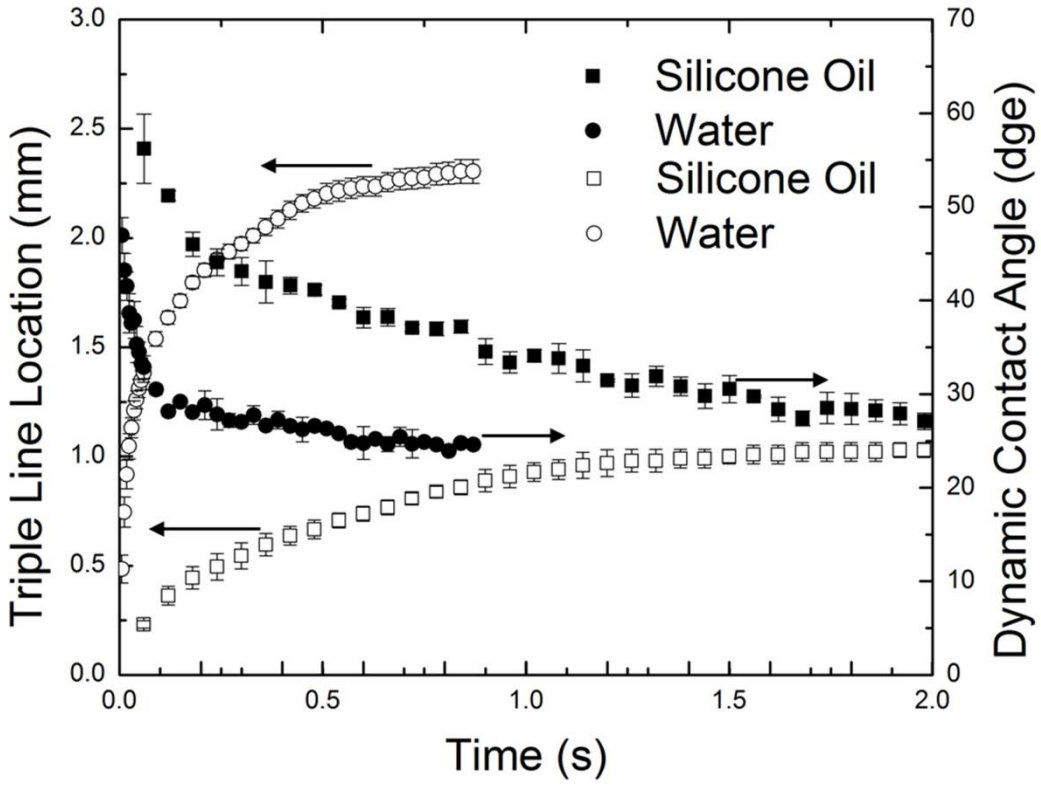

Fig. 3.24 Linear scale of silicone oil and water kinetics with triple line location and dynamic contact angle

In Fig. 3.24, the linear scale of triple line kinetics and dynamic contact angle for both water and silicone oil in the non-reactive systems is plotted. It can be seen that the water system has shorter and faster spreading kinetics, and the triple line location height is higher for water with lower dynamic contact angles. Due to higher viscosity, the kinetics process time is longer for silicone oil.

The model for kinetics of liquid spreading on a solid surface was previously presented by Washburn (1921) as follows,

$$l^2 = \left(\frac{\gamma_{LV}}{\mu}\frac{\cos\theta}{2}\right) rt \tag{3.8}$$

Where l is triple line growth distance, θ is the static contact angle, γ_{LV} is the surface tension between liquid and vapor, μ is the liquid viscosity and r is radius of capillary tube.

It can be noticed that the triple line location is a function of square root of time as:

$$l^2 = \left(\frac{\gamma_{LV}}{\mu}\frac{\cos\theta}{2}\right)At \tag{3.9}$$

Where A is a constant related to geometric shape of the configuration.

If A is taken as 1m, we have

$$l^2 = \left(\frac{\gamma_{LV}}{\mu}\frac{\cos\theta}{2}\right)t \tag{3.10}$$

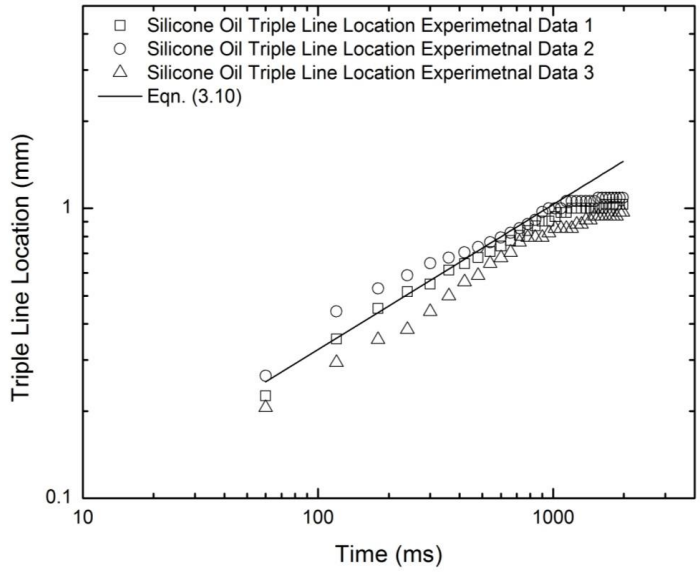

(a)

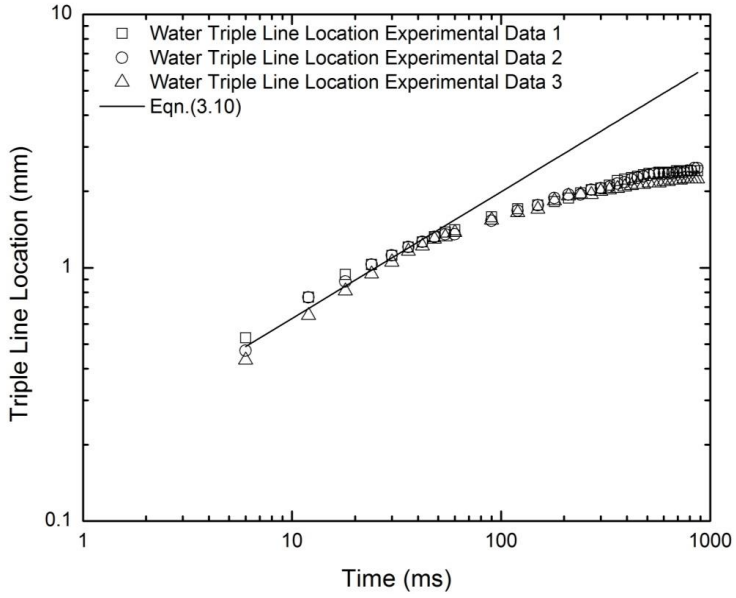

(b)

Fig. 3.25 (a) Silicone oil triple line location dynamics experimental data and Washburn theoretical prediction and (b) water triple line location dynamics experimental data and Washburn theoretical prediction

For both water and silicone oil systems, the constant A is calculated to be 1 m. It can be seen from Fig. 3.25 (a) and (b) that Eq. 3.10 has good agreement in both water and silicone oil systems in the first capillary-viscous stage before the deviation after 500 ms for silicone oil and 40 ms for water. The first stage can be considered as the capillary-viscous stage (Wen et al., 2011) dominated by the balance between surface tension and viscosity, and it covers majority of the spreading on the vertical slide. The square root of time relationship in Eq. 3.10 is obeyed in this stage for both water and silicone oil cases. However, the subsequent stage, known as capillary-viscous-asymptotic stage apparently shows a different power law relationship, see Fig. 3.26(a) and (b). This stage features the $x \sim t^{1/n}$ relation with n~5. In this stage, the surface tension and viscosity impact on the

spreading of the liquid becomes less dominating and eventually is taken over by other factors that are beyond the scope of this study.

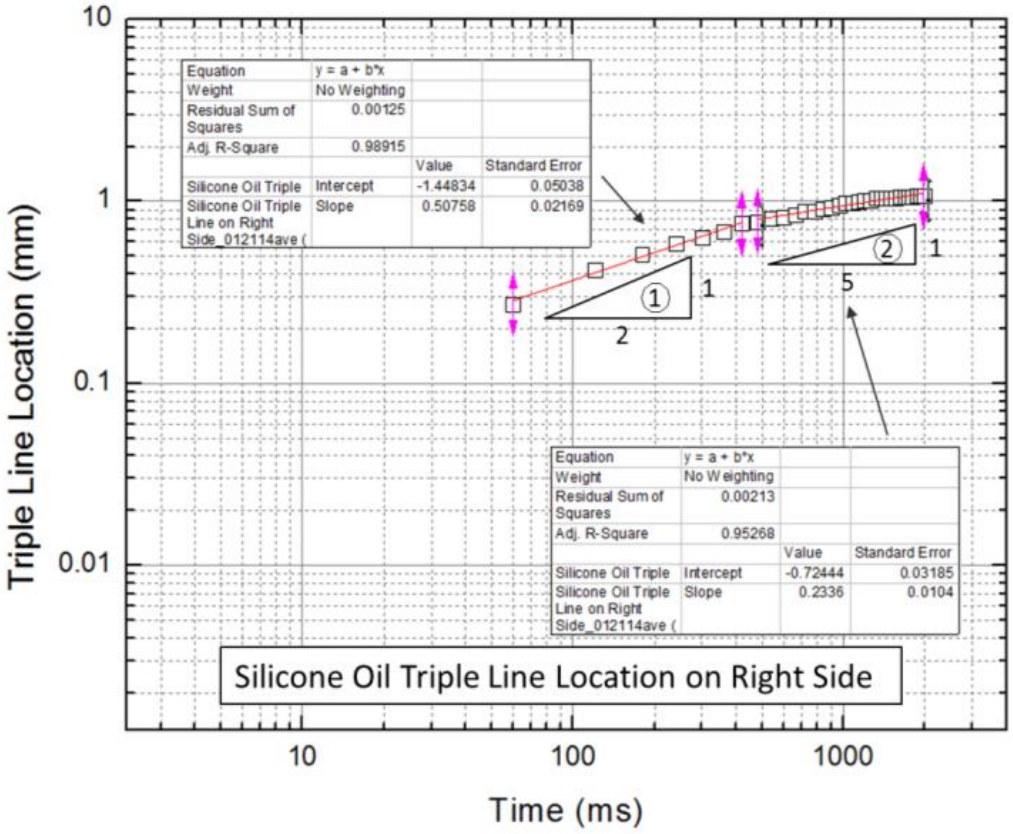

(a)

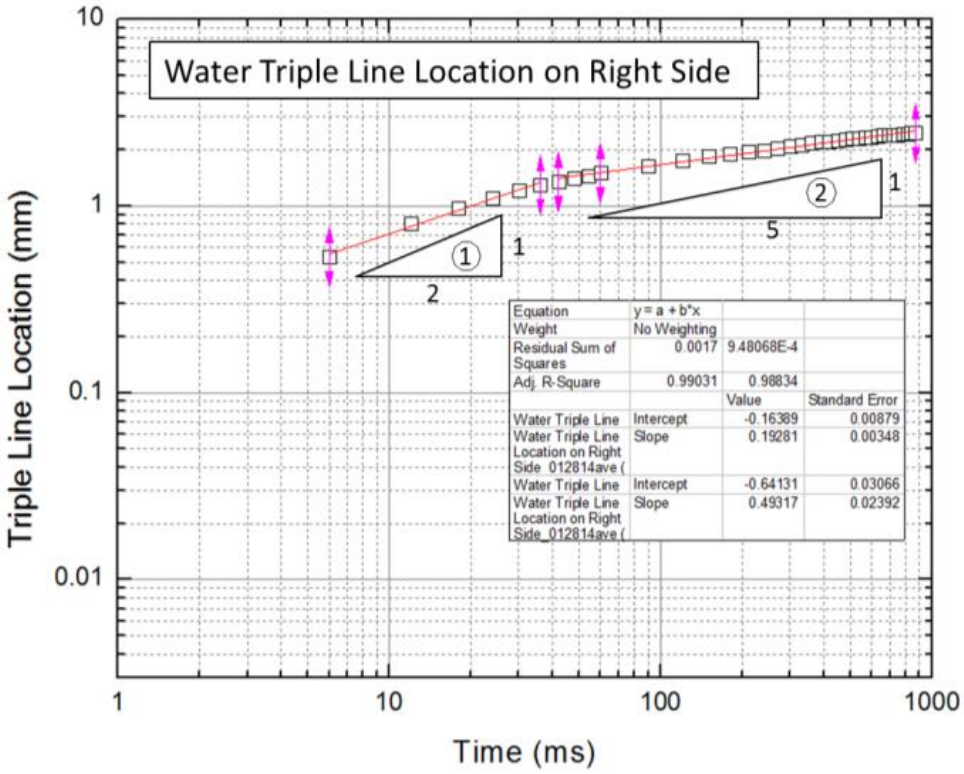

(b)

Fig. 3.26 Triple line location kinetics for silicone oil (a) and water (b) in log-log scales

In Fig.3.26, the experiment data are plotted and it can be noticed that the 5^{th} power law correlation well agrees with the experimental data. The physical explanation of the exact separating point from the two different stages is not clear, therefore the current separating domain size is based strictly on curve fitting shown in Fig. 3.26. The results show that for the silicone oil on glass system, the Washburn type flow spans from the beginning to the 700 ms, however, in the water on glass system, the Washburn type flow lasts from the beginning to 40ms. Both of the systems show that Washburn type flow is the major flow-mode in the spreading on the glass solid surface. The later capillary-viscous-asymptotic

stage has a longer time period, but the triple line location spreading contribution is not major compared to previous Washburn type flow.

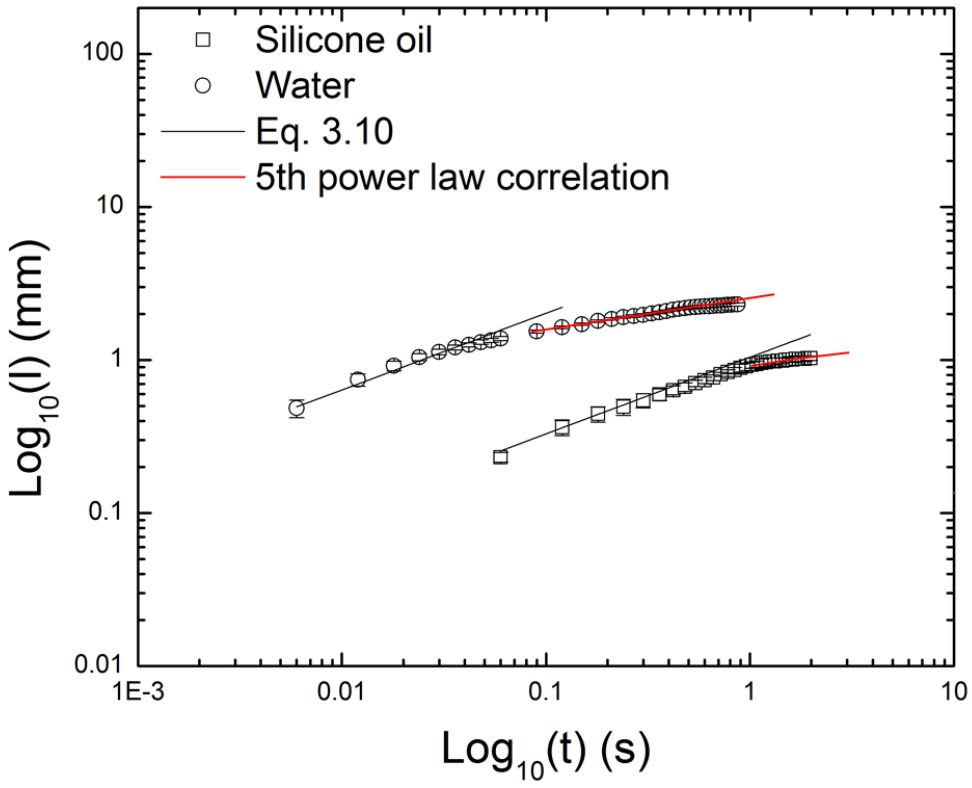

Fig. 3.27 Silicone oil and water triple line kinetics comparison with error bars in log scale

A comparison plot between silicone oil and water is shown in Fig.3.27. The capillary-viscous stage and the later capillary-viscous-asymptotic stage are clearly shown. The capillary-viscous stage obeys Washburn's law of 2^{nd} power law correlation, and the process is dominated by surface tension and retarded by viscosity. The latter capillary-viscous stage obeys the 5^{th} power law correlation, and the process is tending to reach equilibrium.

3.4 Summary

In this chapter, the benchmark experiments of non-reactive liquid wetting systems at low temperatures are presented in a process of designing the experimental methodology for experiments on reactive wetting at elevated temperatures. The benchmark experiment results also serve the purpose of a tool to verify the numerical simulation that is funded by the same collaborative NSF project with the team at the Washington State University (Grant CBET # 1234581 and 1235759).

Two common non-reactive liquid-substrates are used. The liquids spread over the glass wedge-tee configuration to simulate the joint formation configuration to be used for the reactive wetting at elevated temperatures. To establish the reliable database for the non-reactive wetting kinetics, a wetting experiment is adopted to validate the experiment configuration and procedures. In the wetting experiment, the contact angle and the equilibrium triple line location relationship was verified and compared with theoretical results. The experiment data show good agreement with the theoretical prediction for both water and silicone oil systems. The experiment result also shows at a certain given range of liquid layer thicknesses, the triple line location equilibrium height is independent from the liquid thickness. In the kinetics segment of experiments, silicone oil dynamic contact angle and capillary length can agree with the theoretical correlation. The water dynamic contact angle and triple line location correlation feature a deviation when compared to some existing correlations developed earlier and reported in literature. A new modified correlation for water dynamic contact angle and capillary number correlation was established for the water on glass system. The liquid systems wetting also obey the classic Washburn flow model in the capillary-viscous stage, showing the initial

wetting is mainly impacted by surface tension and viscosity. The subsequent capillary-viscous-asymptotic stage shows that for these two liquid systems, a 5th power law correlation can easily be identified. The experiment data error analysis is performed (see associated Appendix A) to explore the potential main causes of data dispersion. The result shows the vertical plate movement of the Wilhelmy plate configuration is having little impact on the triple line kinetics experiment data. The measurement error contributes to a smaller degree to the overall error level compared to the experimental conditions, namely the glass plate surface condition variations and environmental conditions.

CHAPTER 4: EXPERIMENTAL EQUIPMENT AND PROCEDURES FOR THE HIGH TEMPERATURE CAPILLARY FLOW STUDY

4.1 Overview

Chapter 4 is mainly focused on the experiment preparation, equipment and procedures for the reactive wetting at elevated temperatures. As mentioned in Chapter 2, sessile drop experiment method is a major method to investigate the liquid spreading and wetting phenomena due to its simplicity and yet thoroughly coverage of both contact angle and triple line location behavior. The experiment preparation and procedures introduced in this chapter offer general guidelines of the preparation method and procedures for experiments presented in later chapters. Various experiments will involve different sample designs, preparations and procedures, but the overall intention of all the experiments is to generate data for a study of the molten metal spreading at high temperatures with the same experiment equipment and its accessories.

The Optical Contact Angle Analyzer (OCA) is the main piece of equipment used in the molten metal spreading research. It is assembled in the *Brazing, soldering and heat exchangers research laboratory* at the Institute of Sustainable Manufacturing at University of Kentucky. Other experiment facilities include scanning electron microscope (SEM), optical surface profiler, and differential scanning calorimeter (DSC) at University of Kentucky.

Typical sample design and preparation examples will be illustrated in this chapter along with the corresponding general experiment procedures. Post-experiment samples

handling following the solidification of the molten metal and analysis will also be included along with brief SEM result.

4.2 Experiment Configuration

Most of the experimental data obtained in this segment of the research plan are from the customized Optical Contact Angle Analyzer. The high temperature contact angle measurement facility is a unique system, manufactured by DATA PHYSICS, a combination of OCA-15 LHT and HTFC 1200 and subsequently customized in-house for being able to be supplied by the background controlled atmosphere (in this case, ultra-high purity Nitrogen, 99.999) and equipped with an enhanced temperature measurements capability, see Figs. 4.1 and 4.2. The hot zone system is positioned on an optical table and it is fully controlled by a dedicated computer system, including the hot zone/sample temperature measurements, the heating rate and the peak temperature control, followed by the image processing. The hot zone in the Joule-heating driven cylindrical furnace can be rotated around the vertical axis for up to 90 degrees via the dedicated clamp at the base for a secure loading of the samples. A Dee-Tubing 96% purity alumina purchased from Coorstek was placed in the furnace chamber for the purpose of stabilizing the sample platform. The furnace is positioned so that the camera, hot zone axis and light source are all in a perfect horizontal alignment. Two hot zone end ports are sealed with specially designed water cooled flanges, hence sealing the ceramic tube in the heating zone while at the same time being cooled through jacketed heat exchange flange chambers. Thus, the water cooling system provides the specified temperature levels of the quartz glass windows, imbedded into the end port flanges. The additional cooling system, external to the hot zone interior, prevents the exterior of the furnace from heating up

extensively. The hot zone atmosphere is strictly controlled in the process to eliminate oxidation, an issue causing wetting restrictions (Eustathopoulos et al., 2005). Ultra-high purity nitrogen (99.999% N_2) is connected through the flange's gas inlet ports with the hot zone chamber space. The outlet of the Nitrogen with any eventual effluents' stream is connected to a trace oxygen analyzer made by Teledyne Analytical Instruments. The K-type thermocouple is extended through a flange to the data acquisition system including National Instruments DAQ-9172 module connected to the LabView data acquisition software support installed on the control functions dedicated computer. The hot zone and the CCD camera are controlled by SCA20 software from FDS Corp, see Fig. 4.3. Images and videos are handled by SCA20 as well as VirtualDub.

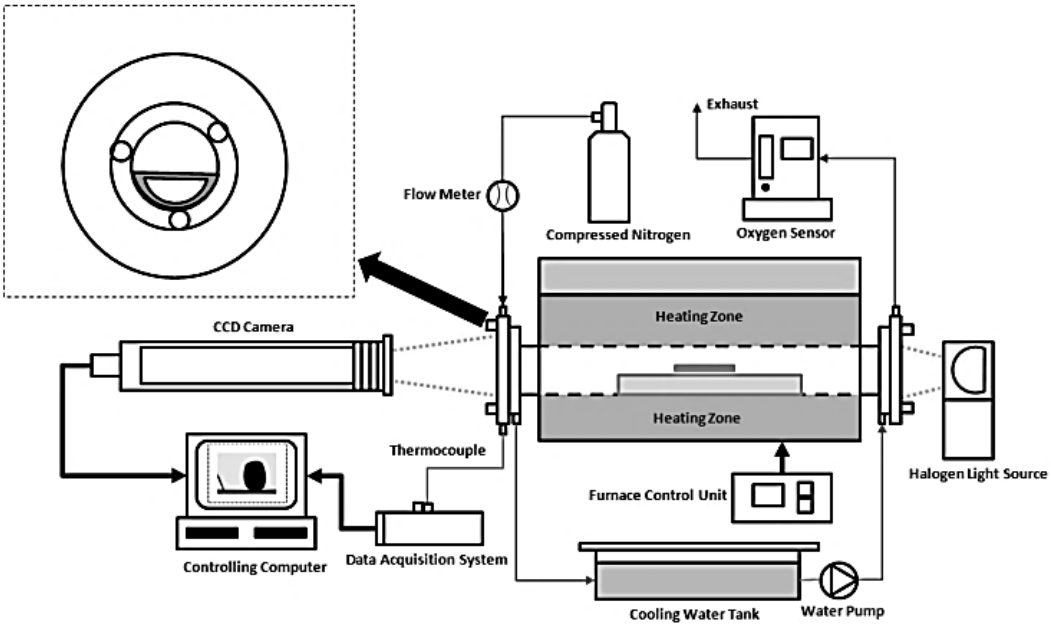

Fig. 4.1 High temperature contact angle measurement system's schematic diagram

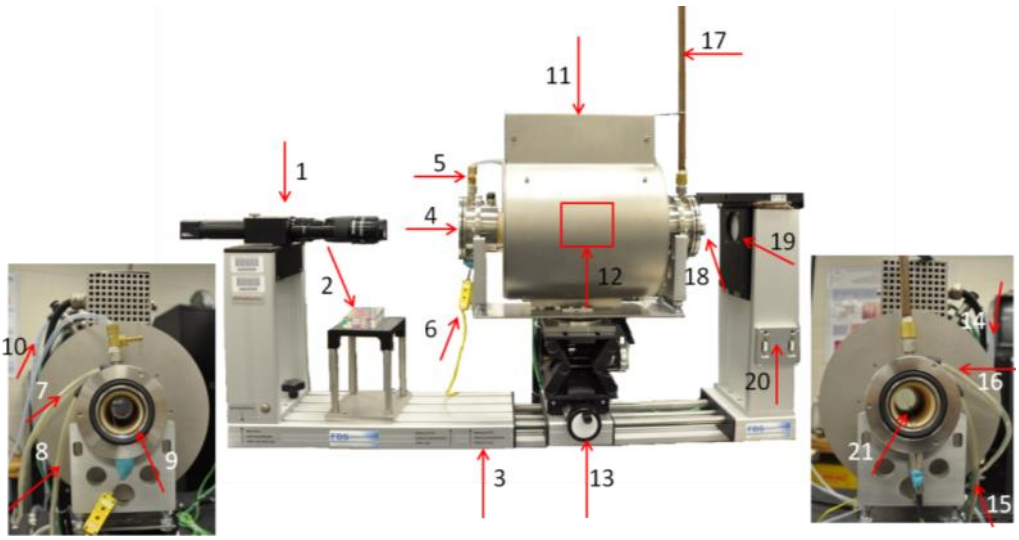

Fig. 4.2 OCA system facility

1-CCD camera 2-Bubble level 3-Frame 4-Quartz glass window (Left) 5-Purging gas inlet valve 6-External thermocouple 7 -Flange water cooling inlet (Left) 8-Flange water cooling outlet (Left) 9-Thermally conductive ceramics tube 10-Furnace top cover water cooling outlet 11-Furnace 12-Hot zone/Sample location (Inside) 13-Furnace rotation knob 14-Furnace top cover water cooling inlet 15-Flange water cooling outlet (Right) 16 -Flange water cooling inlet (Right) 17-Exhaust gas outlet pipe 18-Quartz glass window (Right) 19-Halogen light 20-External USB ports 21-Built-in thermocouple

As shown in Fig. 4.2, the high temperature furnace (designation 11, operational up to 1700 K) has the inner diameter of 35 mm and length of 300 mm so that it can easily accommodate a single test sample at a time. The hot zone (12) is visually unobstructed in the axial direction (4-18) except for the presence of the test specimen and its supporting structure. A halogen light source (19) delivers a homogeneous visible light flux and is located on one side (a far-end) of the hot zone to illuminate the ceramic inner tube space, obstructed from the field of vision of the front camera only by a test sample contour. So,

the sample's side shade view is visible from the opposite side of the hot zone as a black contour image on a white background. Additional ports for the background atmosphere gas supply and exhaust exits are included (5 and 17). Transparent side windows allow on one side an access to the light source illuminating the hot zone, and on the other side to a telescope (1) for digital camera recording of the shadow image. The two flanges are sealing the ceramic tube of the heating zone and are also cooled by the water cooling system (7.8 and 15, 16). This cooling system prevents the exterior of the oven, as well as the lateral windows ports, from an excessive heating. The temperature ramping speed can be controlled by SCA20 by setting different temperature ramps, see Fig. 4.4. The maximum temperature ramp can be reached by the hot zone is 40°C/min. It should be noted that SCA20 doesn't have the limit of temperature information. Thus by setting the temperature heating rate higher than 40°C/min could only result in 40°C/min of heating rate in the physical heat zone by the heaters. The default heating rate by the system is also 40°C/min as tested by various experiments.

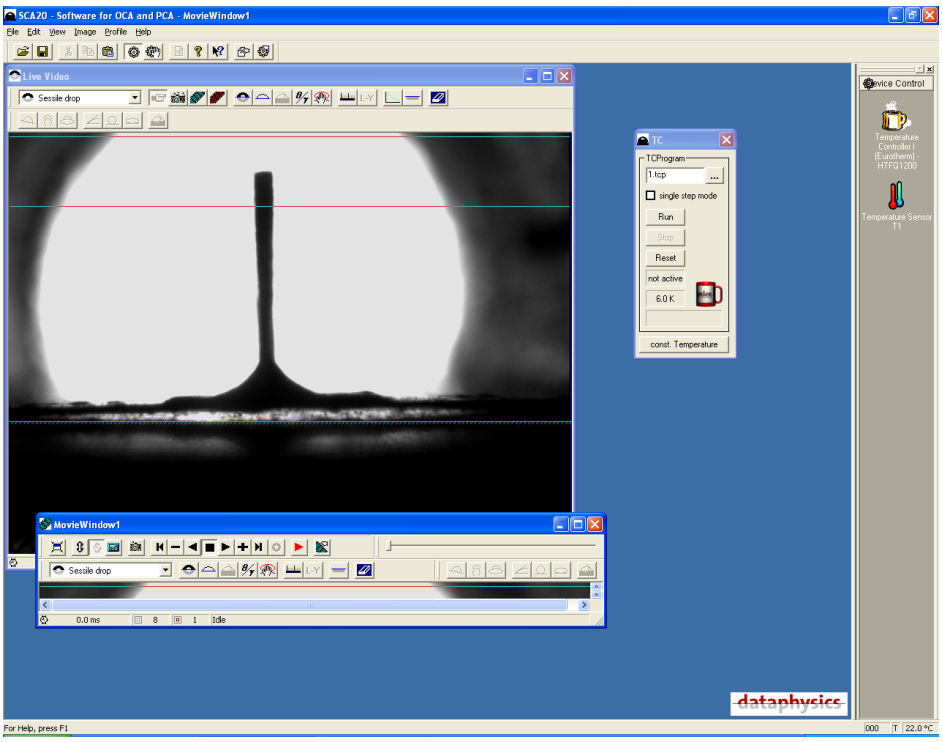

Fig. 4.3 Operation screenshot of SCA20 software

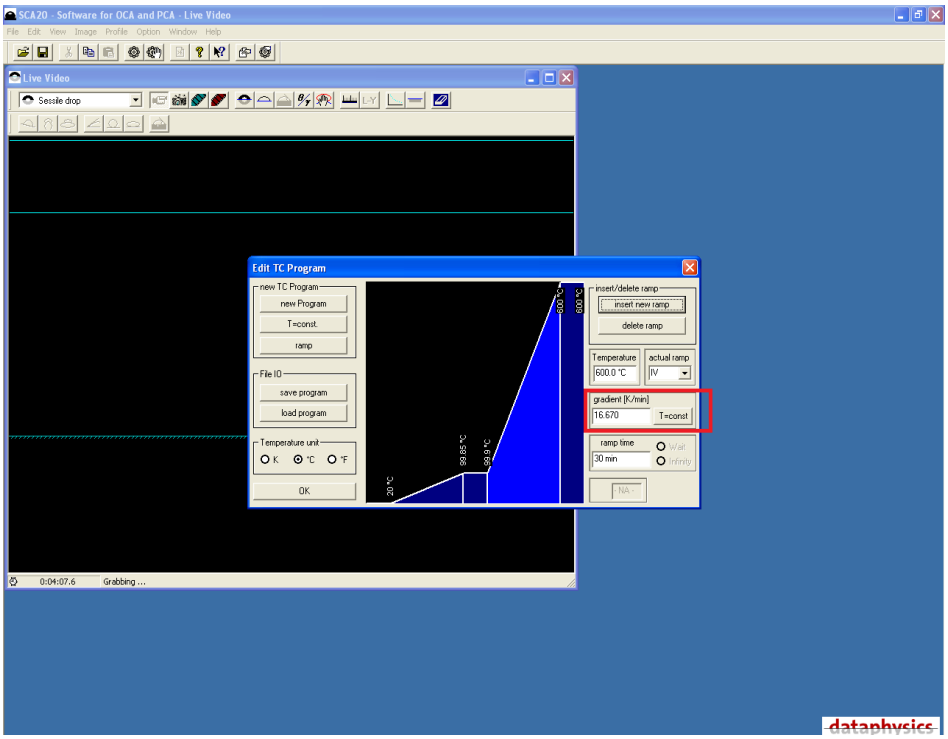

Fig. 4.4 Temperature settings screenshot of SCA20 software

4.3 Sample preparation

As mentioned in Chapter 2, the "fluxless" material (i.e., the material that has the flux imbedded, not added over the surface) has many advantages over the traditional brazing fillers. Thus the self-fluxing material developed by Sapa Group (Ogilvy et al., 2014) and registered as Trillium^{TM} is used in this research. Trillium is a patented (proprietary) Al-Si alloy (AA4045) with 9 to 11 wt% Si mixed with approximately 2 to 3 wt % potassium-fluoro-aluminate as inorganic salt (Ogilvy et al., 2014; Hawksworth et al., 2015). The substrate and the vertical plate are both made of AA3003, including 1wt%-1.5 wt% Mn. Based on the TrilliumTM material, various samples are designed and prepared for the reactive wetting at elevated temperatures. Generally, for the kinetics study of the reactive wetting process, the wedge-tee type of sample configuration is adopted with different material configurations with various thicknesses, so that the joint formation kinetics can be both visually and analytically studied with the aid of the SCA20 software. For the surface tension and contact angle study, the classic sessile drop configuration is used in the experiment for both wetting and non-wetting cases. All raw materials, i.e., clad brazing sheet, AA3003 sheet, and pure aluminum wires or stainless steel wires, were first manually cleaned with soap water ultrasonically for ~ 2 minutes, then with water ultrasonically for ~ 2 minutes and with 95% ethanol ultrasonically for ~ 2 minutes in order to eliminate oil and/or chemical residues. The materials were dried in air for subsequent use. The K-type thermocouple is normally placed close to the point of interest within 15 mm radius, but not affected by the liquid flow during the experiment, see Fig. 4.6

4.3.1 Wedge-tee type of sample preparation

The wedge-tee type of sample design is made in order to simulate the real heat exchanger configuration of two pieces of aluminum perpendicular to each other. The test sample consists of two mating surfaces: (1) an Al alloy vertical surface (a AA3003 sheet), and (2) an Trillium^{TM} clad over an AA3003 core surface (a brazing sheet), see Fig. 4.5 and Fig. 4.6 for the sample assembly configuration.

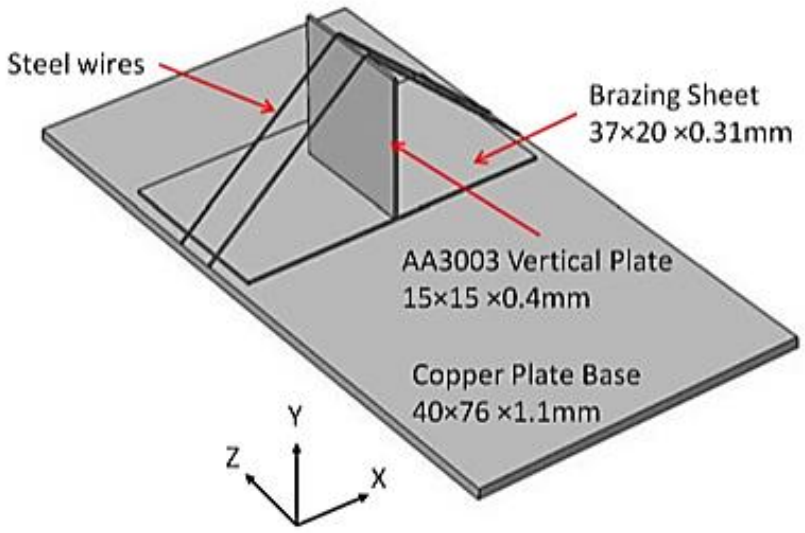

Fig. 4.5 Wedge-tee sample 3-D configuration of 0.03 thickness Trillium^{TM} clad metal

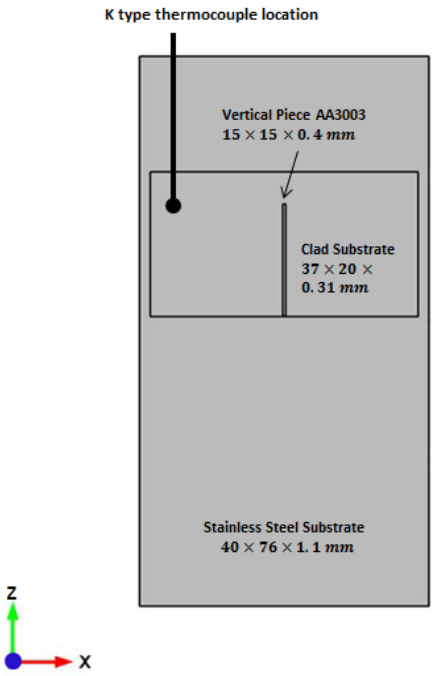

Fig. 4.6 XY plane view of wedge-tee sample configuration of 0.03 thickness Trillium^{TM} clad metal

The typical wedge-tee configuration samples in this research as shown in above figures have the base stainless sheet of $40 \times 76 \times 1.1\ mm$, which is used to fix the location in the furnace for the clad substrate with dimensions of $37 \times 20 \times 0.31\ mm$. The vertical piece is AA3003 sheet with dimensions of $15 \times 15 \times 0.4\ mm$. The vertical piece is fixed on the substrate by using two stainless steel wires of a diameter of 0.3mm. As mentioned earlier, all these materials are pre-cleaned before assembled into the wedge-tee configuration. The sample is positioned in the furnace chamber in such a way that the clad brazing sheet is horizontal with a deviation of up to 1.5°. The angle (Fig. 4.7) between vertical AA3003 piece and the horizontal clad brazing sheet is controlled to be 90° ± 1.5°. Each sample was positioned in the furnace chamber so that the brazing sheet level deviates by up to maximum 1.5° from the horizontal. Consequently, it is assumed

that a small geometrical deviation of the verticality has a minimal impact on the kinetics of the triple line movement, as well as on the overall evolution of the molten metal joint fillet formation.

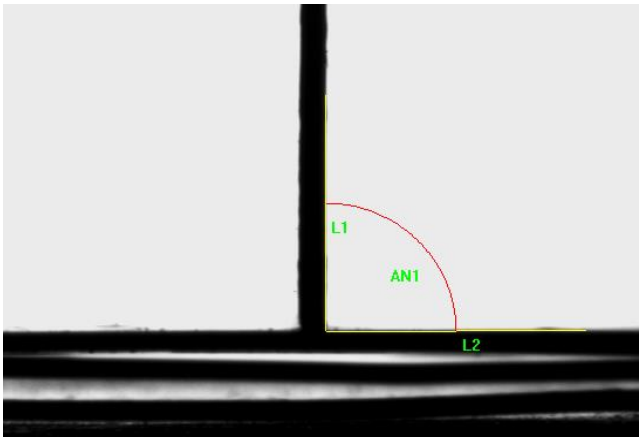

Fig. 4.7 Configuration of the vertical piece and clad substrate

An SEM image of the AA3003 vertical sheet surface is shown in Fig. 4.8 (a). A cross-section through the horizontal brazing sheet is given in Fig. 4.8(b). The roughness of the AA3003 sheet is 0.43 ± 0.08μm, measured by Zygo New View TM 7300 3D Optical Surface Profiler, see Table 4.1. Measurements are performed at 20 different locations on the sheet. It can be observed that the AA3003 surface of the vertical sheet features a pattern of multiple microgrooves formed during the sheet manufacturing (the hot rolling traces). These microgrooves do not feature a high ridges and deep valleys topography to be able to impact the spreading. Moreover, the surface features have a uniform, directional distribution and in this case would not act as capillary channels (as verified by the performed tests). Placing an AA3003 mating surface with more pronounced microgrooves perpendicular to the horizontal substrate may, in principle, significantly enhance the spreading (as opposed to the case with micro grooves parallel to the

substrate). The related research (Liu et al., 2012) implies no groove impact in the present case. Still, the microgrooves pattern of the AA3003 sheet was adjusted so that the directional topographical features are oriented perpendicularly to the horizontal substrate.

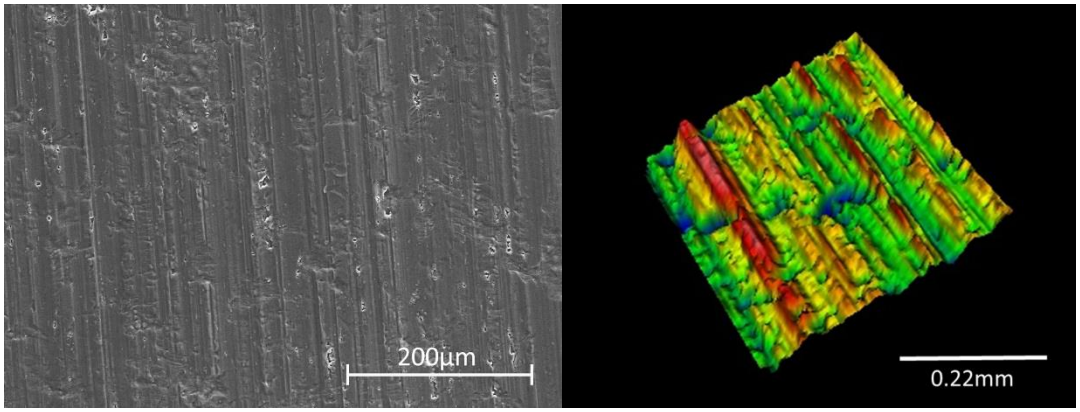

(a) (b)

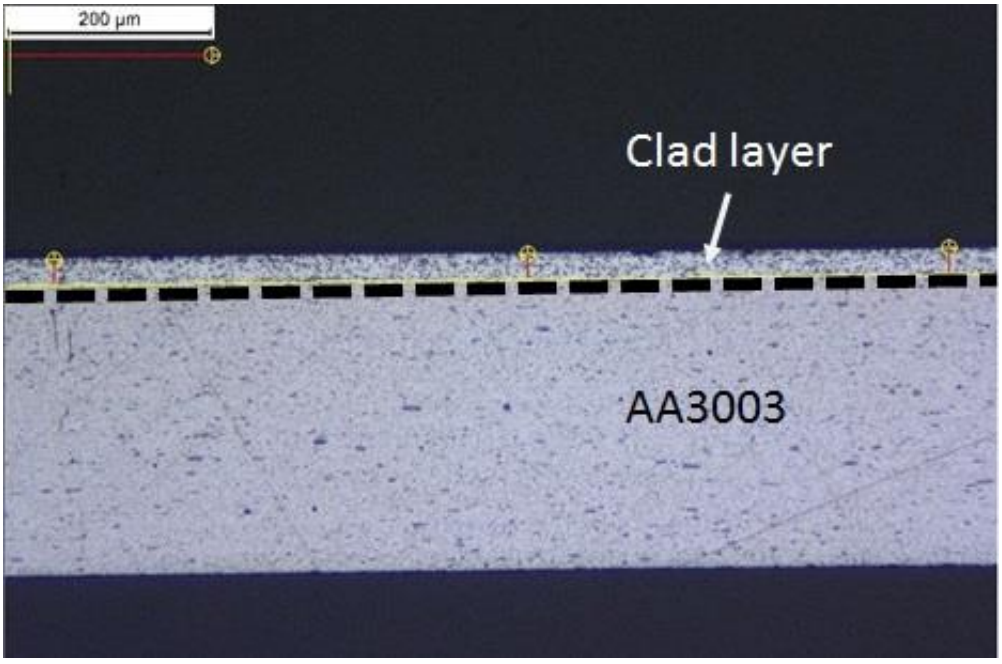

(c)

Fig. 4.8 (a) The surface topography of the AA3003 substrate measured by Hitachi S-3200-N Scanning Electron Microscope; (b) 3D scanning image of topography of AA3003 substrate measured by Zygo New View TM 7300 3D Optical Surface Profiler; (c) Brazing sheet cross section structure (horizontal mating surface, Fig. 4.5)

Table 4.1 Surface roughness of AA3003

Measurement	Surface Area (mm^2)	Surface Roughness Ra (μm)	Average Surface Roughness Ra (μm)
1	0.1936	0.41	0.43 ± 0.08
2	0.1936	0.293	
3	0.1936	0.292	
4	0.1936	0.317	
5	0.1936	0.449	
6	0.1936	0.449	
7	0.1936	0.358	
8	0.1936	0.395	
9	0.1936	0.392	
10	0.1936	0.369	
11	0.1936	0.508	
12	0.1936	0.538	
13	0.1936	0.515	
14	0.1936	0.557	
15	0.1936	0.481	
16	0.1936	0.456	
17	0.1936	0.571	
18	0.1936	0.448	
19	0.1936	0.46	
20	0.1936	0.425	

Compared to the 0.03 thickness Trillium^{TM} clad metal wedge-tee configuration, a similar wedge-tee configuration is also used for the kinetics of molten metal spreading study, see the comparison in Fig. 4.9.

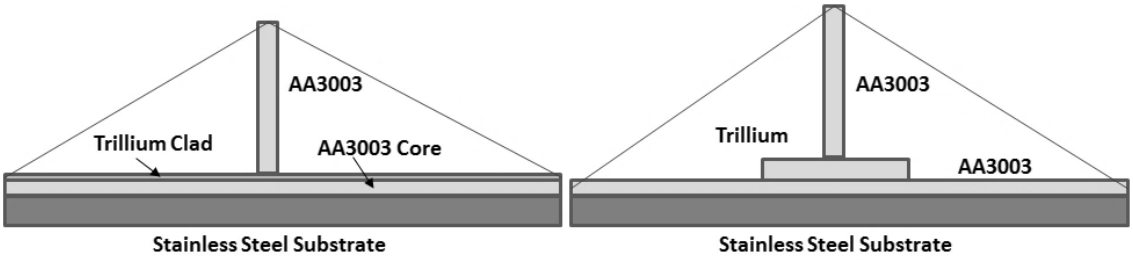

(a) (b)

Fig. 4.9 Aluminum alloy spreading test samples. (a) 0.03 mm thickness Trillium^{TM} clad configuration, (b) 0.4 mm thickness Trillium configuration

As shown in Fig. 4.9, the other wedge-tee configuration design is intended for the thicker Trillium^{TM} clad metal.

4.3.2 Sessile drop sample preparation (non-wetting case)

In order to study physical properties of the Trillium^{TM} clad metal, the sessile drop experiment is designed. Different from previous AA3003 substrate, a non-wetting substrate of alumina is used in the sessile drop experiment. The alumina substrates are of a 96% purity and they are of an excellent planarity quality (with artifact scratches less than 0.0005cm depth) and a superior surface finish (camber<0.003mm/mm). The alumina substrate samples were acquired from Coorstek in size of 114mm×114mm× 1.1mm. The ceramic sheet was cut by a laser cutter from the Workshop and Digital Fabrication Lab in College of Design of University of Kentucky into 38mm×114mm×1.1mm substrate in order to fit into the furnace. Trillium^{TM} clad metal in this type of experiment is cut into cubes so that it can be positioned on the alumina substrate for melting purpose. The materials are soaked into soap water, washed with water and 95% ethanol in ultrasonic pool for 2 minutes respectively.

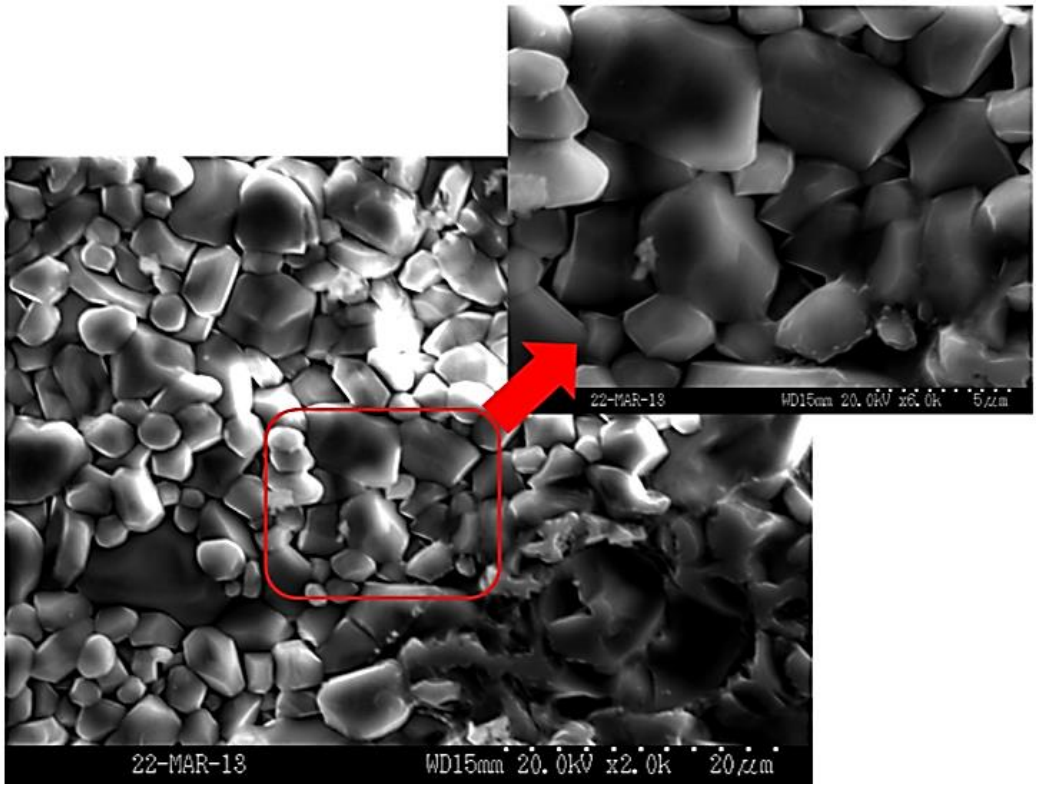

Fig. 4.10 The surface topography of the alumina substrate scanned by Hitachi S-3200-N Scanning Electron Microscope

An SEM image of the alumina substrate surface (Fig. 4.10) is obtained by the Hitachi S-3200-N Scanning Electron Microscope from The Electron Microscopy Center of the University of Kentucky. The surface composition was also analyzed by EDS (Energy Dispersive Spectrometer), see Fig. 4.11 and Fig. 4.12.

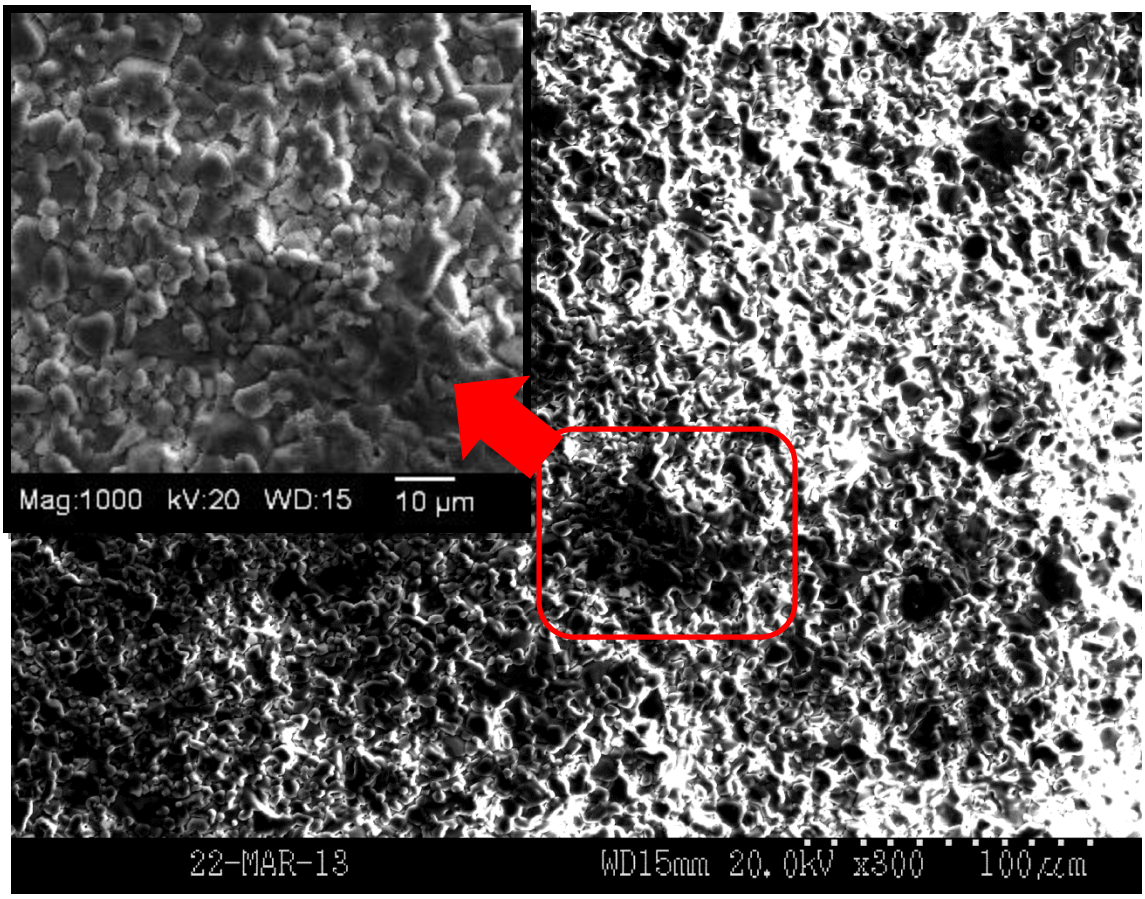

Fig. 4.11 The surface topography of the alumina substrate measured by Hitachi S-3200-N Scanning Electron Microscope for EDS analysis area

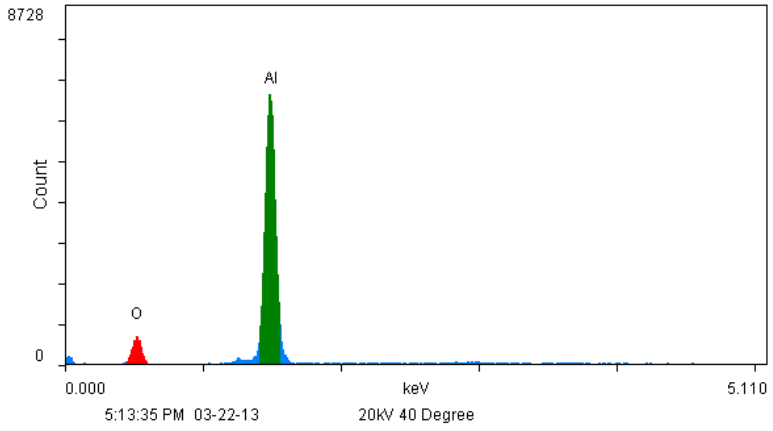

Fig. 4.12 Alumina substrate area spectra from Fig. 4.11

As shown in Fig. 4.12, the alumina surface represents a composition of AlO_2 as specified.

The roughness of the alumina surface is measured by Zygo New View TM 7300 3D Optical Surface Profiler, see Table 4.2. The average surface roughness (*Ra*) of the alumina is 5.679 μm ±0.736 μm. 20 measurements are taken at different random locations of the alumina plate surface. The 3D scanning image of topography of alumina substrate measured by Zygo New View TM 7300 3D Optical Surface Profiler is shown Fig. 4.13 (a). The scanning intensity map of the topography of alumina surface is shown in Fig. 4.13 (b).

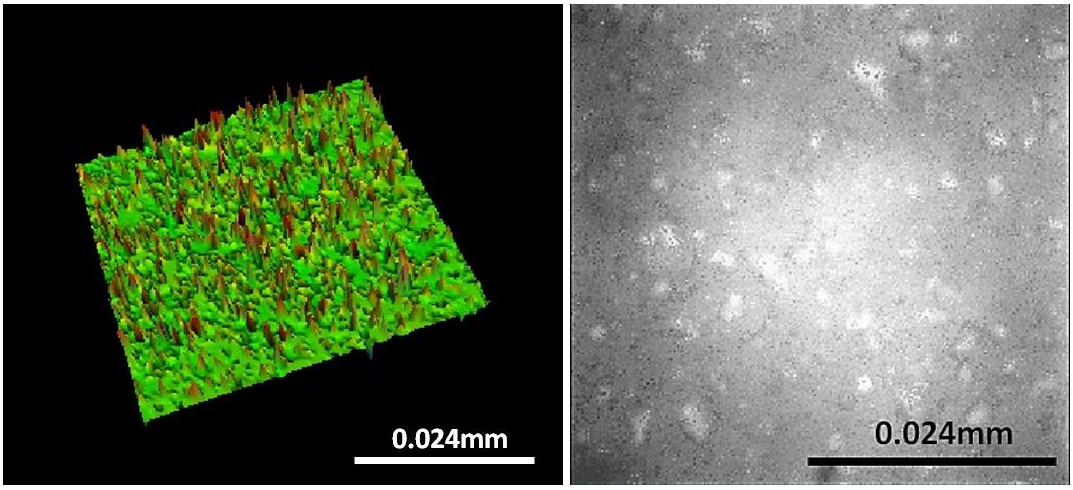

(a) (b)

Fig. 4.13 3D scanning image of topography of alumina substrate measured by Zygo New View TM 7300 3D Optical Surface Profiler; (b) 3D scanning intensity map of topography of alumina substrate measured by Zygo New View TM 7300 3D Optical Surface Profiler

Table 4.2 Surface roughness of alumina

Measurement	Surface Area (mm^2)	Surface Roughness *Ra* (μm)	Average Surface Roughness *Ra* (μm)
1	0.0484	4.816	5.679±0.736
2	0.0484	4.95	
3	0.0484	5.671	
4	0.0484	6.657	
5	0.0484	6.6	
6	0.0484	6.61	
7	0.0484	7.199	
8	0.0484	6.071	
9	0.0484	5.006	
10	0.0484	5.205	
11	0.0484	5.175	
12	0.0484	6.02	
13	0.0484	6.042	
14	0.0484	6.215	
15	0.0484	5.003	
16	0.0484	6.014	
17	0.0484	5.21	
18	0.0484	4.802	
19	0.0484	4.766	
20	0.0484	5.548	

4.4 Experiment procedures

4.4.1 Wedge-tee configuration and sessile drop experiment

In the wedge-tee configuration of kinetics experiments, as shown in Fig. 4.1 and Fig. 4.2, a sample assembly is placed in the center of the ceramic tube on the Dee shape tube platform within the hot zone after the sample is cleaned and assembled. Before the start of an experiment as well as during and after heating, the hot zone is purged with ultra-high purity nitrogen (99.999% N_2). The furnace chamber was purged with ultra-high purity nitrogen for no less than 2 hours with a flow rate of $1.38\times10^{-5} \pm 0.06\times10^{-5}$ kg/s. Thus, with the constant flow rate, in 2-hour time frame, the volume of the hot zone in the

ceramic tube can be replaced for up to ~30 times. Tests were not triggered until the oxygen level in the furnace chamber has reached below 80 ppm. During the entire process of the joint formation, the oxygen level is below 80 ppm and continuously recorded by the oxygen sensor. The data collection of the temperature vs. time starts from the onset of the heating process. The CCD camera starts to record the joint formation at the temperature of 570℃ and ends at the temperature of 590℃. During the test time period, the wedge-tee joint will start to form primarily within the 120 seconds of the video recording. The controlled temperature does not have an appreciable effect on the kinetics of the joint formation. The CCD camera records the joint formation process with a frame rate of 5 f/s before the measured sample temperature reaches the melting point of the clad. Hence, the whole period of the kinetics of the T-Joint formation process is recorded. After the heating time is completed, the hot zone cools down by natural convection.

Similar to non-reactive spreading kinetics process method, the recorded video is extracted to different frames of process before being imported to Image-Pro© for measurement.

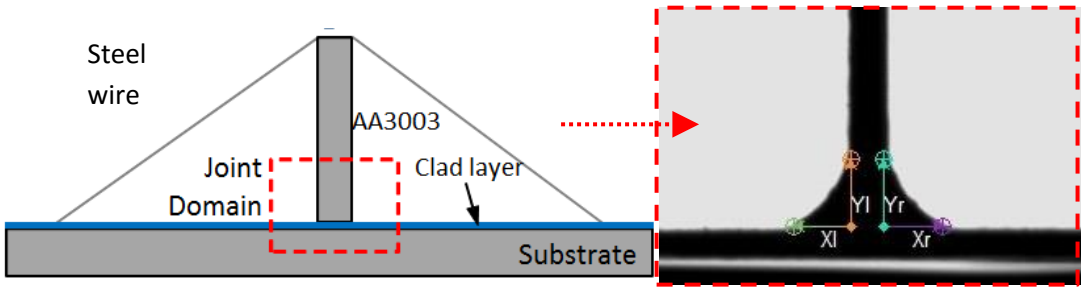

(a) (b)

Fig. 4.14 (a) Joint domain configuration and (b) vertical/horizontal length of the joint

As shown in Fig. 4.14 (a) and (b), the vertical direction of both left and right (Yl and Yr) as well as the horizontal direction of both left and right (Xl and Xr) are all measured in the frames for triple line location and dynamic contact angles.

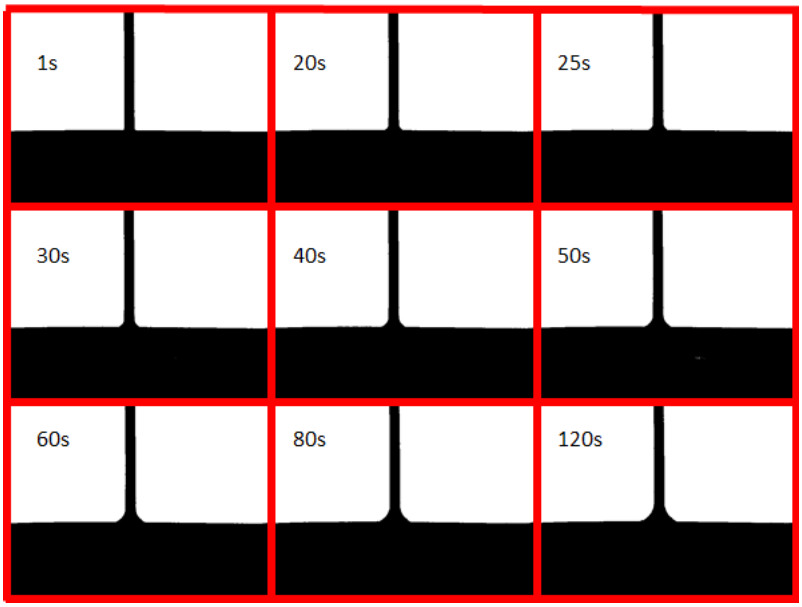

Fig. 4.15 A selection of image sequences decomposed from a recorded movie indicating the evolution of joint formation with time (0.03mm thickness Trillium™ of experiment 091212)

Image-Pro© provides the Tracking Objects function for tracking the distance of the targeted object in a given time. Once the starting point is chosen, the tracking point could travel with the growth of T-Joint formation manually, and the accumulated distances can be recorded accordingly. The data can be exported to the spreadsheet for analysis. This method is efficient for a large quantity of images, easily increasing the sample data population. The starting point location would not change once it's chosen, thus reducing the measurement errors. An example of the Image-Pro© screenshot is shown in Fig. 4.16.

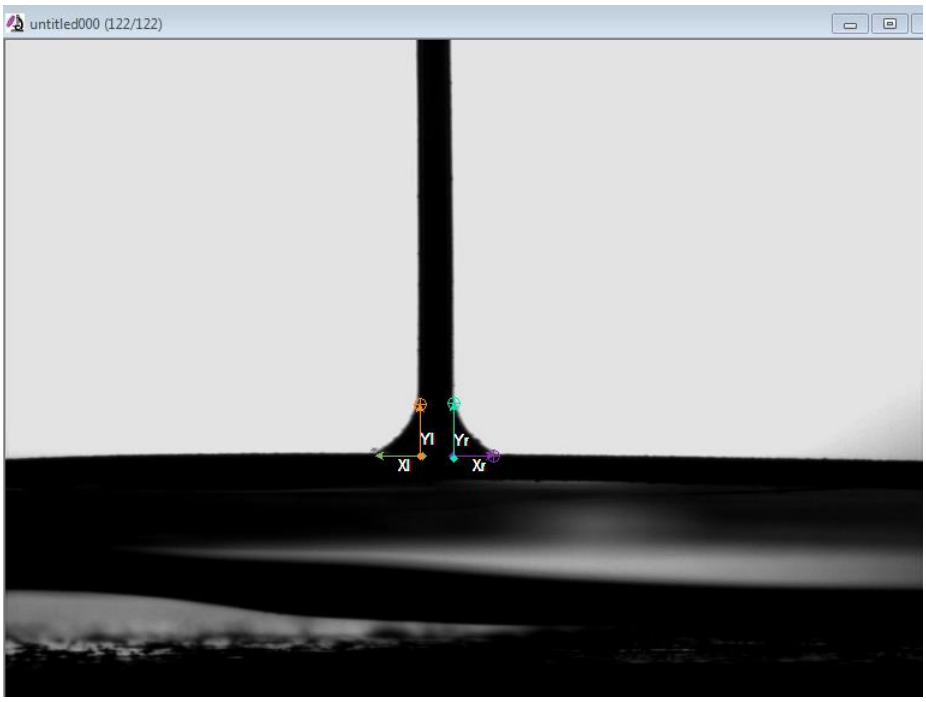

Fig. 4.16 Tracking objects method (experiment 091212)

In the sessile drop experiment, the similar procedure is conducted. In order to keep the Trillium^{TM} at the molten state, the temperature is gradually increased to 620°C. The cube metal melted at 600°C to form the spherical shape. The oxygen level is kept below 70 ppm. The temperature span during the measurement was from 603.8°C to 606.6°C, with a temperature ramp rate of 0.028°C/s. After the image frames are exported from the video, ImageJ is used to calculate the sessile drop contact angle and the capillary constant c ($c = \Delta\rho \cdot g/\gamma$, m^{-2}), which was implemented as a Java plug-in for the ImageJ software, see Fig. 4.17.

The calculation of the surface tension was based on Dorsey method (Dorsey, 1928; Anson, 1999).

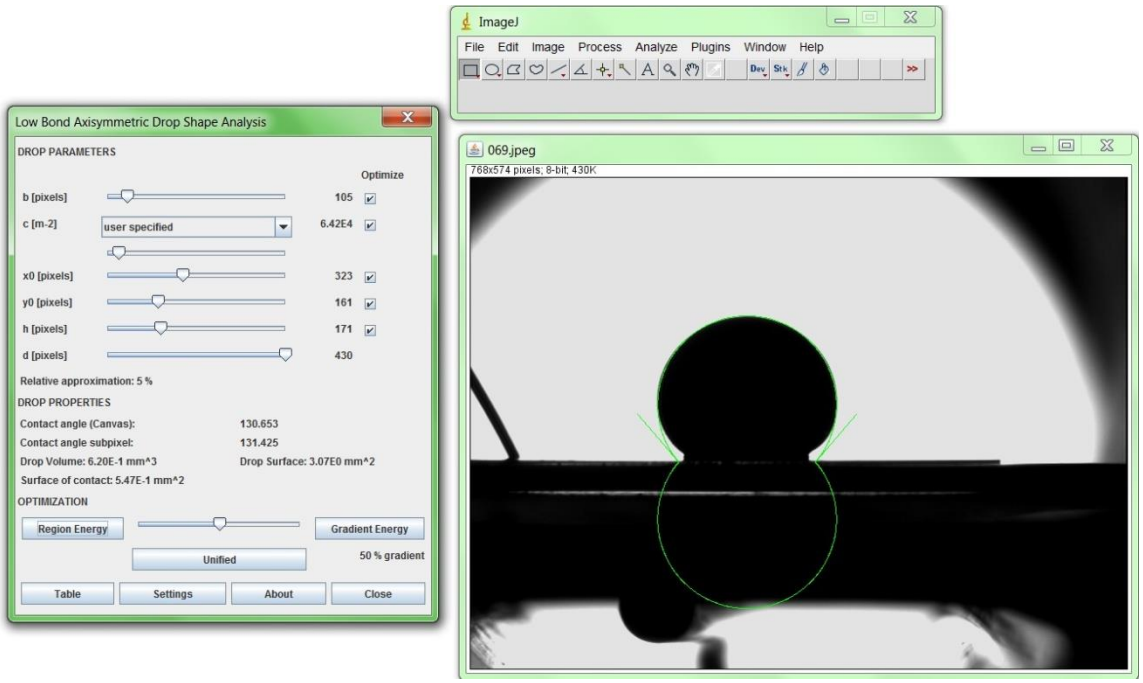

Fig. 4.17 ImageJ low-bond axisymmetric drop shape analysis sample

4.4.2 OCA furnace FLIR infrared camera temperature phenomenology

In order to verify the temperature distribution uniformity for the wedge-tee configuration samples in a qualitative manner, a dummy sample is made (Fig. 4.18) so that the infrared camera can be used to visualize the temperature distribution within the interested area. Aluminum 1100 rod with diameter of 3.15 mm and length of 10 mm was prepared in the configuration shown in Fig. 4.18. The aluminum 1100 rod and the clad substrate were first manually cleaned with 95% ethanol and then ultrasonically cleaned with 95% ethanol for ~ 2 minutes in order to eliminate oil or chemical residues prior to the experiment.

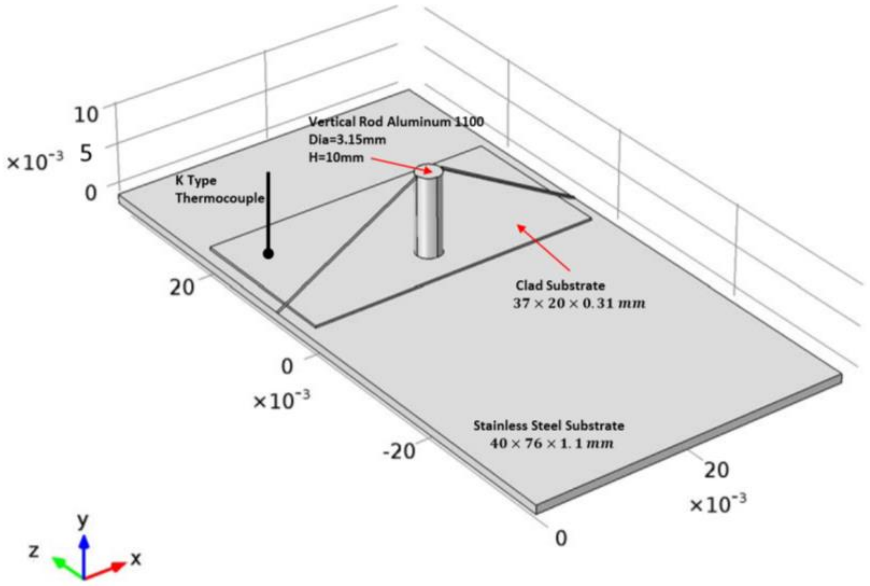

Fig. 4.18 Dummy sample configuration

AFLIR SC640 infrared camera was fixed at the z-axis 0.5 m away from the furnace entrance so that the infrared images of the wedge-tee joint location can be taken, see Fig. 4.19. Due to the presence of the reflection impacting the IR imaging from the terminal glass window at the front entrance of the furnace, the experiment was run under atmosphere conditions without glass blocking the front view. The target temperature was set to 595℃. The images were taken at time intervals of 20 seconds. The IR images were calibrated based on the measured thermocouple temperature with the associated FLIR software. 5 images selected at temperatures of 577℃, 580℃, 585℃ and 590℃ (measured by the thermocouple) were analyzed by the IR camera. The infrared images are shown in Fig. 4.20.

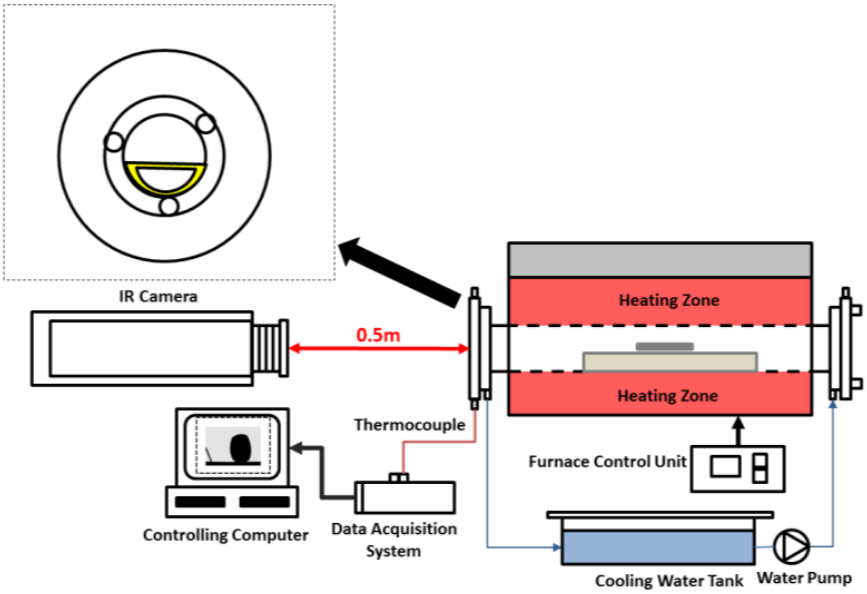

Fig. 4.19 Infrared camera setup in the OCA system

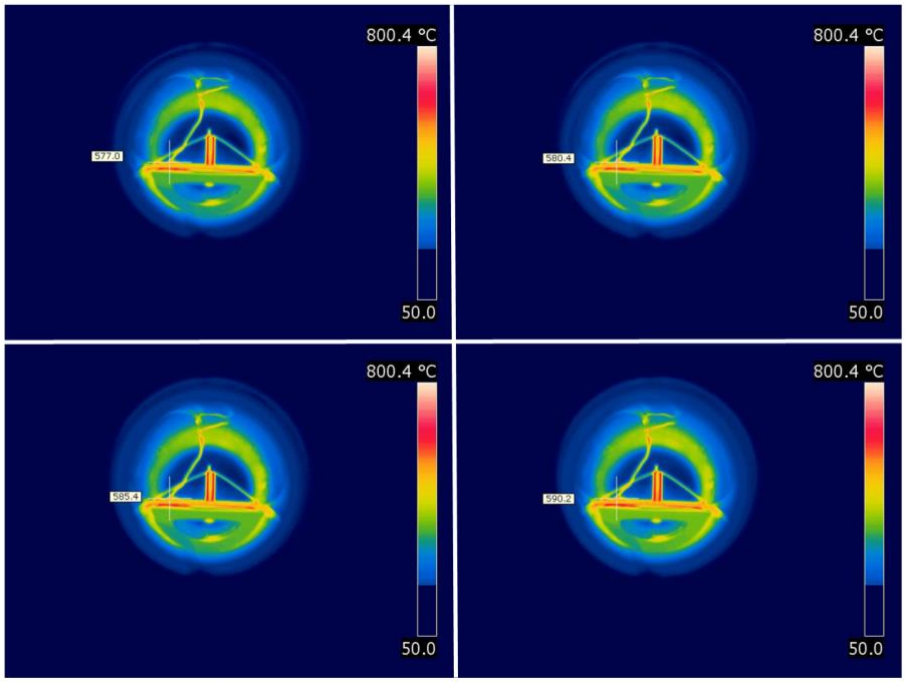

Fig. 4.20 IR Image of the temperature distribution of the wedge-tee joint formation

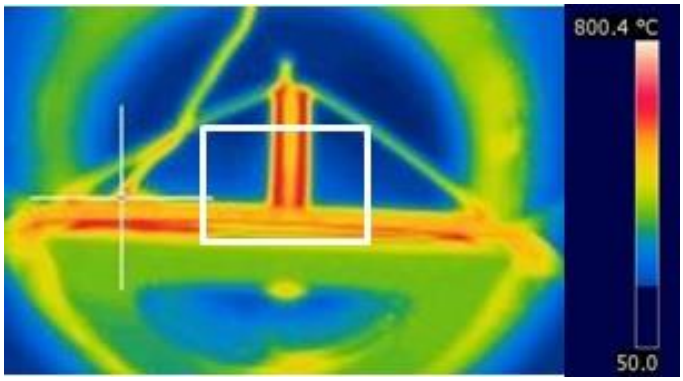

Fig. 4.21 Symmetric temperature distribution of the wedge-tee joint region

The temperature distributions of the wedge-tee configuration at/above clad metal melting point are mostly symmetric except for the thermocouple location where the temperature is higher due to more heat conducted from thermocouple to the thermocouple location. However the distance between the thermocouple and the joint formation interested region justifies the fact that the slight temperature difference caused by the thermocouple does not affect the temperature distribution of the interested area (see Fig. 4.21). The interested region of the wedge-tee joint location has a symmetric temperature distribution as shown in Fig. 4.21.

4.5 Summary

In this chapter, the main OCA equipment is presented along typical sample preparation and experiment procedures. For different experiment purposes, different experiments needed to be designed and conducted. The general procedure introduced in this chapter is established and was available for studies presented in the following chapters.

Two major experiment studies for reactive wetting at elevated temperatures are introduced: the uniquely designed wedge-tee configuration and the classic sessile drop

experiment. The description of the first type of the experiment includes the general configuration of the wedge-tee shape for all the studies in the later chapter. The latter (non-wetting over Alumina surface) experiment is design to study the physical properties of the interested patented material, namely the surface tension and contact angle of Trillium^{TM}. Similarities and differences are introduced between these two experiment setups and procedures. The data analysis processing are explained in the last section of this chapter. The validation of the uniform temperature distribution of the wedge-tee sample configuration is illustrated in the last section, showing the OCA furnace capable of providing the environment for the wetting study at elevated temperatures.

Chapter 5 will focus on the wetting process based on sessile drop experiment, and Chapter 6 will discuss the wedge-tee sample configuration of wetting kinetics study at elevated temperatures.

CHAPTER 5: WETTING OF MOLTEN CLAD METAL ON WETTED AND NON-WETTED SURFACES

5.1 Overview

This chapter mainly focuses on the experimental study of the molten clad metal, namely Trillium^{TM} wetting on either wetting surface or the non-wetting surface. Phenomenological observation, data analysis and the reviewed literature validation will be discussed here. As the general experiment facility, preparation and procedures have been introduced in the previous chapter, only specific difference of the experiment preparation and procedure will be commented on in this chapter.

The wetting of molten Trillium^{TM} on wetting surface and non-wetting surface was studied with the Optical Contact Angle Analyzer (OCA), see Chapter 4 for details. The sessile drop experiment configuration was adopted to study the physical properties of the molten clad metal at elevated temperatures needed for modeling in latter stages of this project work (see Appendix E). In the wetting surface case, the substrate used is the same material (AA3003) that will be used in studies in the following chapter. Thus studying the simple sessile drop spreading on the wetting surface gives the preliminary insight into the physical characteristics of the molten clad metal at elevated temperatures. In the non-wetting surface case, alumina substrate was used in the sessile drop experiment configuration for the molten clad metal to form the spherical liquid metal shape to facilitate measuring the unknown surface tension as well as its contact angle based on the low-bond axisymmetric drop shape analysis (LBADSA) (Stalder et al., 2010). Note that the molten metal considered represents a novel alloy (composite) and literature data for surface tension were considered a priori non reliable for this case. The molten sample

cross section images were analyzed by SEM and EDS to confirm the eventual liquid penetration and dissolution of the substrate (existing in the wetting case), and more complicated de-oxidation, chemical reaction and inter-diffusion phenomena shown in the non-wetting case. The measured value of surface tension for the new material (namely Trillium^{TM}) was validated by comparing evaluated surface tension data to the known experiment values from multiple different literature sources of similar metal alloy systems.

5.2 Experimental study of the molten clad metal at elevated temperatures

As mentioned earlier, the sessile drop configuration was adopted to study the phenomenological analysis of the molten clad metal wetting process. The prepared samples were placed on the Dee shape tubing, so that the heating chamber can be purged with ultra-high purity nitrogen (99.999% N2) for more than 2 hours with a flow rate of 1.38×10-5 ± 0.06×10-5 kg/s. Tests were not triggered until the oxygen level in the furnace chamber has reached below 60 – 80 ppm. The CCD camera starts to record when the clad metal Trillium^{TM} is melting at its melting temperature of $580 \pm 5℃$. The frame rate of the recoding CCD camera was 25 frames/s. The recorded video was extracted into Image-Pro© as well as ImageJ for measurement of surface tension and contact angle.

5.2.1 Molten clad metal wetting on the wetting surface – preliminary tests

To ensure the equilibrium state of the liquid clad metal under nearly isothermal state at the peak temperature, the molten metal, formed from a solid alloy sample, initially cut into a 0.1979 g cube, was positioned on the AA3003 substrate. The run lasted

approximately 45 minutes before the video ended recording. The gas condition was kept within 100 ppm during the whole process. During the recording time, the temperature profile of the molten clad metal is shown in Fig. 5.1.

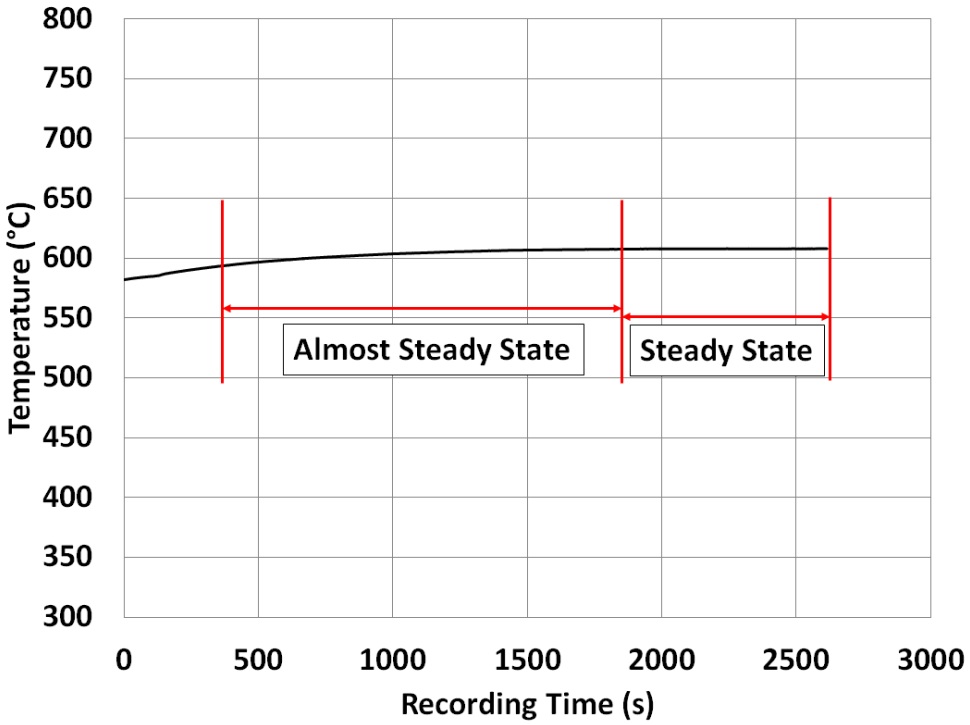

Fig. 5.1 Temperature profile of the sessile drop in the experiment of the wetting surface

As seen in Fig. 5.1, after the clad metal has melted, to avoid potential solid clad metal existing in the sample, the temperature continues to rise to over 605 °C while the sample is maintained in the near isothermal state. Images were taken at the so established isothermal state for data analysis.

Fig. 5.2 A snake-based approach to the measurement of the contact angle

The snake-based approach was used in the ImageJ to measure the contact angle of the molten Trillium^{TM} on the wetting substrate of AA3003. Both left and right sides were measured from 604℃ to 607.9℃ when the molten liquid has virtually reached its stable (equilibrium) state. The average measured contact angle is 6.9°±2.7°, see Table 5.1. The measured experimental contact angles will be used for theoretical analysis discussed in the Appendix B and C.

Table 5.1 Contact angle measurement results of wetting surface

T(°C)	time (s)	Contact Angle left (°)	Contact Angle right (°)	Measured times
607.9	2615	6.1	4.8	1
		9.3	4.4	2
		2.8	2.4	3
606	1351	8.2	4.8	1
		10.0	4.8	2
		6.1	9.1	3
605	1186	9.0	14.0	1
		8.4	10.0	2
		4.4	9.0	3
604	1056	6.1	6.0	1
		7.7	7.6	2
		4.3	6.4	3
Total Average		6.9	6.9	
Standard Deviation		2.26	3.15	

5.2.2 Molten clad metal surface tension review

Multiple literature sources involving surface tension of aluminum and aluminum alloys data were reviewed and summarized in this section to compare with the measured surface tension value of the molten clad metal.

Experimental data for the aluminum alloys' and pure aluminum's surface tensions were identified in a number of literature sources, but the surface energy $\gamma_{sv}$and the crystal-melt interfacial energy γ_{sl} were only available (to the best knowledge of the authors at the present time) from the stimulation models (Aqra et al., 2012), see Appendix C. The most referred to and the most frequently used aluminum surface tension data was from Keene (1993). The data summarized by Keene (1993) were considered to be a set of the recommended aluminum surface tension values. The mean surface tension of pure

aluminum at the melting point of 660℃ is 871 mNm^{-1}(Keene,1993). Without the presence of oxygen, the value tends to be a bit higher of the order of magnitude of 1050-1100 mNm^{-1}(Sarou-Kanian et al., 2003) (oxygen would decrease the magnitude of the surface tension). From the existing experimental data, the surface tension may be considered as having a linear relationship with temperature.

The experimental surface tension measurement result has been compared to the literature data, as shown in Fig. 5.3. Multiple measurements were taken in two independent tests in current experiments. As shown in Fig. 5.3, both theoretical values are drawn as two straight lines from Keene (1993) and Egry et al. (2001). Keene (1993) used curve fitting from previous experiments to get the empirical equation for the surface tension of aluminum prediction. The solid line in Keene (1993) is predicting the value from 660 ℃ to 710 ℃ with his experimental values. The dashed line of Keene (1993) is below 660 ℃ with the assumption that the surface tension obeys the linear trajectory below 660 ℃. The linearity assumption is further verified by Egry's (2003) theoretical dotted line with his temperature range from 620 ℃ -1150 ℃. Other literature references of the aluminum and its alloys surface tensions at 660 ℃ and 700 ℃ are plotted in the figure. The surface tension ranges from 0.7 N/m to 1 N/m.

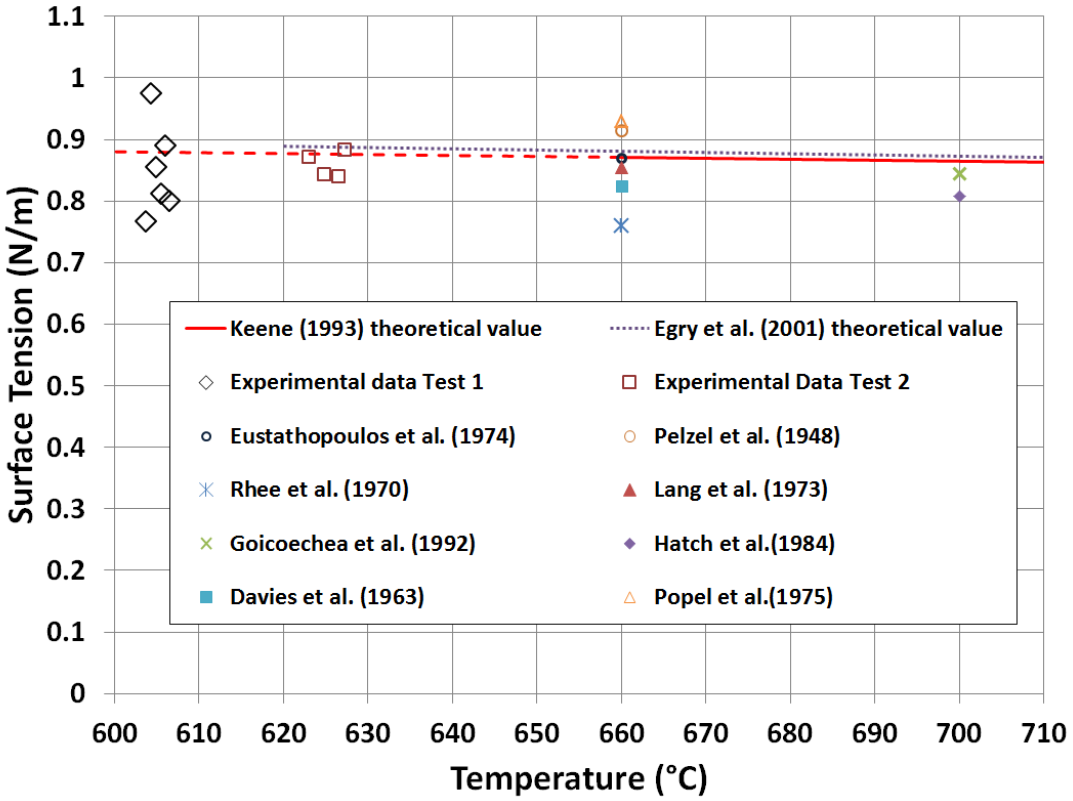

Fig. 5.3 Trillium^{TM} surface tension experimental result comparison

Within the predicted linear range, our experimental results from both tests show the surface tensions in the acceptable range vs. the previous literature values.

5.3 Analysis of the sessile drop triple line region

The sessile drops on the non-wetting surface (aluminum on alumina), and the case of the wetting surface (aluminum on aluminum) were both tested and the cross sections of both drops were prepared for the optical imaging as well as SEM analysis. Eustathopoulos et al. (1974) stated that for the reactive wetting, continuous layers of a new compound can be formed leading to better wettability by the liquid metal than is the initial substrate. In the non-wetting case, the liquid aluminum alloy (Trillium^{TM}) over alumina substrate (Fig.

5.4 and a zoomed in Fig. 5.5) show that at the triple line location, a dark colored formation was present as a separate region.

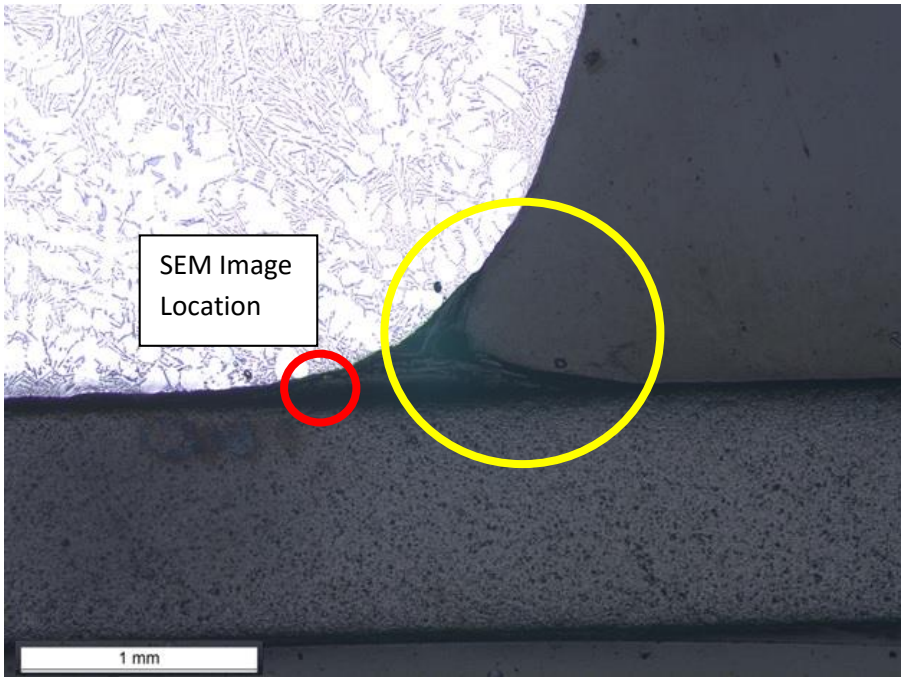

Fig. 5.4 Non-wetting sessile drop triple line region on alumina

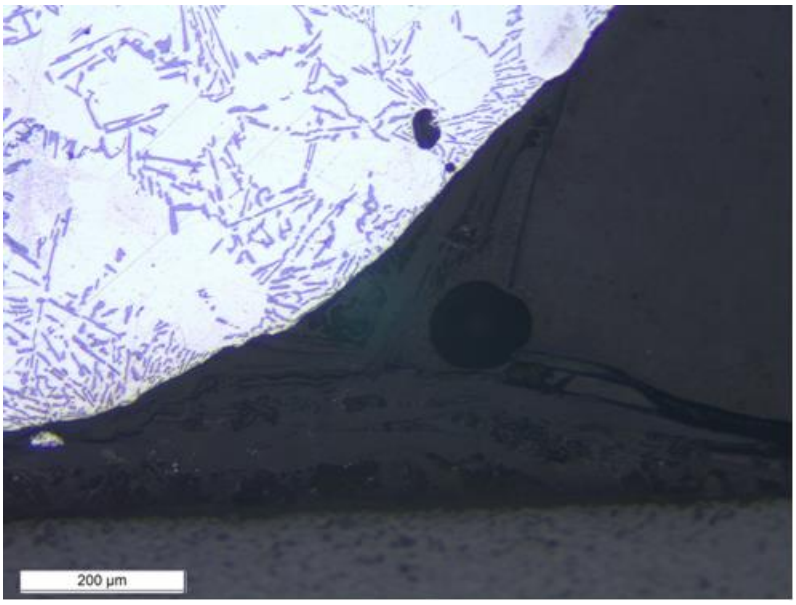

Fig. 5.5 Non-wetting sessile drop triple line region on alumina

Three major element compositions can be seen in the optical images: the brighter aluminum silicone alloy (clad metal), the darker potassium-fluoro-aluminate (flux) at the triple line region, and the dark gray alumina. It is assumed that the molten clad/flux salt was accumulated at that location during the spreading of the molten clad metal drop since this aluminum alloy is doped with potassium-fluoro-aluminate flux that melts before the Al-Si only alloy. To clarify that assumption, an SEM image was taken by SEM 3200 at the triple line area of the non-wetting sessile drop. The SEM image was taken at the region where three major compositions exist, see Fig. 5.6. 5 spots in the SEM image were taken for EDS analysis for the chemical analysis to represent the present elements. The result is shown in Table 5.2 and Fig. 5.7.

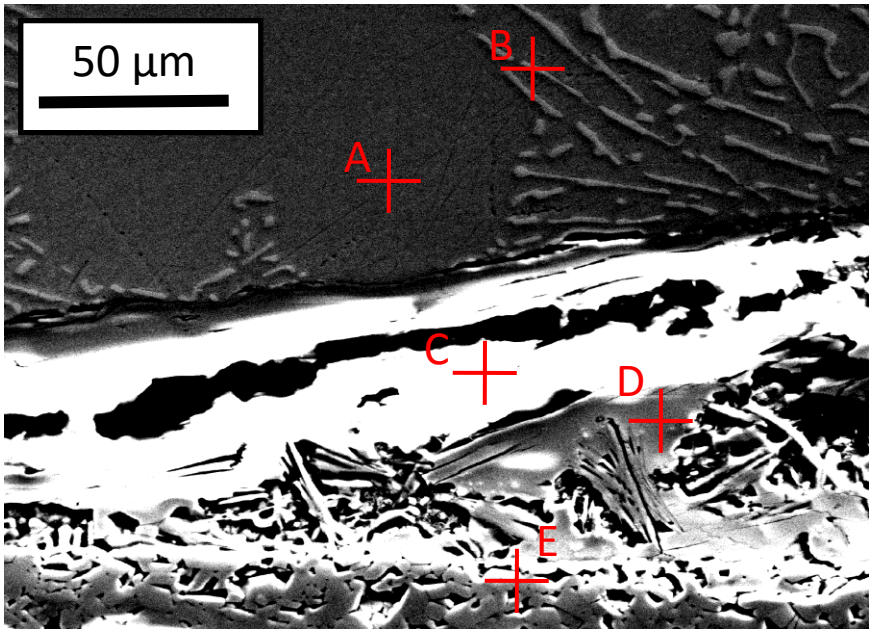

Fig. 5.6 SEM image of non-wetting sessile drop triple line region

Table 5.2 Chemical composition for different points in the triple line (refer to Fig. 5.6)

	Al (wt%)	Si (wt%)	K (wt%)	F (wt%)	O (wt%)
A	97	1	2		
B	72	25	2		
C	13	31	50	5	
D	30	2	59	9	
E	90				10

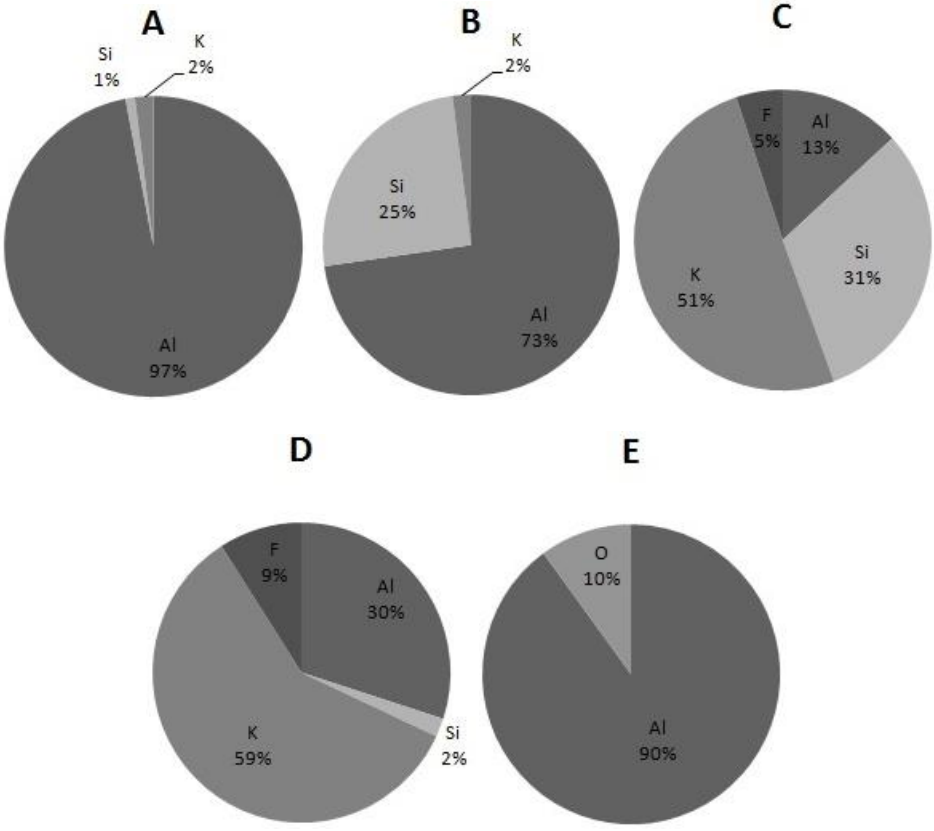

Fig. 5.7 Chemical composition at different locations in the triple line region

Point A represents the domain of an alpha phase of the re-solidified aluminum alloy featuring 97% Aluminum. This is fully in agreement with the re-solidified microstructure formation that corresponds to the alpha phase. However, multiple lighter stripes are noticed in the clad metal area and the point B shows that there is up to 25 wt% Si in the area. These domains represent the re-solidified needle-like phase domain close to the

eutectic or, more precisely above the eutectic composition. The white phase area, C, features a rich potassium domain of 51% of K, with the lowest Al content (13%) and the highest Si content (31%). Yet another domain, point D features the highest potassium level of 59 wt%. The surface of alumina as represented by point E shows that the composition for the alumina surface didn't change during the spreading or the re-solidification process of the molten clad metal drop. The porous configuration of the alumina surface shown in Fig. 5.6 has verified the roughness of the surface configuration.

As assumed, the result verifies that the first dark region is composed of aluminum-silicone alloy with minor potassium. The middle region where the triple line region is positioned (both C and D) features a large amount of potassium which corresponds to the potassium-fluoro-aluminate flux. The bottom region is proven to be alumina shown as E in the table, see Fig. 5.6.

Based on the EDS result, it can be stated that during the spreading of the sessile drop (due to the lower melting point of the brazing flux of potassium fluoride, as well as silicon contained in the clad metal), a layer of liquid flux is formed on the surface of the liquid molten clad metal preventing oxidation. A large amount of the flux accumulates at the triple line region. It is speculated that the molten clad metal spreads primarily across the exposed alumina surface, and in the process squeezes the liquid accumulation of the flux in the triple line area, forming complex multilayered phases observed in Fig. 5.6.

In the wetting case, the triple line region is relatively simple (based on the images taken by the optical camera, see Fig. 5.8 and Fig. 5.9). The clear alpha phase aluminum and eutectic phase can be observed at the intersection area between the Trillium^{TM} and the

substrate AA3003. A larger amount of silicone contained alloy (re-solidified eutectic Al-Si) is above/between the alpha phase aluminum. Erosion can also be observed at the AA3003 surface. Therefore, the image verifies that in the wetting case of the molten clad metal spreading, viscosity and surface tension are not necessarily the only influential factors. Other phenomena such as inter-diffusion, dissolution and corrosion should also be considered (Fu et al., 2016).

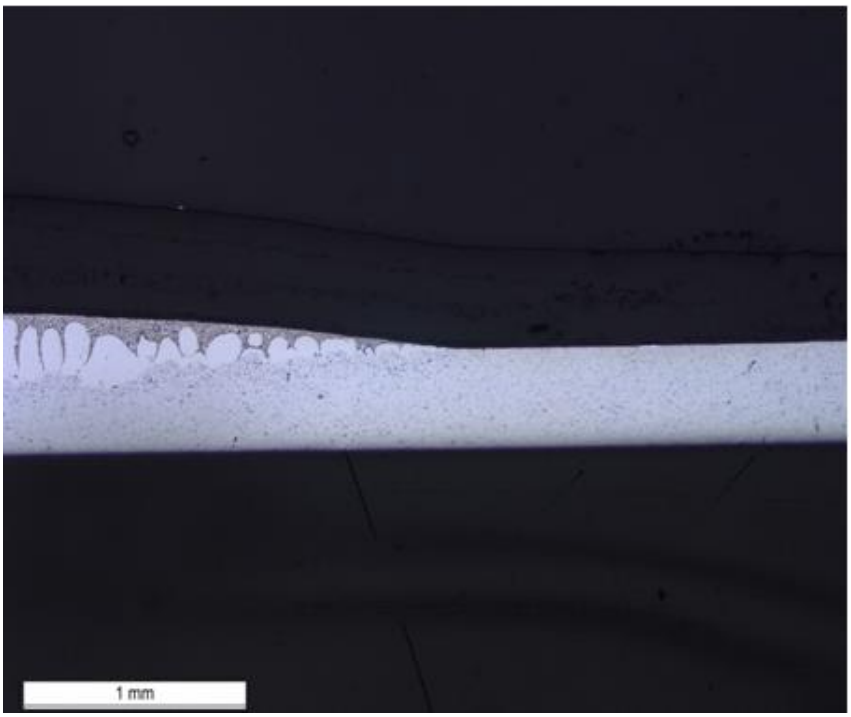

Fig. 5.8 Wetting of the molten clad metal sessile drop triple line on AA3003

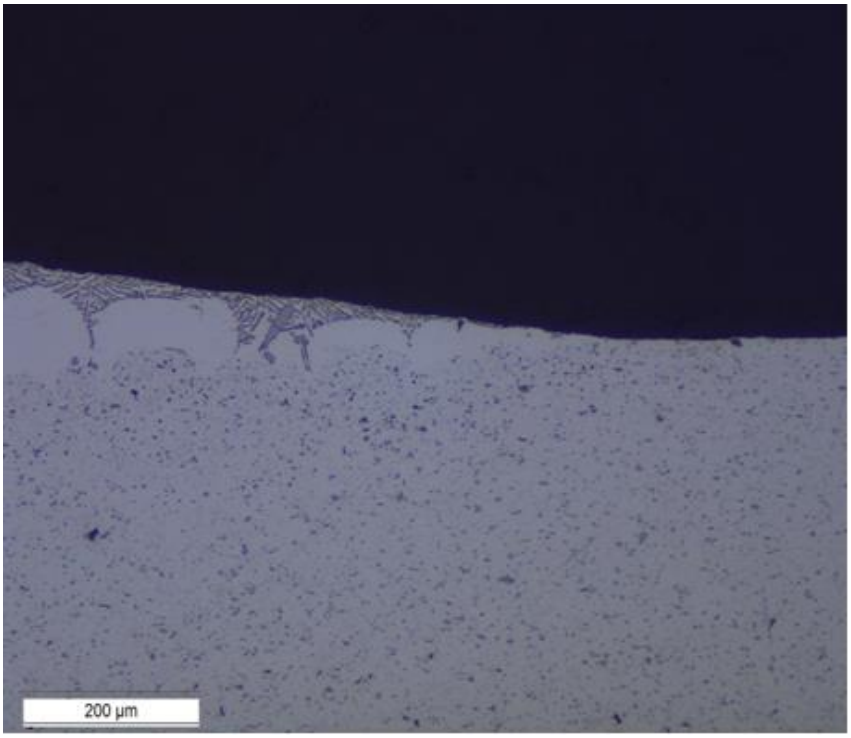

Fig. 5.9 Zoomed-in image of wetting of the molten clad metal sessile drop triple line on AA3003

5.4 Summary

Sessile drop experiment method is adopted to investigate the molten metal spreading features on both wetting and non-wetting substrates. The result verifies the spreading at elevated temperatures for the clad metal Trillium^{TM} in both wetting and non-wetting cases involves more complicated physical phenomena than only viscosity and surface tension driven spreading phenomenon.

The molten clad metal spreadings in both wetting and non-wetting cases are largely isothermal. Key physical properties of the surface tension and contact angle of the new material Trillium^{TM} have been measured for further study on the material and details are presented in the appendix. The surface tension of the Trillium^{TM} has been measured and

compared to multiple references (see Appendix). Based on the theoretical predictions from both Keene (1993) and Egry et al. (2001), the measured surface tension falls in the expected range of aluminum alloy surface tension. The measured surface tension of the new flux-less aluminum alloy serves a critical role in the study.

The triple line region of the sessile drop on the non-wetting and wetting substrates are further analyzed after its re-solidification. In the non-wetting case, the triple line regime presents a more complicated phenomenon. The molten flux, the potassium-fluoro-aluminate contained in the clad metal forms a layer on top of the molten clad metal preventing metal beneath from oxidation. However, flux accumulated at the triple line region forms a ridge. Other phenomena, such as inter-diffusion and erosion can also be observed in the non-wetting spreading of the clad metal. In the wetting case, based on the optical image of the molten metal on AA3003 after re-solidification, the alpha phase aluminum can be seen at the intersection between Trillium^{TM} and AA3003 and the silicone rich eutectic phase separates at the top of the drop. During the spreading process, surface tension and viscosity are no longer the dominating forces in this region, hence more complicated phenomena such as inter-diffusion and erosion and liquid penetration can clearly be seen in those images.

.

CHAPTER 6: WEDGE-TEE CONFIGURATION KINETICS OF THE CAPILLARY FLOW OF MOLTEN CLAD

6.1 Overview

This chapter discusses the experimental study of a specific configuration of mating surfaces (a wedge-tee). The near reactive wetting kinetics at elevated temperatures is considered. The specific configuration is similar to the Wilhelmy plate configuration in the non-reactive wetting studies reported above. In the current configuration, both vertical and horizontal plates are fixed to each other before brazing without any movement. This simulates the joint area formed by the extended surfaces on substrates like the fins in heat exchangers. The sample preparation is introduced in Chapter 4. While Chapter 3 addresses the similar configuration for a non-reactive spreading, serving as the benchmark reference.

Different clad metal forms were investigated in the wedge-tee configuration by changing the clad metal layer thickness. The 2-D configurations of the observed clad metal liquid joint zone formation at elevated temperatures during a time evolution of the molten metal free surface spreading are captured via the Optical Contact Angle Analyzer (OCA) system. It is found that the triple line kinetics features a sequence of multiple spreading phases. These phases of the joint formation are identified and the influential parameters are assessed (Fu et al., 2013). An empirical power law relationship based on the kinetics of the triple line is established for different configurations of the wedge-tee joints.

Different clad metal layer thickness and the substrate surface wetting properties, lead to different equilibrium height of the triple line location. It can be observed, due to a change

in the availability of the molten clad metal at the joint location, that liquid rise greatly depends on an availability of liquid in the pool if the quantity of liquid becomes smaller than some pre-defined quantity related to the total volume of liquid in the joint, formed with an unrestricted flow up to the equilibrium location of the triple line.. The final result of the wedge-tee joint formation kinetics has been compared to the benchmark tests investigated in previous chapters. Numerical analysis also confirms the experimental procedures as well as the experimental results. It can be concluded that in the wedge-tee configuration spreading at elevated temperatures, surface tension and viscosity are not the only controlling factors. Physical phenomena such as inter-diffusion, erosion and liquid metal penetration along the grain boundaries are all taking place at the same time during the process evolution.

6.2 Experimental study of the molten clad metal spreading kinetics in a wedge-tee configuration at elevated temperatures

6.2.1 Molten clad metal kinetics study methodology

The wedge-tee sample preparation and experimental procedure have been introduced in Chapter 4. Three clad metal layer thicknesses have been investigated in the wedge-tee joint configuration. These include, 0.03mm, 0.4mm and 0.8mm thickness of clad metal Trillium^{TM}, see Fig. 6.1. In these configurations, the vertical plate AA3003 has dimensions of 10×10×0.4 mm (in a, b and c configurations), Trillium^{TM} clad metal sheet (horizontal) has dimensions of 10×37×0.32 mm with 0.03 mm thickness Trillium^{TM} clad on the top (configuration a), the AA3003 substrate is 10×37×0.4 mm and the Trillium

filler metal has the dimension of 10×10×0.4 mm (configuration b) or 10×10×0.8 mm (configuration c).

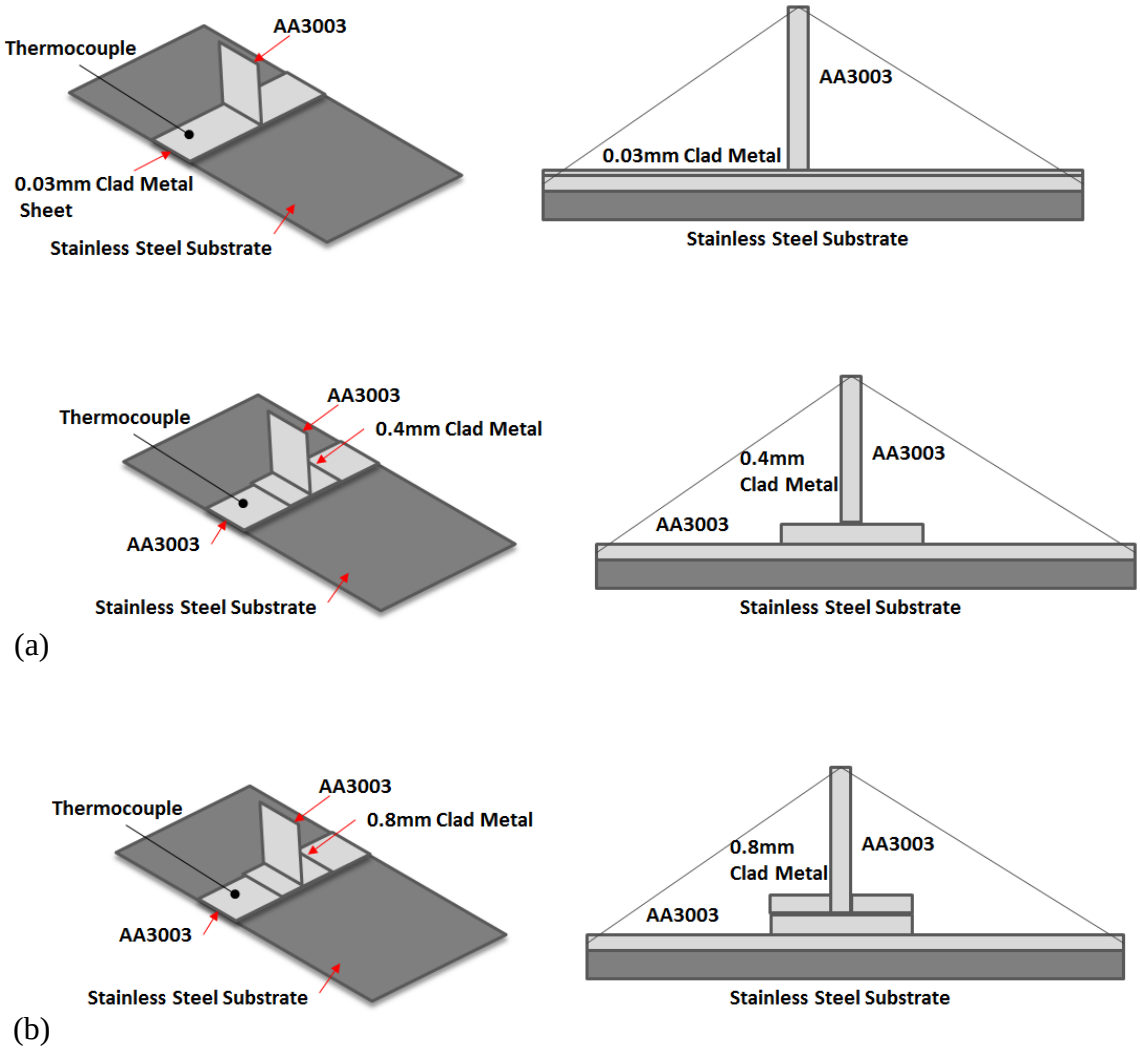

Fig. 6.1 Wedge-tee configuration of Trillium^{TM} clad metal with various thicknesses on wetting substrate of AA3003: (a) 0.03 mm thickness Trillium^{TM} clad; (b) 0.4 mm thickness Trillium^{TM} foil-formed filler; (c) 0.8 mm thickness Trillium^{TM} foil-formed filler

In each experiment with a different clad layer thickness, the sample was placed in the center of the ceramic tube in the heating zone. Before the start of an experiment and after it, the heating zone is purged with ultrahigh purity nitrogen gas. The data collection of temperature starts to record from the beginning of the heating process and the CCD camera starts to record at the temperature of 560℃ and ends at the temperature of 590℃. During the overall time sequence, the wedge-tee joint starts to form during up to 120 seconds included in the video record. The control temperature doesn't have an appreciable effect on the kinetic of the joint formation. The CCD camera records the joint formation process with a frame rate of 5 f/s before the measured sample temperature reaches the melting point of the clad in order to capture the whole period of the T-Joint formation process. After the overall heating time is completed, the heating zone cools down by natural convection, under the atmospheric conditions.

To establish the methodology, the 0.03 mm thickness clad metal configuration has been investigated as a benchmark for the following tests. Detailed experimental methodology is discussed here for the 0.03 mm thickness clad metal configuration.

As shown in Fig. 6.2, the temperature profile of the wedge-tee joint formation process has a ramp-up, dwell and quench phases. The joint formation process can be considered as being executed under the quasi-isothermal state conditions. The relevant temperature span during that process is characterized by temperature changes of 0.17 ℃/s. The formation of the joint finishes within the time domain of 120 seconds.

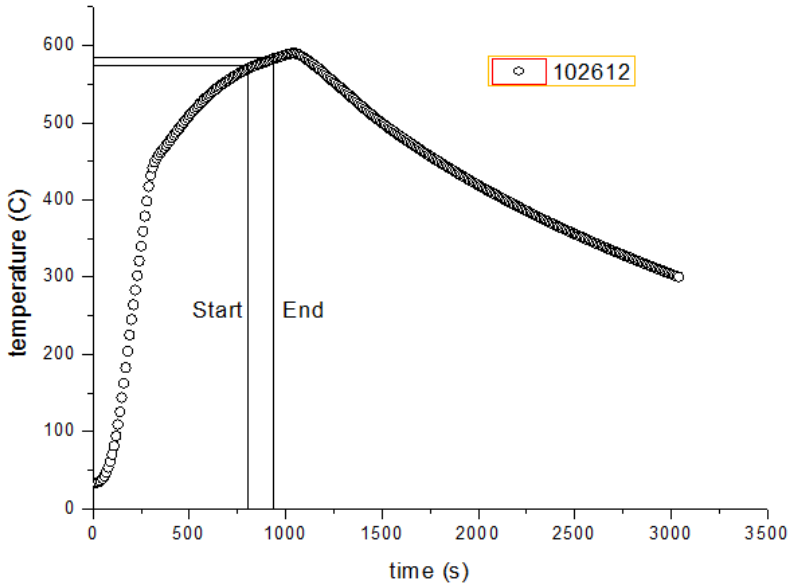

Fig. 6.2 Temperature profiles for joint formation process with recordings of every 10 seconds (experiment 102612)

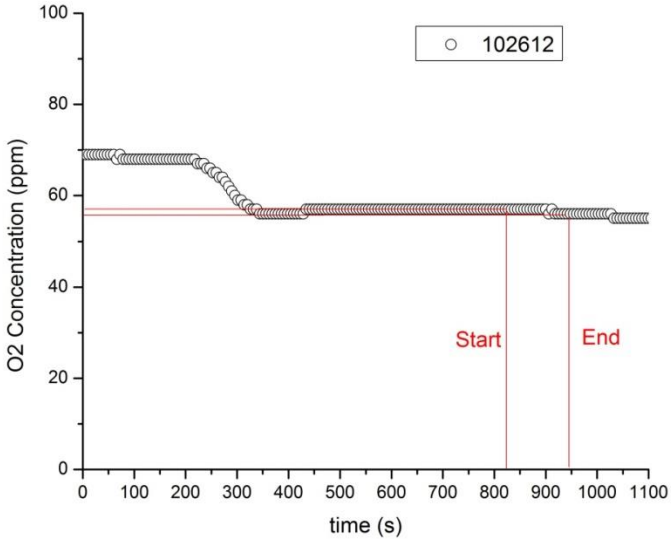

Fig. 6.3 Oxygen level in the joint formation process (experiment 102612)

During the joint formation process, the oxygen level is kept below 100 ppm after more than 2 hours purging with a flow rate of $1.38\times10^{-5} \pm 0.06\times10^{-5}$ kg/s, see Fig. 6.3. Thus the

oxygen concentration should play a negligible influence on the molten clad metal spreading. As introduced in Chapter 4, both horizontal and vertical directions of the joint extend are measured on both left and right sides for the comparison, but rigorously speaking only the vertical location can be interpreted as a triple line location..

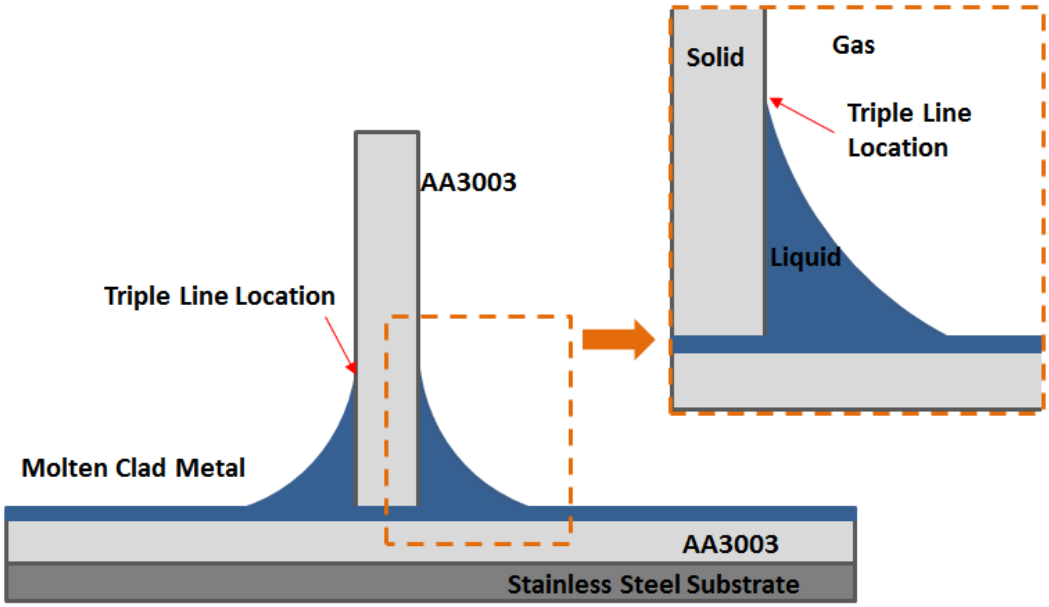

Fig. 6.4 Schematic diagram of triple line location at wedge-tee joint area with molten clad metal

The symmetric configuration of the wedge-tee joint configuration is shown in Fig. 6.4. Both left and right sides in the vertical direction at the top of the meniscus are representing the triple line location. Thus either right or left could be selected for the triple line location kinetics analysis. The horizontal end location of the meniscus, however, features the meeting of the locus of points of the liquid and gas (no solid substrate), thus it is not triple line location. After being extracted from the video, an example sequence of images of the triple line location progress is shown in Fig. 6.5.

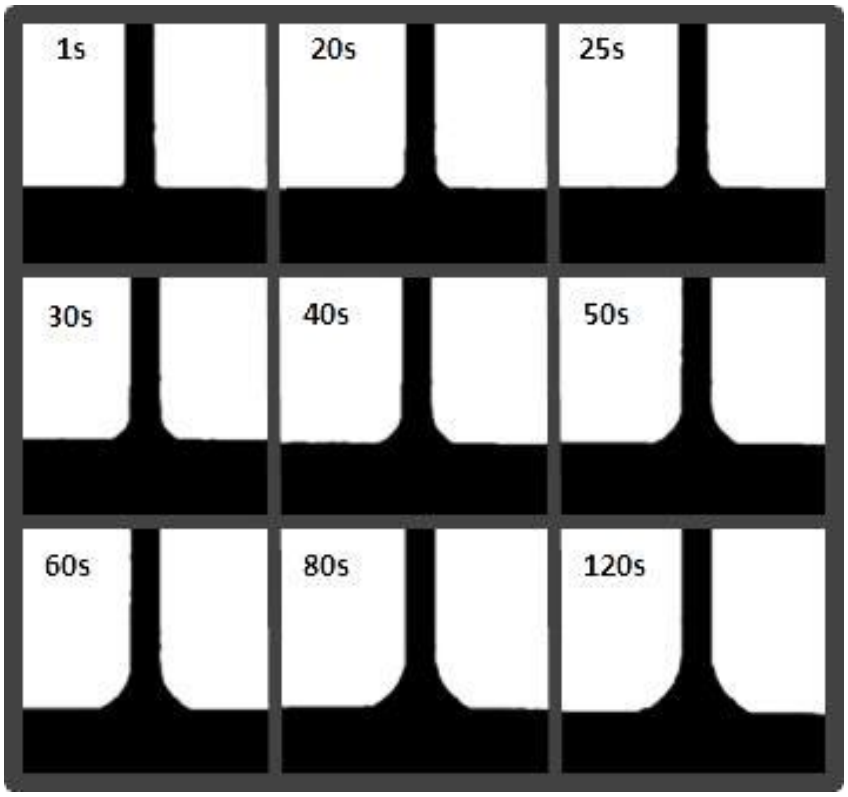

Fig. 6.5 A sequence of images decomposed from a recorded movie indicating the evolution of the joint meniscus formation as a function of time (0.03mm thickness Trillium^{TM}) (Test 091212)

The individual frames were extracted from the recorded video at the frequency of 1 image per second, starting right before the onset of the formation of the joint (hence, a 120 seconds long video has 120 images). The complete joint formation would end seconds before an expiration of 120 seconds (see Fig. 6.5). Both vertical and horizontal directions menisci kinetics were measured by extracting data from the images. The normalized data (each location data value is scaled with the maximum distance of the triple line established upon reaching the steady state) are plotted in Fig. 6.6 (a). As shown in Fig. 6.6 (a), it can be observed that the vertical direction triple line location is slightly smaller than the horizontal line. The reason for this discrepancy may be attributed to the

impact of gravity and different physical parameters, regardless of a small Bond number of Bo = 0.015. Note that the conditions of liquid phase "withdraw" on horizontal and spreading on vertical surfaces differ due to the fact that horizontal surface represents the brazing sheet and the vertical surface a non-clad substrate. Hence liquid metal produced at the onset of melting may impact the location of the horizontal joint extend in a different way than the triple line climbing the vertical surface (including reaction and gravity) (Fu et al., 2013). Consequently, only vertical direction of the spreading will be further studied. An average of 7 times repeated test, normalized by the spreading distances in the vertical direction for the 0.03 mm thickness Trillium^{TM}, (with the corresponding error bars), are shown in Fig.6.6 (b).

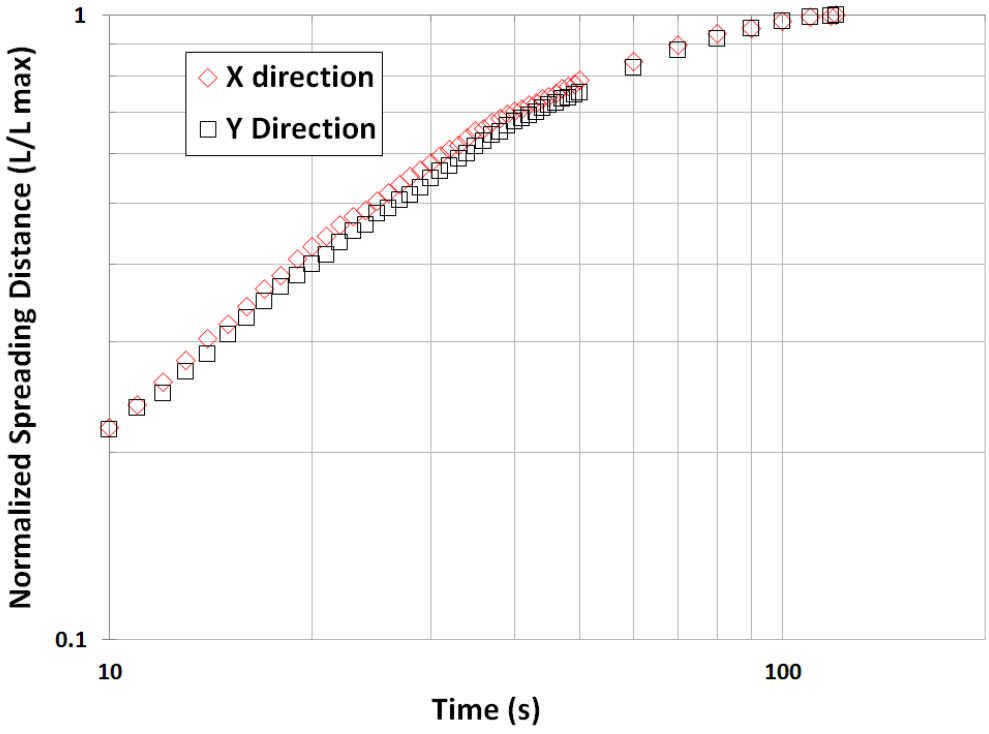

(a)

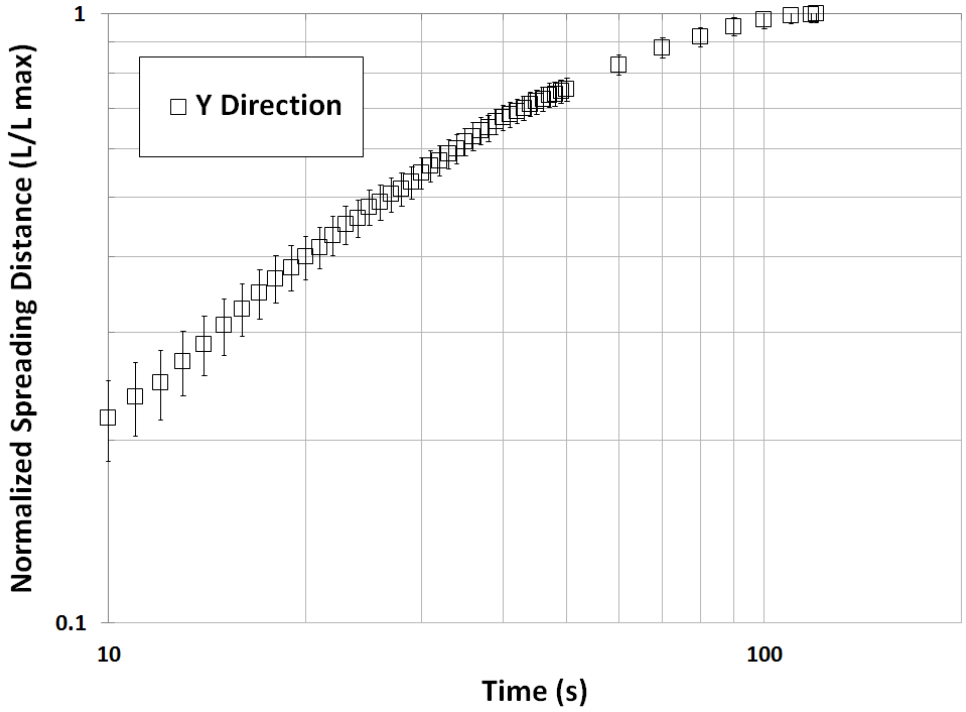

(b)

Fig. 6.6 (a) Normalized spreading distance in both horizontal (X) and vertical (Y) directions and (b) normalized spreading distance in y direction with standard error bars, (an average of 7 times repeated experiment of the 0.03 mm thickness Trillium^{TM} clad metal)

To further study the triple line location kinetics, the averaged kinetics data of the triple line location as a function of time is plotted in Fig. 6.7. The log-log plot of Fig. 6.7 shows that there are at least two regimes, periods/phases during the joint formation evolution of the triple line kinetics. In the first phase, from the time instant of 2 seconds to the time instant of 30 seconds, the slope was fitted well with 1/n= 1.07. In the second phase, from

the time instant of 30 to 100 seconds, the slope was fitted with 1/n=0.51. Therefore, the ~0.5 power law relationship matches in the second region the experimental data.

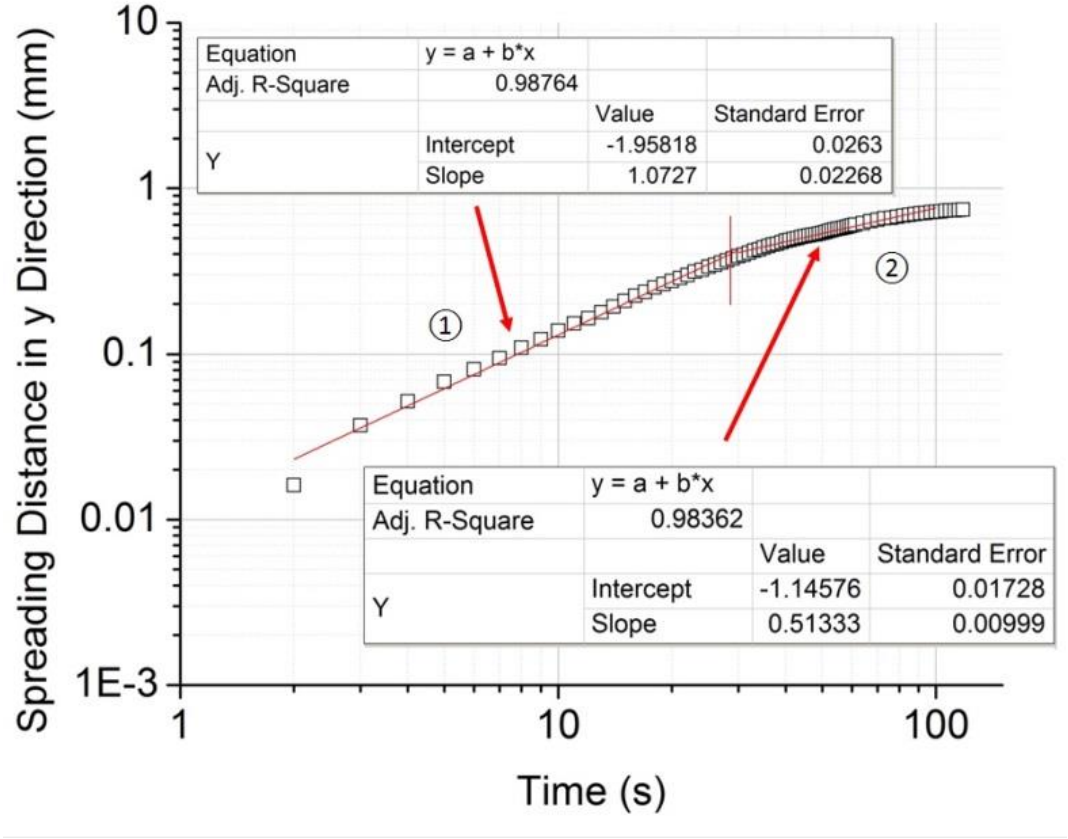

Fig. 6.7 Triple line location kinetics plot in two stages

It can be hypothesized that in the second region the trade-off between surface tension and the viscosity controls the kinetics of the molten liquid metal spreading even when secondary reaction/interface phenomena (see Fig. 6.8) are happening at the same time. Figure 6.8 testifies that the substrate interactions are mild and the reaction would be better characterized as near-reactive flow. Moreover, we note that the front of formed liquid spreads through the randomly formed channels between micro asperities over the real (rough) surface, i.e., the enhanced topographical alterations formed during melting in

situ. An optical cross section image of the joint formation after re-solidification is shown in Fig. 6.8. Silicon diffusion into the horizontal substrate and depletion of the liquid Si content at the interface contributes to alpha phase formation in the Al-Si alloy at the horizontal substrate interface (Gao et al., 2002). The mild erosion can be observed in the figure to prove a presence of more complicated interface phenomena other than surface tension and viscosity are also controlling the spreading kinetics of the molten clad metal. These interface phenomena are much more pronounced on the vertical surface, significantly corroded away from the triple line in the zone of the bulk liquid alloy during joint formation. So, this interaction is attributed to the period of time following the triple line movement up to the near equilibrium state. This hypothesis, however, requires a thorough study which is beyond current scope of the study.

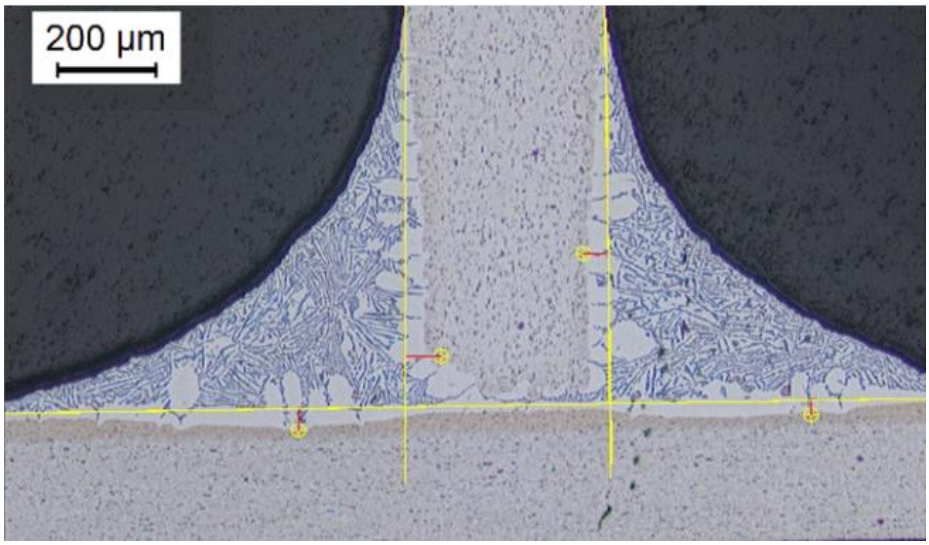

Fig. 6.8 Joint formation cross-section after re-solidification image

6.2.2 Molten clad metal kinetics under deteriorated background atmosphere

As mentioned earlier, the above experiments are done with the background atmosphere having oxygen concentration level below 100 ppm. An additional series of oxygen

concentration level experiments are also studied for establishing the impact that such change would have on the kinetics of the joint formation. Two higher oxygen concentration levels, namely 200 ppm and 500 ppm, are analyzed using the same methodology introduced in the previous section. Both left and right sides of the triple line location on the vertical surface are measured at 1 data point per second. Fig. 6.9 and 6.10 offer data points every 3 seconds (both, triple line actual height and the normalized triple line height). The oxygen concentrations were 70 ppm, 200 ppm and 500 ppm. Total of 11 experiments were done with the 70 ppm oxygen concentration level and the averaged data are plotted with standard deviation bars. For higher oxygen concentrations, 3 experiments were done respectively with averaged data and standard deviation plotted in the figures. For better comparison, the triple line locations are also normalized-dividing the triple line location by its maximum heights.

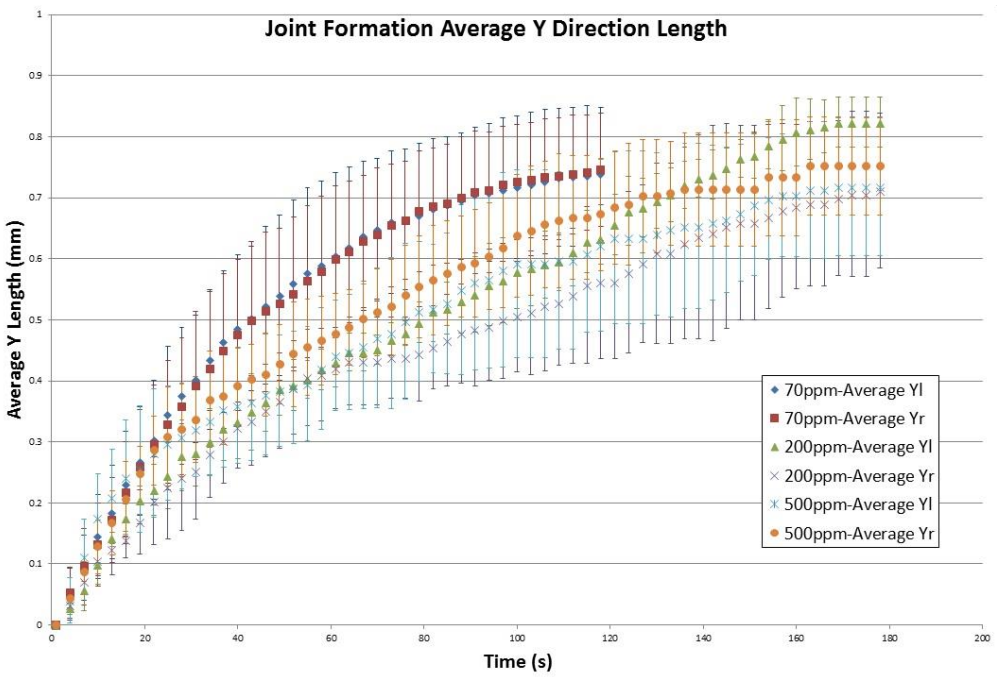

Fig. 6.9 Triple line kinetics of the joint formation with different oxygen concentration levels

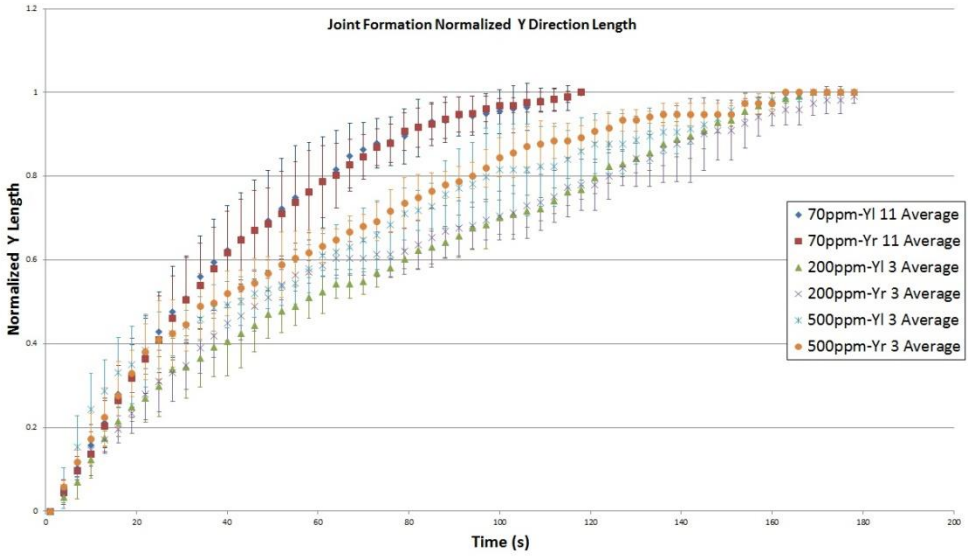

Fig. 6.10 Normalized triple line kinetics of the joint formation with different oxygen concentration levels

Based on the results, it is noted that with higher oxygen content in the controlled brazing atmosphere, the time consumed for the finishing joint formation is longer. However the final height doesn't have the dramatic difference compared to the 70 ppm oxygen level. It can be seen that in these three oxygen level experiments, the initial kinetics behaviors are close to each other. The deviation of the kinetics starts after initial 15 seconds with the lowest triple line location in the 500 ppm oxygen level. To form the same joint area, 70 ppm oxygen level is clearly the optimal atmosphere condition for the triple line kinetics. In terms of the final triple line location height, the difference between 200 ppm and 500 ppm is not dramatic with the standard deviation bars. No clear distinction between the 200 and 500 ppm's can be identified. This may be an artifact of the relatively small number of tests performed. The clear distinction between these two deteriorated cases vs. 70 ppm is, however, obvious.

6.2.3 Molten clad metal kinetics with different clad layer thicknesses

As mentioned earlier, the 0.03 mm thickness clad metal sample configuration is the benchmark for further investigation on the clad metal thickness impact. Two more clad metal thicknesses (0.4 mm and 0.8 mm) are also considered, see Fig. 6.1 (b) and (c). A sample of 0.4 mm thickness Trillium^{TM} clad configuration is shown in Fig. 6.11.

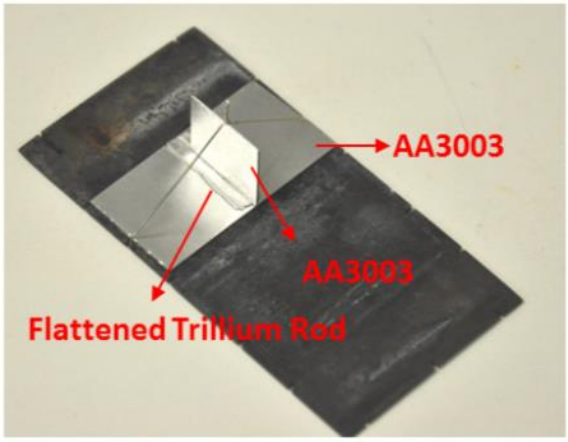

Fig. 6.11 0.4 mm thickness Trillium™ kinetics study sample configuration

In the 0.4 mm thickness clad metal configuration, a similar heating cycle is implemented in the three independent tests, with heating rate of 0.17 °C/s from the melting point to the end of joint formation of 120 seconds. The results are plotted in Fig. 6.12 with the dynamic contact angle.

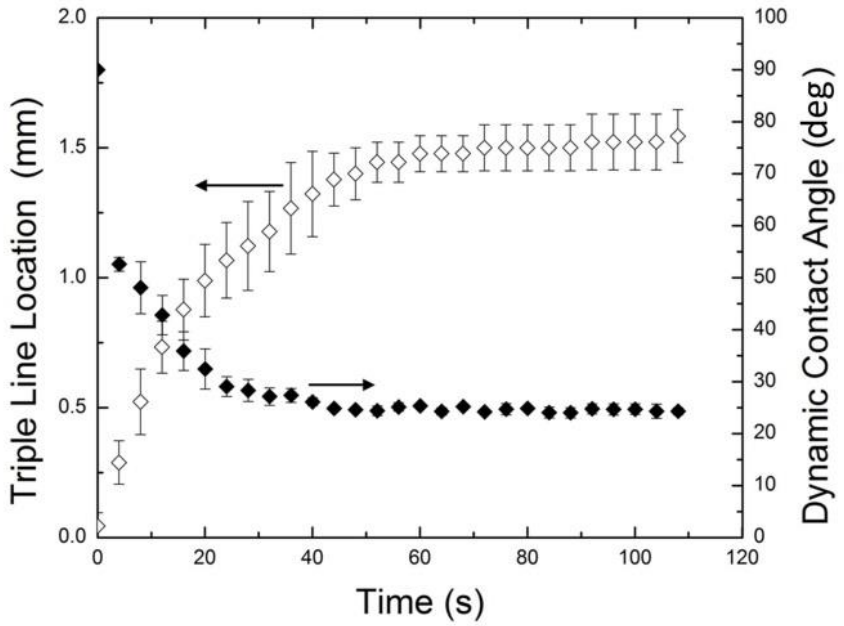

Fig. 6.12 Linear scale representation of 0.4mm thickness Trillium™ clad metal kinetics with triple line location and dynamic contact angle (Fu et al., 2016)

The result of the 0.4 mm thickness Trillium™ clad metal kinetics is also compared with the 0.03 mm thickness Trillium™ clad metal as well as the non-reactive systems of water and silicone oil, see Fig. 6.13. A logarithmic scale plot of the triple line kinetics with standard deviation error bars and power law correlations are shown.

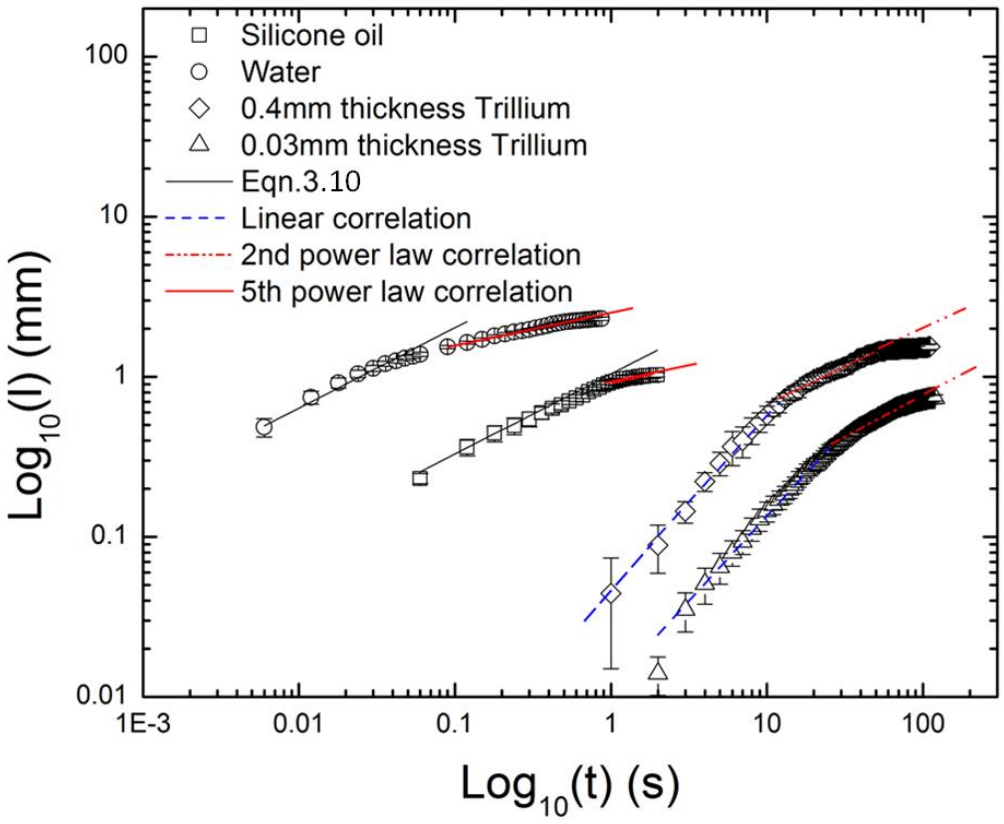

Fig. 6.13 Log scale of (i) silicone oil, (ii) water, (iii) 0.03 mm thickness Trillium™ and (iv) 0.4 mm thickness Trillium™ kinetics comparison with Washburn's equation, Eq. 3.10 i.e., the power law correlations

It can be seen from Fig. 6.13 that in the silicone oil and water systems, Eq. 3.10 fit ($t \sim l^2$) is featured by the first capillary-viscous stage (Liu et al., 2012) of the kinetics. The 5th power law relationship ($t \sim l^5$) of the triple line location and time can be observed in the subsequent capillary-viscous-asymptotic stage (Liu et al., 2012). For the weak reactive

wetting case of Trillium^{TM} clad metal, a linear power law correlation ($t \sim l$) can be observed in experiments of both 0.03 mm thickness and 0.4 mm thickness liquid clad metal. A 2nd power law correlation can be fitted in the second stage (Fu et al., 2013). Equation 3.10 (with only viscosity and surface tension as dominating factors) would not be adequate to explain the two-stage phenomenon. This is because additional physical phenomena (such as chemical reaction, ridging, inter-diffusion and de-oxidation of the liquid Trillium as well as dissolution of Trillium^{TM} on aluminum substrate) also play significant roles in the process (Saiz et al., 1998; Saiz et al., 2005; Saiz et al., 2007; Benhassine et al., 2009; Champion et al., 1969; Drevet et al., 2012), especially at the triple line location.

To further study the triple line kinetics impact factors, 0.8 mm thickness clad metal configuration (Fig. 6.1) is used as well, with a higher heating rate of 0.22 °C/s (from the melting point to the end of joint formation of 120 seconds). Two independent tests are done, and the averaged values of the triple line location with standard deviation error bars are shown in the linear scale in Fig. 6.14 and the log scale in Fig. 6.15.

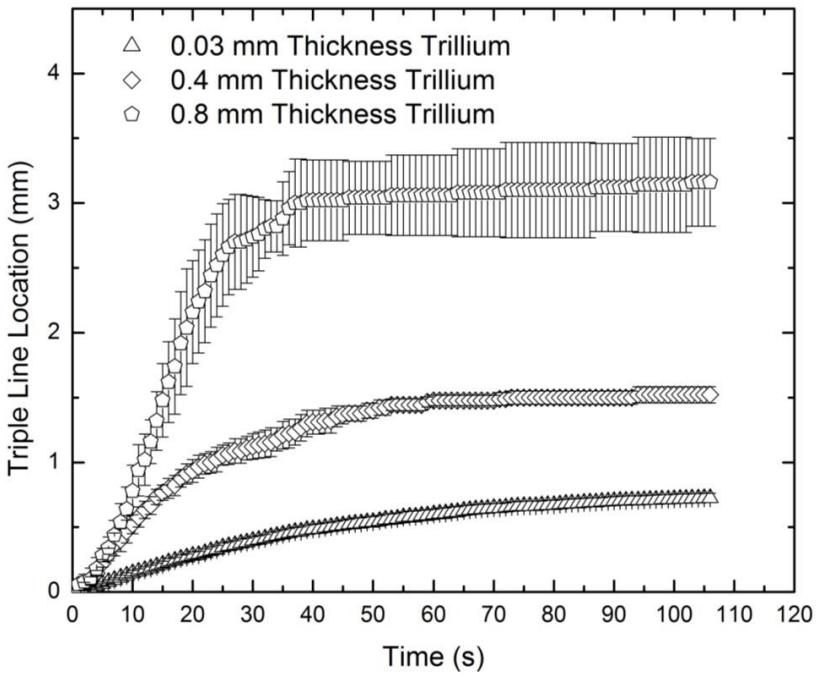

Fig. 6.14 Linear scale of 0.03 mm thickness Trillium^{TM}, 0.4 mm thickness Trillium^{TM} and 0.8 mm thickness Trillium^{TM} kinetics comparison

It can be seen from both Fig. 6.14 and Fig. 6.15 that the final triple line height in the 0.8 mm clad metal thickness is higher than those of thinner thickness clad metal. This can be explained by the available amount of molten clad metal at the joint area during the brazing process. The kinetics behavior can be observed in the log scale figure in Fig. 6.15. In the thinner thicknesses, both 0.03 mm and 0.4 mm thicknesses show the similar trend of a linear (in the log scale) progress initially with a slower trend in the second stage. However, the 0.8 mm thickness clad metal shows a higher slope initially and a sudden change in the end of the slope. The last stage of the 0.8 mm thickness is relatively flat as opposed to the previous two cases.

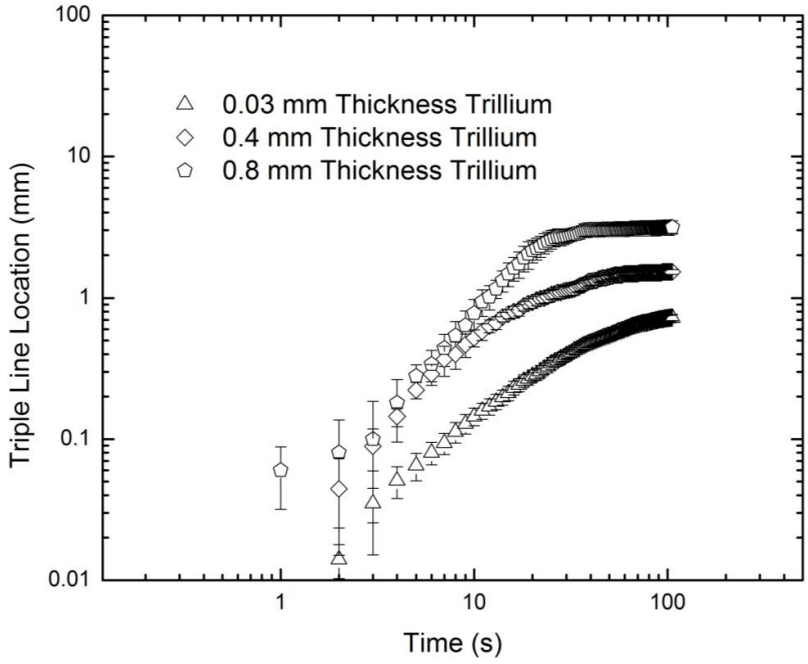

Fig. 6.15 Log scale of 0.03 mm thickness Trillium™, 0.4 mm thickness Trillium™ and 0.8 mm thickness Trillium™ kinetics comparison

6.2.4 Molten clad metal kinetics on non-wetting surface

In order to further investigate the maximum height of the triple line location, a case is considered with non-wetting substrate (horizontal mating surface made of alumina) with a vertical mating surface prone to wetting (aluminum). Due to the non-wettability of the horizontal substrate, it is hypothesized that the molten clad metal would be spreading only on the vertical plate forming gravity-surface tension controlled liquid envelope. The experiment is done following the same procedure and process methodology as the previous experiments with 0.22 °C/s from the melting point to the end of joint formation of 120 seconds. The configuration is shown in Fig. 6.16.

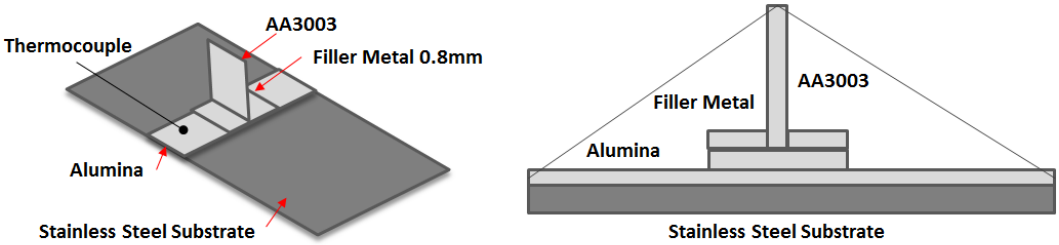

Fig. 6.16 Trillium^{TM} filler metal on non-wetting alumina horizontal surface configuration with thicker filler metal of 0.8mm

Fig. 6.17 Molten clad metal spreading on vertical AA3003 plate with non-wetting horizontal surface (Experiment 05052015)

The sample configuration is shown in Fig. 6.16. A final configuration of the equilibrium state at 120 second from the beginning of the melting is shown in Fig. 6.17. As was predicted, a volume of 0.8 mm thickness clad metal melts and the molten clad metal spreads onto the vertical AA3003 plate with no obvious molten clad metal left on the horizontal substrate. The kinetics of this process is measured from the extracted

individual frames from the video taken during spreading. A total of three independent experiments were executed. The kinetics this spreading process is plotted in Fig. 6.18.

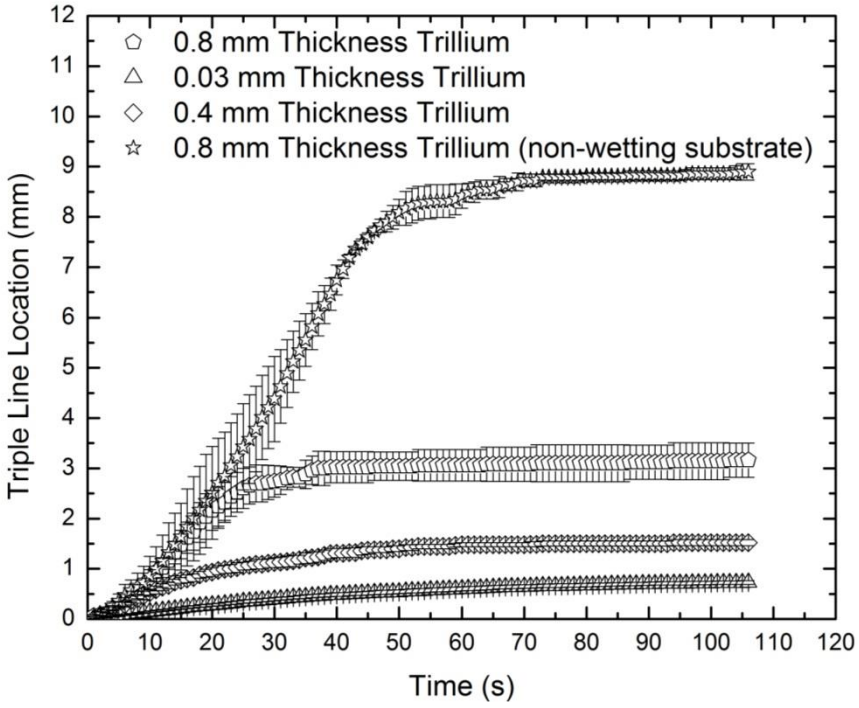

Fig. 6.18 Kinetics of 0.03 mm thickness Trillium™, 0.4 mm thickness Trillium™, 0.8 mm thickness Trillium™, all on wetting horizontal surface, and 0.8 mm thickness Trillium™ on non-wetting horizontal but wetting vertical

It can be seen that given enough available molten clad metal at the horizontal substrate, the triple line location height can reach up to approximately 9 mm. A kinetics trend comparison between these four experiments is also shown in a log scale in Fig. 6.19.

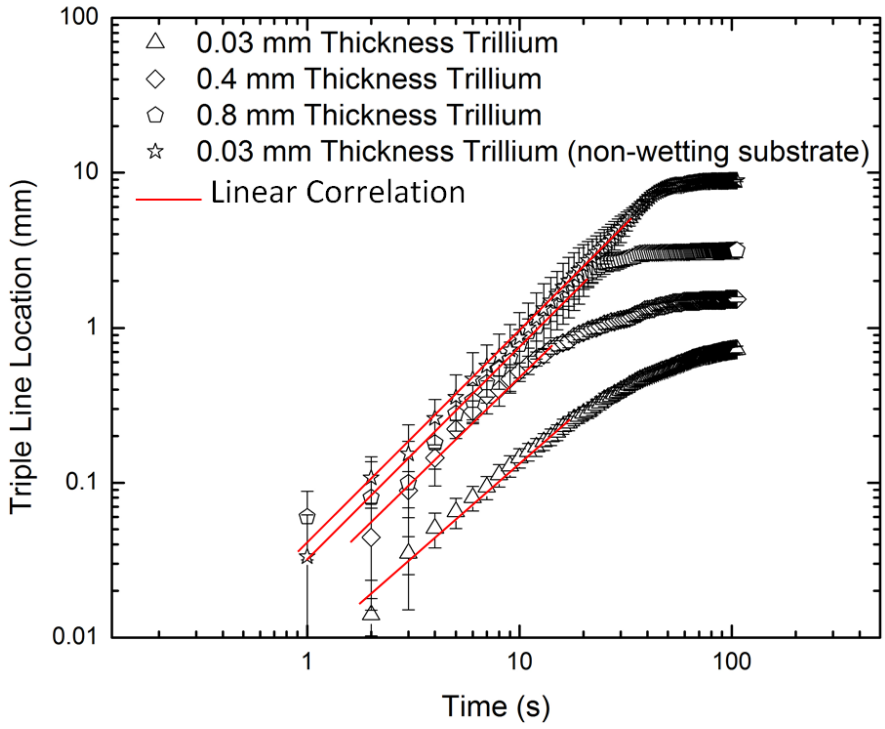

Fig. 6.19 Kinetics of 0.03 mm thickness Trillium^{TM}, 0.4 mm thickness Trillium^{TM}, 0.8 mm thickness Trillium^{TM} and 0.8 mm thickness Trillium^{TM} on non-wetting horizontal substrate but wetting vertical substrate

It can be seen from the log scale, Fig. 6.19 that in these different thicknesses experiments, the initial kinetics is similar, regardless of its horizontal substrate surface properties. A quasi linear correlation (in a log-log coordinate system) can be fitted in all those experiments. The non-wetting horizontal substrate surface experiments feature the longest spreading regime. The shortest triple line height is for the 0.03 mm thickness clad, as expected. The triple line location height is largely controlled by the available clad metal amount, and the initial kinetics of the triple line is not impacted by the clad metal volume. The post linear stages (log-log) in these experiments are not all the same. It can

be interpreted that after the linear kinetics stage (log-log), the molten clad metal quantity is not sufficient to support the linear (log-log) spreading process.

6.3 Phase-field model analysis of the molten clad metal kinetics

The results of this section have been published by Fu et al., 2016 and Dehsara et al., 2016. A brief introduction of the phase field model is presented in Appendix E. The diffuse interface (phase-field) model is used to analyze the triple line movement. The triple line movement is described in terms of a local surface diffusion of fluid. In the computational model, a 2-D wedge-tee joint configuration was considered. The phase field model parameters are related to the physical parameters (density, viscosity interface energies, kinetic barrier for surface diffusion), and the computational parameters. The non-reactive benchmark experiments of silicone oil and water spreading on glass provided the sufficient support before the model is implemented on the molten clad metal spreading. Excellent agreement is achieved with both benchmark experiments and 0.4 mm thickness clad metal experiments. The experimental data and simulation data are plotted against each other in Fig. 6.20. It is assumed that the surface roughness is also an important factor in the wetting process, but the study is beyond the scope of the current research.

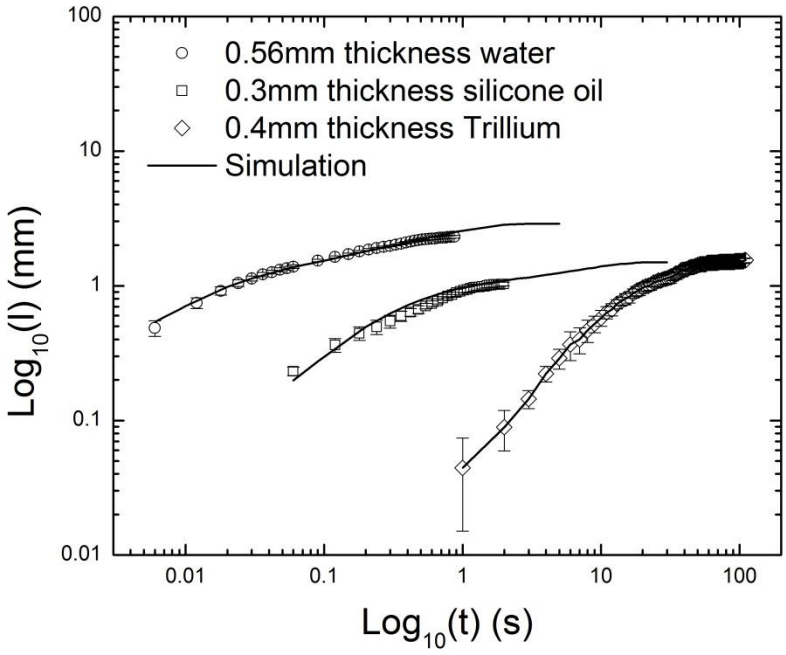

Fig. 6.20 The comparison between experimental data and phase field modeling

6.4 Summary

In this chapter, the kinetics of molten clad metal at elevated temperatures spreading at the wedge-tee joint area is studied comparatively both experimentally and numerically. A thinner clad metal sample configuration is firstly established for the initial experiment methodology. The result shows a slower triple line kinetics process compared to previous non-reactive spreading process. Following the benchmark methodology, two additional clad metal thicknesses are designed for experiments. The result shows the triple line location height is impacted by the available amount of the molten clad metal at elevated temperatures. Another non-wetting substrate is used as the ideal maximum amount molten clad metal provided at the joint area. The result further confirms the triple line location height is impacted by the molten clad metal volume. The comparative study also shows the initial stages of these different configurations obey a similar quasi-linear

kinetics process regardless of its horizontal surface properties and its clad metal volumes. With larger amount of the molten clad metal, the quasi-linear kinetics process in the log-log scale lasts longer.

In the numerical analysis based on the result from Washington State University, a phase field model of wetting based on modified Navier-Stokes equations, incompressibility condition and the 4^{th} order Cahn-Hilliard diffusion equation for the conserved phase field is developed combining multiphase flow and contact line dynamics of a diffusive boundary interface. The model provides a solid background for an accurate theoretical description of the wetting phenomena for both non-reactive and reactive wetting at elevated temperatures. The numerical model results are compared with the non-reactive benchmark experiment results, and the results have an excellent agreement. Due to the generality and thermodynamics nature of the model, this model can be extended to complex problems with chemical reactions and diffusion of components, such as the molten clad metal kinetics process. The numerical model successfully predicted the evolution of the meniscus and triple line kinetics process for both non-reactive and reactive systems.

CHAPTER 7: CONCLUSION AND FUTURE WORK

This chapter summarizes this dissertation. Contributions to the knowledge about kinetics of spreading phenomena are addressed first. Suggestions regarding future study are discussed next.

7.1 Main conclusions from the current study

The kinetics of non-reactive and reactive spreading for both ambient temperature systems and the elevated temperature systems have been studied experimentally and compared to numerically obtained data from a simultaneously performed collaborative study constituting jointly a work within the NSF sponsored research under Grant # 1234581 and # 1235759. The kinetics of molten clad metal spreading is defined as the movement of the triple line of the advancing front of the liquid metal driven by surface tension into the joint area of two melting metal surfaces. This phenomenon is important for Controlled Atmosphere Brazing (CAB) among multiple other technological applications. Based on the experiment findings, the spreading kinetics at the wedge-tee joint area can be well predicted via analytical empirical and semi-empirical correlations. The numerical solutions for both non-reactive and reactive spreading has been obtained following a development of the phase-field theory of the liquid front advances (that segment of work is beyond the scope of the dissertation effort), except as data base for comparison.

The non-reactive spreading systems involved water on glass and silicone oil on glass. The empirical data from these experiments were used to verify the analytical and the semi-empirical solutions, as well as later numerical analysis.

The spreading kinetics at elevated temperatures features an Al-Si alloy system combined with addition of $K_xF_yAl_z$ system on Al substrate.

The result of the non-reactive systems' spreading has confirmed that the kinetics of the triple line is controlled by surface tension and viscous force. An empirical constant based on the Washburn's law is established for both water and silicone oil systems. The equilibrium height of the triple line location and contact angle relation from the experiment data were both well predicted by the analytical solution derived from Young's and Laplace equation. Seebergh and Jiang's empirical correlation well fitted in the experimental data of spreading kinetics of capillary number and dynamic contact angle in the silicone oil/glass systems. A modified Seebergh empirical correlation is also developed to predict the capillary number and dynamic contact angle relationship from the benchmark experiment in water/glass systems. The later capillary-viscous-asymptotic stage is also discovered in both water/glass and silicone oil/glass systems. The later stage obeys a 5^{th} power law relationship consistently.

The sessile drop experiments for the molten clad metal spreading at elevated temperatures have been designed to investigate the molten clad metal properties. The system used is a new brazing clad metal material Trillium^{TM}, a patented Al-Si alloy with embedded salt content so a self-fluxing process occurs during CAB brazing. The sessile drop experiments were conducted with the Optical Contact angle Analyzer (OCA) facility. The surface tension of the molten clad metal system has been experimentally determined. The experimental data on kinetics of the molten metal triple line movement were compared with kinetics trends from various literature sources. The re-solidification images and SEM/EDS results indicating the structures at the interface zone within the triple line region prove that the molten clad metal spreading at elevated temperatures involves more complicated physical phenomena, such as inter-diffusion and dissolution.

Still, the interaction may be considered as mild if the dwell at the peak temperature is brief.

Various clad metal thicknesses (before melting – hence offering various liquid pool quantities during spreading) were considered in the experiments to determine the joint formation size. The linear log-log kinetics correlation is identified in the experiment data, and a 2nd power law correlation is observed in the later stage. A non-wetting alumina horizontal substrate and vertical AA3003 plate system was studied as well to establish kinetics of the triple line on the vertical Al3003 surface. The results re-emphases that clad liquid metal initial volume impacts the final triple line location height. The initial log-log kinetics relationship is established, but the larger the clad metal volume, the longer the linear log-log trend lasts. The later stages of the kinetics are not all the same due to complex controlling factors.

Supported by the experimental results from both non-reactive and reactive systems, a phase field model was established in a simultaneous study, beyond the scope of the Thesis work (that one is executed at the Washington State University). Based on Lowengrub et al. (1998) analysis and the initial model from Jacqmin (2000), the governing equations of the incompressible model were offered. These consist of the modified Navier-Stokes equations, the incompressibility condition and the 4^{th} order Cahn-Hilliard diffusion equation. The numerical model is simulated by using Comsol MultiPhysics 3.5a/4.3 software. The simulated meniscus well verifies the experimental meniscus in both non-reactive and reactive systems. The numerical results have excellent agreement with the triple line kinetics in water/glass, silicone/glass and 0.4 mm molten clad metal on AA3003. Besides the surface tension and viscous force dominating the

non-reactive systems, it is assumed that diffusion controlled concentration changes do not significantly affect the fluid viscosity in the reactive systems at elevated temperatures, and that their effect on the TPL mobility can be phenomenologically included in the model through the triple line mobility parameter without explicitly modeling the changes in diffusion and concentration of molten clad metal.

7.2 Future work

Further study is necessary to better understand the physical/chemical nature of the spreading process of liquid metal over metal substrate.

In the non-reactive ambient temperature benchmark study, two liquid systems are investigated to support the surface tension and viscous force driven theory and the numerical model verified the experimental results. More liquid species spreading would be helpful to identify the later stages of the spreading kinetics phenomena. The initial stage of the non-reactive spreading can be identified as the Washburn type spreading, but the process ending point to the later stage is still ambiguous. An empirical relationship of the transition between Washburn type spreading and the capillary-viscous-asymptotic stage should be established either from experimental analysis or numerical analysis.

The clad metal sessile drop kinetics needs to be studied further in the current experimental setup in both non-wetting and wetting substrates. It is noticed that in the current experiments the spreading process is controlled by different physical phenomena in these two types of substrates. Dissolution, inter-diffusion and are dominant in the case of the wetting Al substrate.

The exact triple line location height at equilibrium state needs to be confirmed with liquid molten clad metal on the wetting substrate not limited.

Surface topography has been an important factor impacting the spreading kinetics. In current study, smooth surfaces are considered in both non-reactive and reactive spreading kinetics study. Surface roughness should be identified as another variable in the future study.

Temperature heating rate impact on the kinetics of the spreading at elevated temperatures has been noticed in several experiments that are not reported here. Smaller heating rate corresponds to the slower triple line growth with smaller value in the spreading kinetics correlation slope. The correlation between the heating rate and the diffusion of the mobile elements in the aluminum alloy should be further identified. To what extent the heating rate is impacting the kinetics of spreading should be investigated.

APPENDICES

Appendix A

Experiment data error analysis (non-reactive case, Water and Silicon oil)

The triple line kinetics data shows an expected dispersion of data to be described by the certain range of incurred measurement variations. It is important to establish whether the dispersion is a consequence of experimental errors inherent to data collection, or that there is another source of deviation caused by an influential parameter not identified so far. Hence, the deviation could be a result of (i) a measurement error or (ii) a presence of the variations in experimental conditions. As an example, an experimental run 012814a was selected for the example of the measurement error analysis. Both right and left side of the vertical surface data for the triple line locations were measured 3 times and plotted in Fig. A1 and Fig. A2 for averaged measured plot.

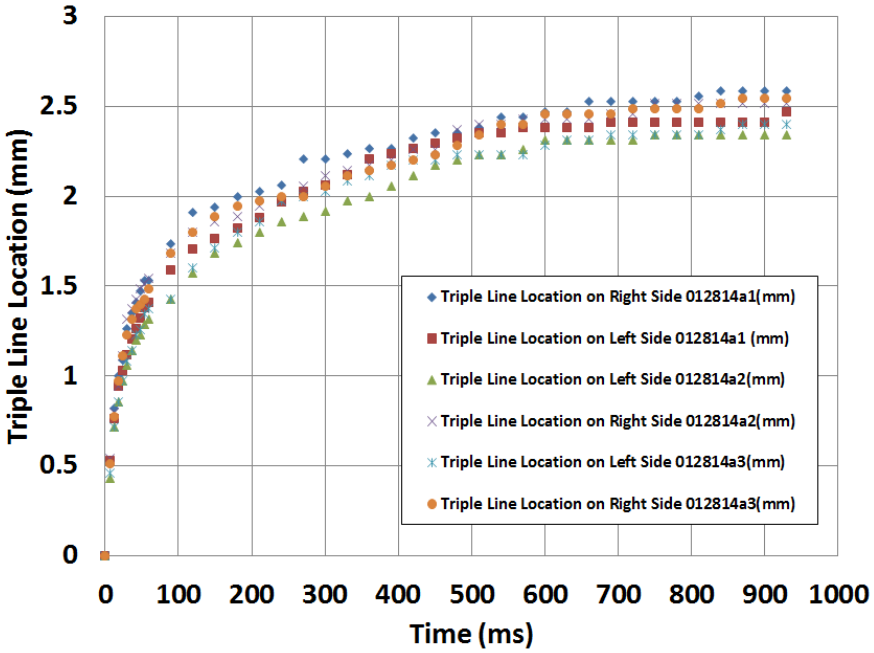

Fig. A1 Average measurement of triple line location of experiment 012814a

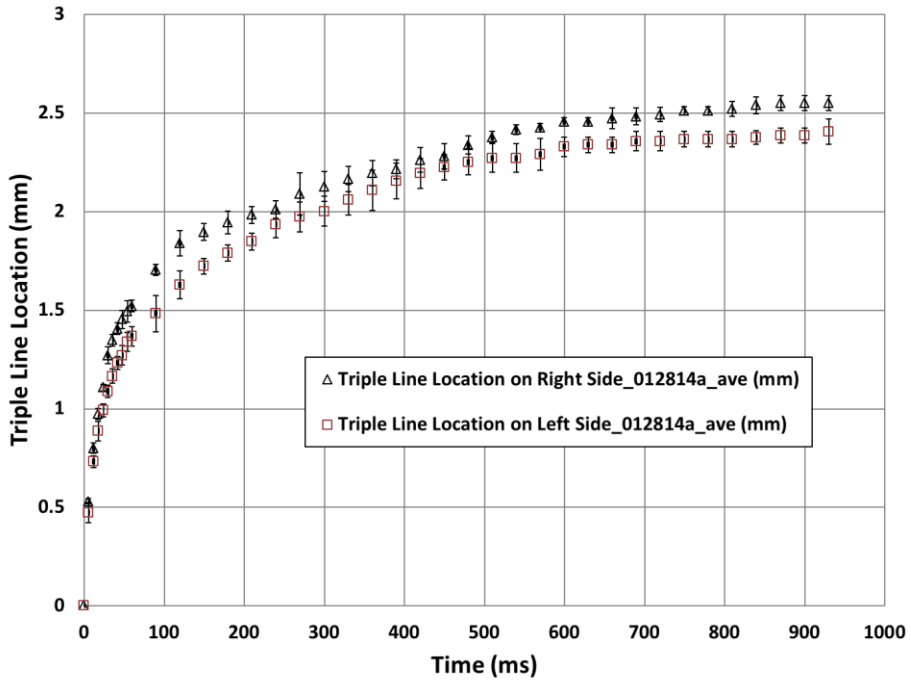

Fig. A2 Average measurement of triple line location of experiment 012814a with error bars

From Fig. A1 one may see that for the experiment considered, the measurement deviations of 0.064mm on the left side and 0.037mm on the right side are established (on average). Therefore, it can be seen that the measurement error appears not to be a main contribution to the deviation (i.e., the dissipation expressed by the error bars is smaller than the dispersion of data for different experiments data). The triple line location deviation identified for two sides appears to play a more important role in the triple location dispersion. The dispersion of data on both sides of the triple line location is shown in Fig.A1 for a single test with different measurements.

Now, we may consider how to estimate an impact of another factor contributing to the triple line location deviation: the experimental conditions including in particular the state

of the substrate's surface. Although, the experiments were done at the same temperature (22±2°C), humidity in the ambient (relative humidity less than 60%) and the surface conditions (manufacturer pre-cleaned – each experiment conducted with a new virgin glass substrate), the final (equilibrium) triple line location has a maximum deviation of 0.52 mm (on right side). For the kinetics analysis, the experiments data are extracted from those with water thickness range from 0.46mm to 0.67mm to ensure the adequate amount of water to form the equilibrium state was provided. Different experiments of the triple line location deviations can be seen in Fig. A3 for left side and Fig. A4 for right side. The averaged triple line locations with error bars can be seen in Fig. A5 for left side and Fig.A6 for right side.

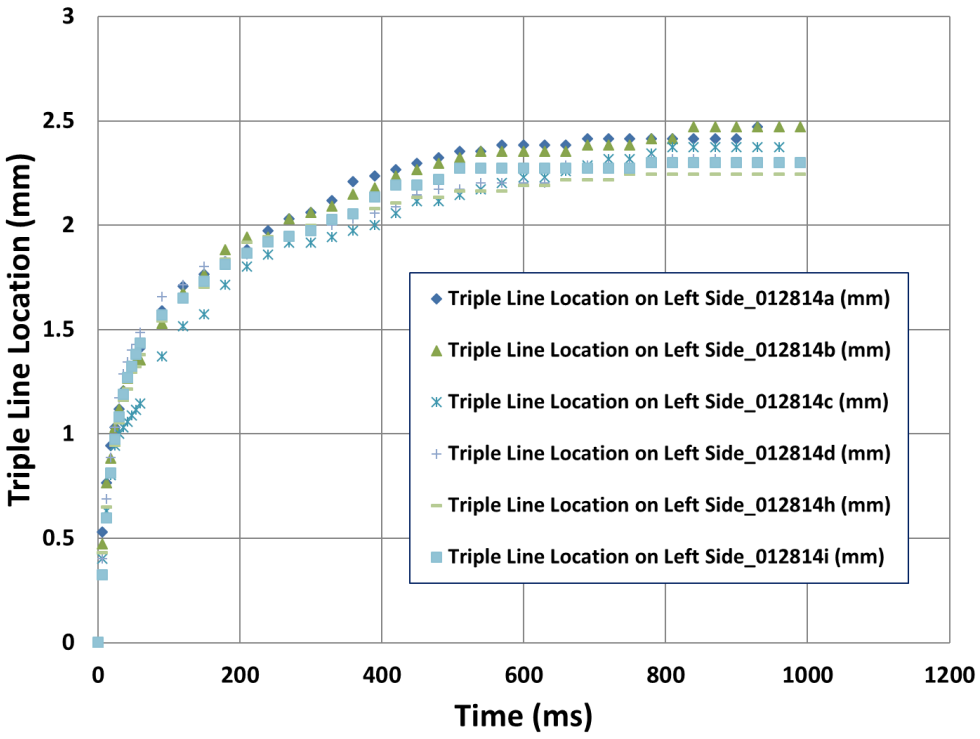

Fig. A3 Triple line location of different experiments on left side

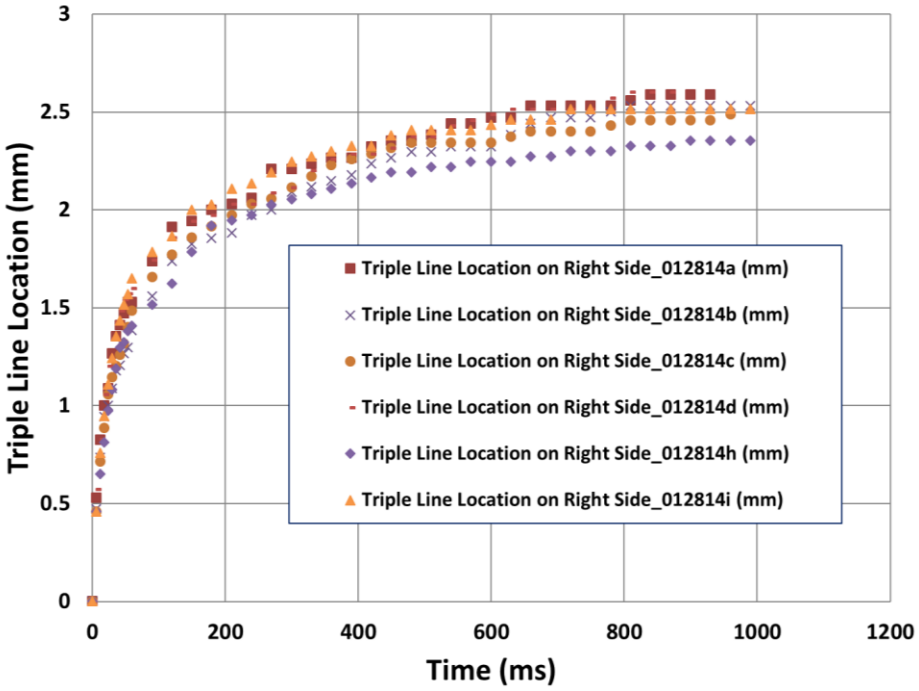

Fig. A4 Triple line location of different experiments on right side

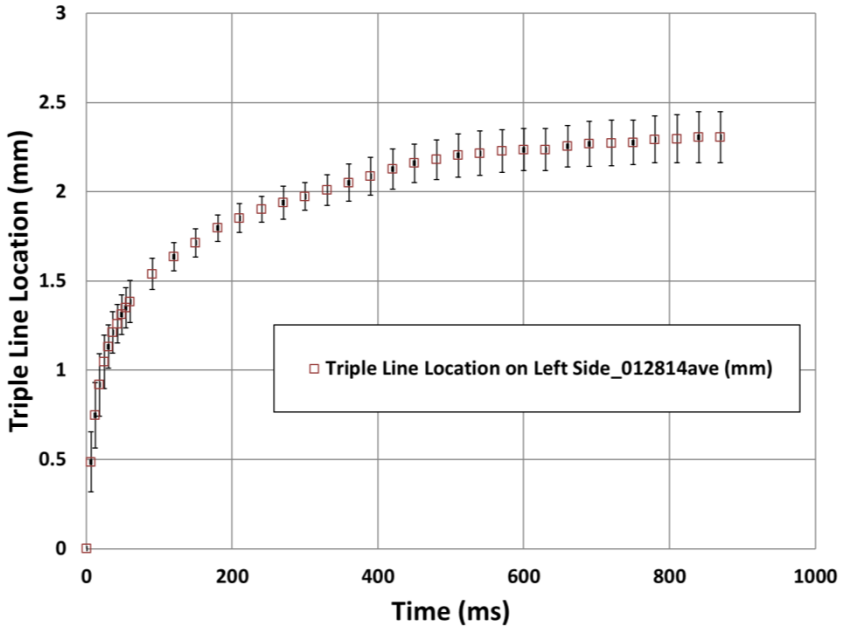

Fig. A5 Average triple line location of different experiments on right side with error bars

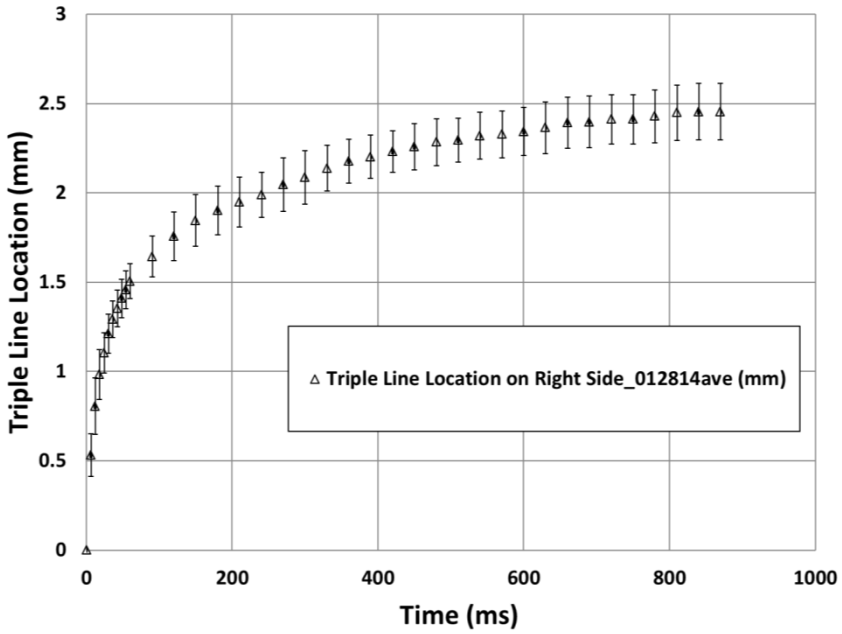

Fig. A6 Average triple line location of different experiments on left side with error bars

Therefore, it can be seen from the above figures that experimental condition, namely the glass surface condition variation can cause a larger data deviation than the measurement error. Also for the same set of experiments on both sides, a deviation between the right and the left can be observed, causing the error. However, for the kinetics analysis, only one side of the kinetics data is considered, thus the geometric error was eliminated.

Finally, as the experiment configuration is known as Wilhelmy plate configuration, thus the real execution required the vertical plate to move slowly down to the water surface. The vertical plate movement might potentially impose an impact on the experiment data result. Therefore, the speed of the vertical plate movement is analyzed to compare with the experiment data for triple line kinetics, see Fig. A7 and Fig. A8.

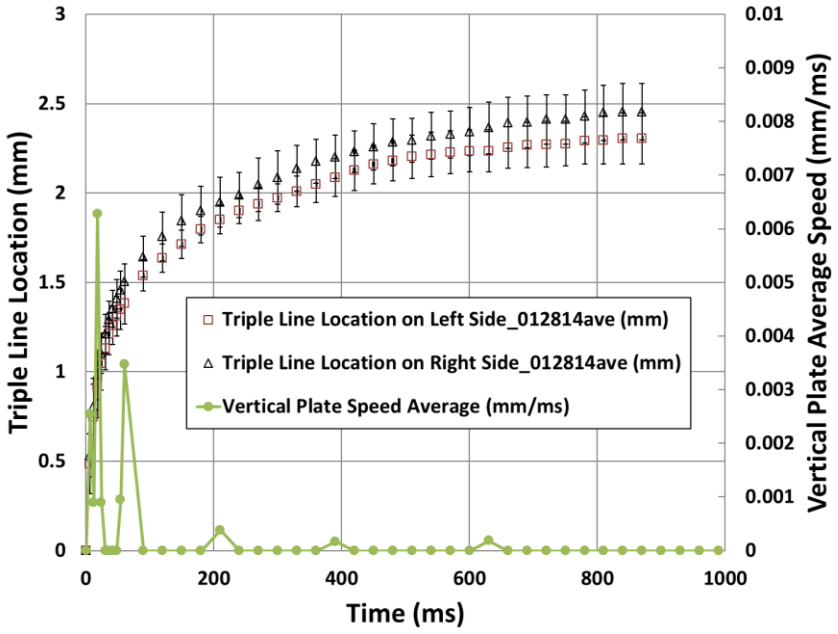

Fig. A7 Average triple line location of different experiments on left side with error bars and vertical plate speed

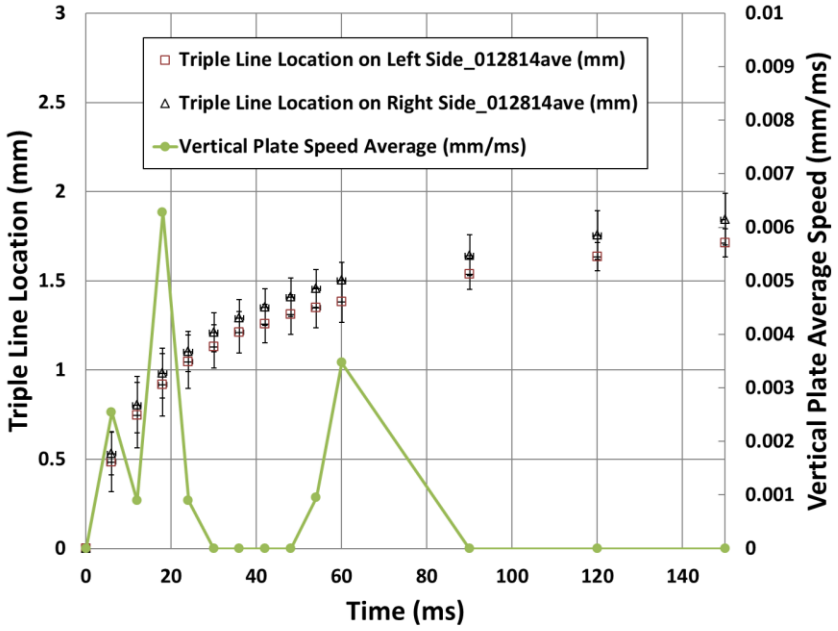

Fig. A8 Average triple line location of different experiments on left side with error bars and vertical plate speed in the first 150ms

In Fig. A7 and Fig. A8, one set of experiment from water on glass system is analyzed with the speed of the vertical plate. The average vertical plate speed is shown in Fig. 3.33. It can be seen that most of the movement takes place in the first 150 milliseconds. The vertical plate initially moves towards the water layer for the contact. The movement of the vertical plate is not uniform and but is still neglected. The zoomed-in plot in Fig. A8 shows that in the first 150 milliseconds, the vertical plate movement doesn't have an impact on the triple line location kinetics (no significant changes in the slope of the kinetics curve corresponding to that time range. The largest speed of the vertical surface in these experiments was 0.016 mm/ms (0.016m/s) in the experiment 012814d, and the absence of an impact of the speed is shown in Fig. A9.

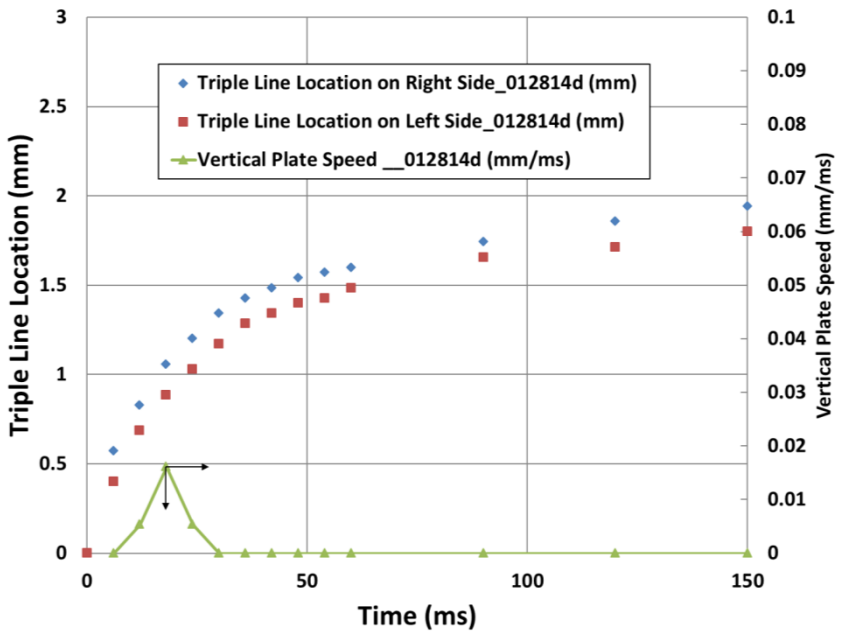

Fig. A9 Experiment 012814d triple line location kinetics and vertical plate speed in the first 150ms

From Fig. A9, the movement of the plate imposed on the liquid surface doesn't have the obvious impact on the triple line kinetics. Therefore, based on the above analysis, given enough water volume (water layer thickness between 0.46 mm and 0.67mm), the

deviation of the triple line kinetics most likely is caused by the glass plate surface condition variations (in spite of consistent use of virgin plates for each test).

Appendix B

Molten clad metal wetting on the non-wetting surface

In the non-wetting surface case, the alumina surface substrate was used for the liquid molten clad metal to spread. The surface characteristics are discussed in Chapter 4. A solid Trillium^{TM} was cut into 1.5173g cube. The sample and the alumina substrate preparation has followed the procedures described in Section 4.2.2. The sample was heated above its melting point of 577 °C (Ogilvy et al., 2014). The recording started from the temperature of 577 °C and ended after at least 45 minutes when the complete spherical shape of the droplet was formed and maintained its shape for enough time in the isothermal state, see Fig. B1.

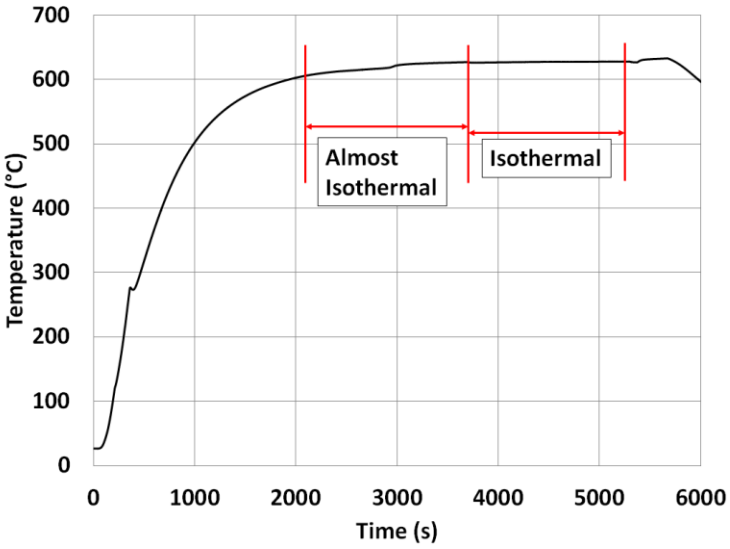

Fig. B1 Temperature profile of the sessile drop in the experiment of the non-wetting surface

Only a few selected images were taken in the isothermal state domain shown in Fig. B1. The temperature ramp rate in the isothermal regime is less than 0.028 °C/s. During the whole process, the oxygen level was maintained lower than 53 ppm.

The main purpose of the sessile drop experiment on the non-wetting surface is to determine the surface tension of the new material, Trillium^{TM}. The surface tension of the clad metal, liquid-vapor (γ_{lv}) may be interpreted as a measurable force existing at the triple line along the liquid-gas surface (Paddy, 1968). Among all of the surface tension measurement methods, sessile drop method was the most frequently used (Fig. B2 illustrated the configuration and offers the variables symbolism). Between the three surface tension components γ_{lv}, γ_{sl} and γ_{sv}, only γ_{lv} is measurable in the present work. The other measurable quantity is the contact angle θ (Kwok et al., 2000).

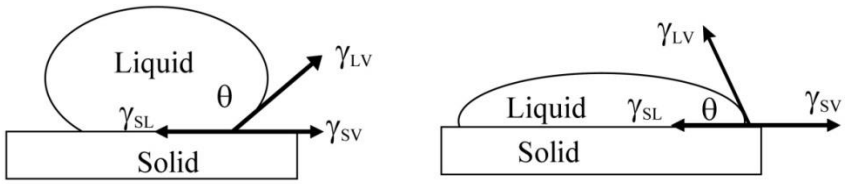

Fig. B2 Sessile drop surface tension

The equilibrium contact angle and surface tensions obey the relation of

$$\cos\theta = \frac{\gamma_{sl}-\gamma_{sv}}{\gamma_{lv}} \quad \text{(B1)}$$

where γ_{lv} is the surface tension between liquid and vapor, γ_{sv} is the surface energy between solid and vapor, γ_{sl} is the surface energy between solid and liquid. Surface tension $\gamma = \gamma_{lv}$ can also be related to the pressure difference across the surface and the radii of curvature (R_1 and R_2) at any point on the drop, based on the Laplace-Young equation:

$$\Delta P = \gamma \left(\frac{1}{R_1} - \frac{1}{R_2}\right) \quad \text{(B2)}$$

There are several correlations to determine the surface tension from the profile of a sessile drop. One of the most well established and most frequently used is the Bashforth and Adams equations (Anson et al., 1999):

$$\gamma = g\rho b^2/\beta \quad \text{(B3)}$$

where γ (= γ_{lv}) is the surface tension , g is the gravitational acceleration, ρ is the liquid density, b is the radius of the curvature at the apex O (Fig. B3) and β is a shape factor or Bond number which is dimensionless and represents the deviation of the drop profile from a sphere (Stalder et al., 2010). This equation assumes that gravity is a non-negligible force exerted by the droplet mass over the substrate.

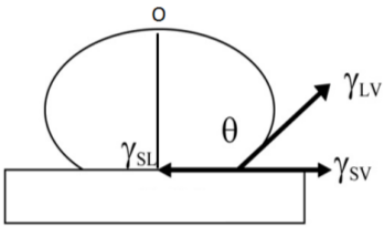

Fig.B3 Sessile drop apex point O

Given a horizontal and homogeneous substrate surface, the drop may be considered to be axisymmetric (Stalder et al., 2010). Anson et al. (1999) also used Dorsey equation to simplify the Bashforth and Adams calculations, by calculating the surface tension from an empirical equation. However, it is necessary to notice the limitation of the Dorsey equation for the liquid aluminum alloy sessile drop surface tension calculation. Namely, the accuracy of Dorsey equation highly depends on the size of the drop (it should be large enough) and contact angle should be larger than 90° (Paddy, 1968) (non-wetting case). The method to determine the contact angle and the capillary constant c ($c = \Delta\rho \cdot g/\gamma$, m^{-}

[2]) is based on the on the low-bond axisymmetric drop shape analysis (LBADSA) (Stalder et al., 2010). The method is implemented as a Java plug-in for the ImageJ software as mentioned in Chapter 4. It needs to be pointed out that LBADSA method can only be applied to small quasi-spherical drops whose diameter is of the order of magnitude of millimeters as used in our tests. The ImageJ measurements were conducted multiple times by using the region energy optimization option in the plug-in for the calculation of the capillary constant value with a comparison between the values obtained from other references (Anson et al., 1999; Guicoechea et al., 1992). The measured contact angle of the molten clad metal on the alumina non-wetting surface is 131 °± 0.5 °. The measured capillary constant is 6.42×10^4 m^{-2}.

The surface tension of the molten clad metal was tested by applying Dorsey equation (Anson et al., 1999). The empirical relation, Dorsey's equation (Dorsey 1928), was applied to calculate the surface tension of the clad metal alloy (Iida et al., 1988) (see Fig. B4):

$$\gamma_{lv} = g\rho X^2 \left(\frac{0.0520}{f} - 0.1227 + 0.0481f\right) \quad \text{(B4)}$$

where γ_{lv} is the surface tension, g is the gravitational acceleration, ρ is the density of the liquid alloy, X and Y are the experimental geometric parameters shown in Fig. B4, and the Dorsey factor f is given by

$$f = \frac{Y}{X} - 0.4142$$

The liquid alloy density ρ is not accurately known for many common alloys and is sometimes a major source of error (Anson et al., 1999). For silicon concentration from 0 to 15 wt%, the density (g/cm^3) of liquid alloy is given by Anson et al. (1999):

$$\rho = (0.3970 + 4.0924 \times 10^{-5}T - 1.04 \times 10^{-3}C_L)^{-1} \quad \text{(B5)}$$

where T is in degrees Celsius and C_L is the weight percent silicon.

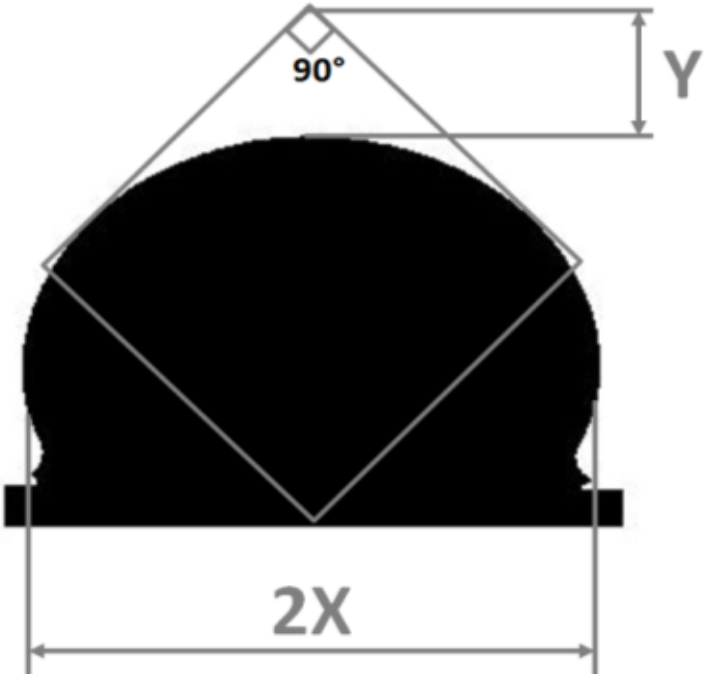

Fig. B4 Surface tension measurement of sessile drop for molten clad metal over an Al_2O_3 surface using Dorsey method

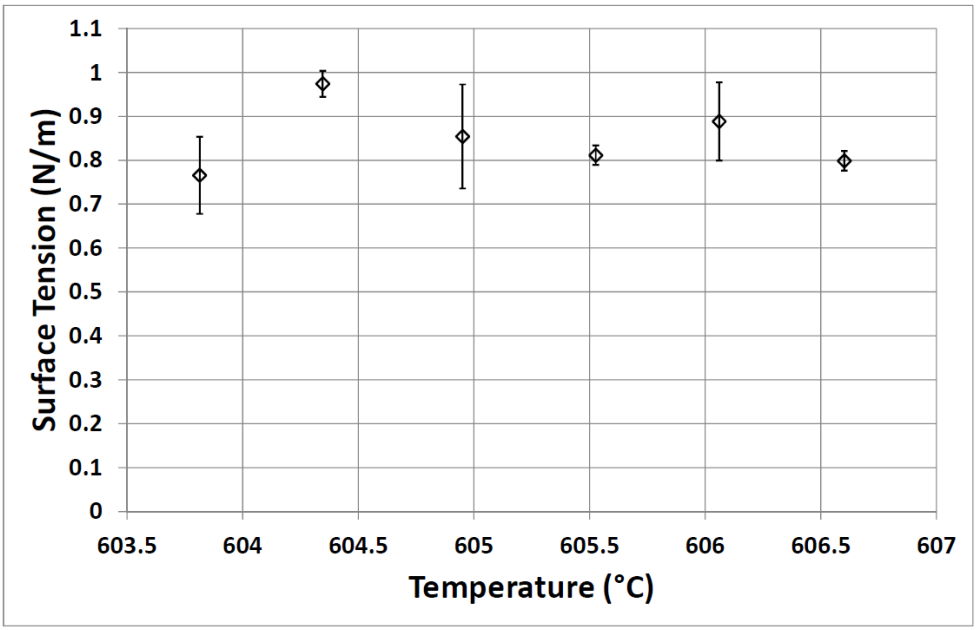

Fig. B5 Measured surface tensions of the clad metal at different temperatures

The measured surface tensions are plotted in Fig. B5 with standard deviation bars. It can be seen that from 603.5 °C to 607 °C, the surface tension variation is relatively small. The measured average surface tension of the clad metal was 0.849 N/m ± 0.042 N/m.

A repeated sessile drop experiment was conducted to verify the measured surface tension result. A sizably larger drop formation on the non-wetting alumina surface was captured by the video recorded. A screenshot comparison between the two tests is shown in Fig. B6. A solid Trillium^{TM} of 2.73 g was cut into a cube to allow the spherical shape to form on the non-wetting alumina substrate. The same procedure was followed with a higher ending temperature and longer dwell time on the substrate.

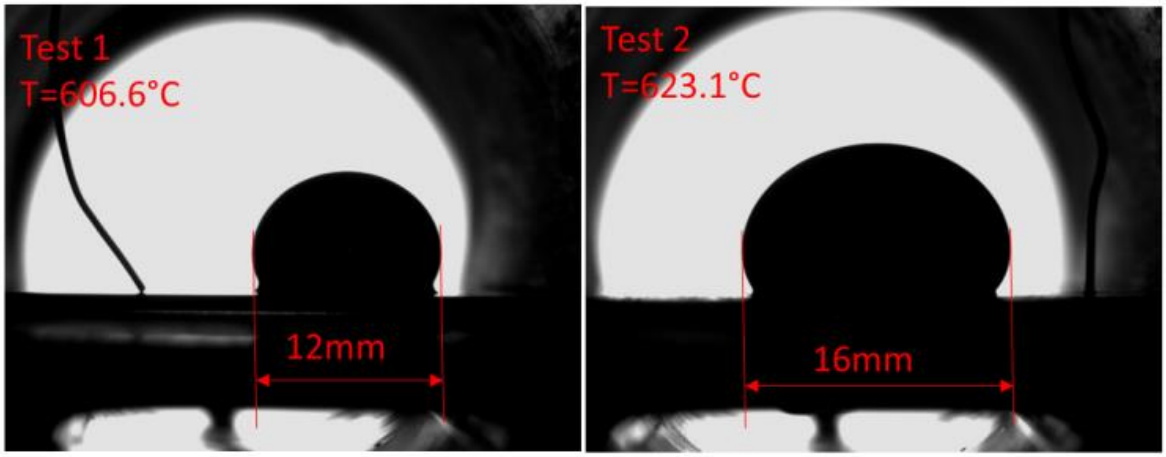

Fig. B6 Sessile drop on non-wetting surface tests comparison

The second test drop sample is 33% larger than the first time. The measured surface tension of the second time is 0.870 N/m±0.021 N/m, compared to the previous value of 0.849 N/m±0.042 N/m.

Appendix C

Surface tension literature review

It is well known that the surface tension decreases as the temperature increases. Although different forms of the relationship may be identified in different reports, Keene et al. (1993) established the relationship of surface tension with temperature as $\gamma = 871 - 0.155(T - 660°C)$ mNm^{-1}. Mills et al. (2006) updated the relationship as $\gamma = 875 - 0.18(T - 660°C)$ mNm^{-1} for the case of the presence of oxygen in the background atmosphere.

Another approach to the surface tension value determination of the molten aluminum was based on a theory developed to allow one to calculate the surface tension of nonionic solids (Skapski et al., 1956), such as the Skapski model, Eyring Model and Schoutens

model, etc. The theoretical consideration is based on a classical statistical thermodynamics formulation of Skapski et al. (1956), and Eyring and his coworkers (Aqra et al., 2012). Based on these models, several modified version were developed. The calculated values were of the order of 1000 $mNm^{-}1$.The calculated values are higher than the experimental values. The deviations in the experimental values lead to a decrease of the surface tension due to the oxygen contamination. Since γ_{sv} and γ_{sl} were calculated based on the definition of the contact angle (Kwok et al., 2000), and it is necessary to point out that the methodology was actually applicable for a low temperature, non-metal surface tension calculations. The situation for metals may be different, with the continuous non-equilibrium state in molten metal in a presence of oxygen. Aqra et al. (2012) compared their calculated results with the data reported from experiments (γ_{lv}) or calculations (γ_{sv}), giving a surface tension relationship with temperature as $\gamma = 985 - 0.275(T - 660°C)$ mJm^{-2} in the range of 660 to 927 ℃. It should be noted that a comprehensive calculation for aluminum alloys surface tension γ_{lv}, surface energy $\gamma_{sv}$and crystal-melt interfacial energy γ_{sl} are still not available, although single surface tension γ_{lv} calculation for alloys was often reported (Su et al., 2005). The surface tensions of alumina and its alloys from various literature sources are listed in Table C1.

Table C1 (Continued) Surface tension γ_{lv} of aluminum and aluminum alloys

Metal Type	**γ_{lv} (mN/m)**	**T (°C)**	**Gas Condition**	**Method**	**Year**	**Reference**
Al	713±11	1650	N/A	Sessile Drop	1997	Naidich et al., 1998
Al	846	800	N/A	Sessile Drop	1999	Anson et al., 1999
Al	870	660	Vacuum	Sessile Drop	1974	Eustathopoulos et al., 1974
Al	520	700-820	N/A	Capillary	1914	Flint et al.,

						1965
Al	300	~700	Ar	MBP (Maximum Bubble Pressure)	1936	Eustathopoulos et al., 1974
Al	502	712	N/A	Detachment	1937	Eustathopoulos et al., 1974
Al	500	660	Ar	MBP	1937	Zhivov et al., 1937
Al	914	660	N2	MBP	1948	Eustathopoulos et al., 1974
Al	860	725	Ar	MBP	1960	Eustathopoulos, 1974
Al	865	660	Vacuum	Large Drop	1961	Eustathopoulos et al., 1974
Al	825	660	Ar	MBP	1963	Eustathopoulos et al., 1974
Al	760	660	Vacuum	Sessile Drop	1970	Eustathopoulos et al., 1974
Al	915	660	Ar	Sessile Drop	1971	Eustathopoulos et al., 1974
Al	855	660	Ar	MBP	1973	Martins et al., 1988
Al-AlF3	~650	1000	Electrolyte	Sessile Drop	1985	Utigard et al., 1985
Al (12 wt%)	847	700	N/A	MBP	1992	Goiceochea et al., 1992
A356	845	700	Ar	MBP	1992	Goiceochea et al., 1992
A356	790	712	Ar	Sessile Drop	1993	Anson et al., 1999
A356 (Sr)	640	712	Ar	Sessile Drop	1993	Anson et al., 1999
A356	889±25	630	Vacuum	Sessile Drop	1999	Anson et al., 1999
A356	874±27	630	Hydrogen	Sessile Drop	1999	Anson et al., 1999
A356 (Sr)	844±32	630	Vacuum	Sessile Drop	1999	Anson et al., 1999
A356 (Sr)	801±7	630	Hydrogen	Sessile Drop	1999	Anson et al., 1999
Al–In (0.13 at% In)	577.6	650–700	Vacuum	Large Drop	2003	Alchagirov et al., 2003
Al	1050	660	CO_2	Surface Oscillation	2003	Sarou-Kanian et al., 2003
Al (1 wt% Pb)	662	750	N_2	Infiltration	1993	Alonso et al., 1993

Al	863	750	N_2	Infiltration	1993	Alonso et al., 1993
Al	861	700	N/A	N/A	1984	Hatch et al., 1984
Al (1% Mg)	658	700	N/A	N/A	1984	Hatch et al., 1984
Al (5% Mg)	601	700	N/A	N/A	1984	Hatch et al., 1984
Al (5% Zn)	846	700	N/A	N/A	1984	Hatch et al., 1984
Al (5% Si)	808	700	N/A	N/A	1984	Hatch et al., 1984
Al	914	660	N/A	N/A	1988	T. Iida et al., 1988
Al	948-0.202T (K)	770-817	Vacuum	Sessile Drop	1970	Rhee et al., 1970
Al	690	N/A	N/A	Linear Interpolation	1957	Rhee et al., 1970
Al	780	N/A	N/A	Linear Interpolation	1957	Rhee et al., 1970
Al	720	N/A	N/A	Linear Interpolation	1957	Rhee et al., 1970
Al	650	N/A	N/A	Linear Interpolation	1957	Rhee et al., 1970
Al (11.8 wi % Si)	817	N/A	N/A	N/A	2001	Hashim et al., 2001
Al	865	660	N/A	Sessile Drop	1979	Goumiri et al., 1979
Al	866	660	N/A	Sessile Drop	1968	ES Levin et al., 1968
Al	865	660	N/A	Sessile Drop	1938	Andreas et al., 1938
Al	930	660	N/A	Sessile Drop	1975	Popel et al., 1975
Al	740	1500	N/A	Sessile Drop	1971	Keene, 1993
Al	880	660	N/A	Sessile Drop	1977	Keene, 1993
Al	815	1000	N/A	Sessile Drop	1969	Keene, 1993
Al	825	660	N/A	MBP	1963	Keene, 1993
Al	1100	800	N/A	MBP	1986	Keene, 1993
Al	865	800	N/A	MBP	1986	Keene, 1993
Al	865	660	N/A	Sessile Drop	1974	Keene, 1993
Al	868	660	N/A	MBP	1977	Keene, 1993

Al	865	660	N/A	Sessile Drop	1972	Keene, 1993
Al	913	660	N/A	MBP	1949	Keene, 1993
Al	1050	700	N/A	Sessile Drop	1982	Keene, 1993
Al	870	660	N/A	Sessile Drop	1974	Keene, 1993
Al	868	660	N/A	MBP	1974	Keene, 1993
Al	873	660	N/A	Sessile Drop	1969	Keene, 1993
Al	1090	700	N/A	MBP	1984	Keene, 1993
Al	868	700	Saturated with O_2	MBP	1984	Keene, 1993
Al (O saturated)	871 - 0.155·(t - 660)	N/A	N/A	Curve Fitting	1993	Keene, 1993
Al	985 (Model Value)	660	N/A	Eyring Model	2012	Aqra et al., 2012
Al	1045 (Model Value)	660	N/A	Modified Skapski Model	2009	Iida et al., 2009
Al	881- 0.2·(t - 660)	620-1150	O_2 contamination	Large Drop	2001	Egry et al., 2001
Al	868- 0.25·(t - 660)	697-897	O_2 contamination	Draining Crucible	2005	Mills et al., 2006
Al	1100	800	No O_2	MBP	1986	Goicoechea et al., 1992
Al	1050	700	No O_2	Sessile Drop	1982	Goumiri et al., 1982
Al	1090	700	No O_2	MBP	1984	Pamies et al., 1984
Al	1024- 0.274·(t - 660)	1517- 1897	No O_2	Large Drop	2003	Sarou-Kanian et al., 2003
Al	1031 (Model Value)	660	N/A	Modified Skapski Model	2005	Lu et al., 2005

Appendix D

Wedge-tee joint meniscus curvature

In the 0.4 mm thickness clad metal configuration at the joint area after formation, a final image is taken and shown in Fig. D1.

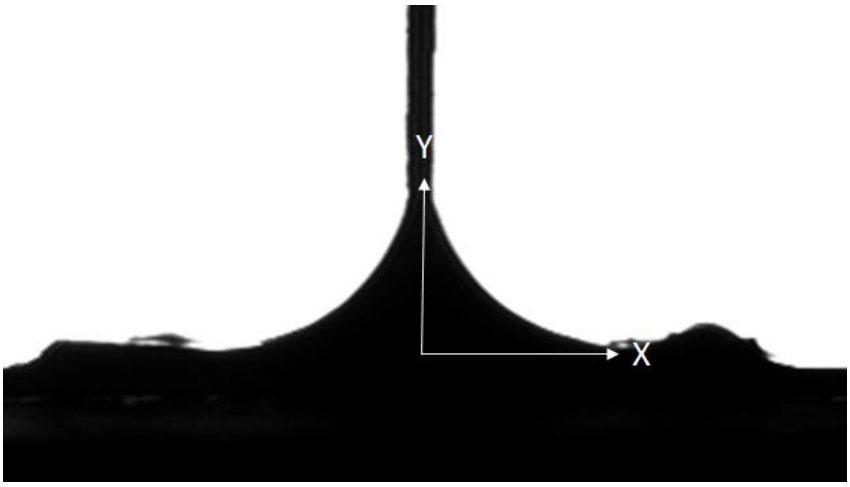

Fig. D1 0.4mm thickness clad metal triple line meniscus at 120 second, experiment 08142014

The right side of the meniscus can be fitted as a polynomial function of y = -0.0609x5 + 0.5925x4 - 1.8034x3 + 2.7841x2 - 2.8853x + 1.6347, with $R^2 = 0.9993$, see Fig. D2. The curvature was calculated from the equation of curvature:

$$\kappa = \frac{\frac{d^2y}{dx^2}}{\left[1+\left(\frac{dy}{dx}\right)^2\right]^{3/2}} \quad \text{(D1)}$$

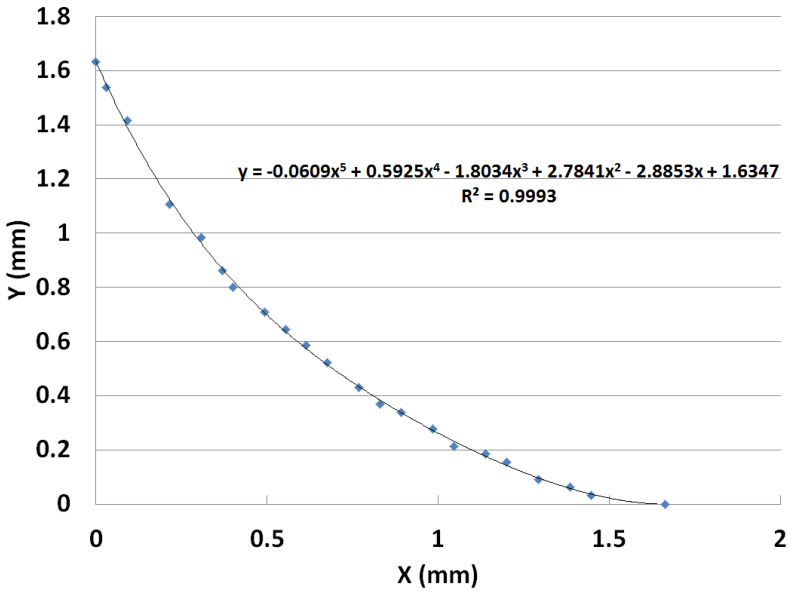

Fig. D2 0.4mm thickness Trillium meniscus polynomial fitting on the right side

The curvature can be plotted in Fig. D3.

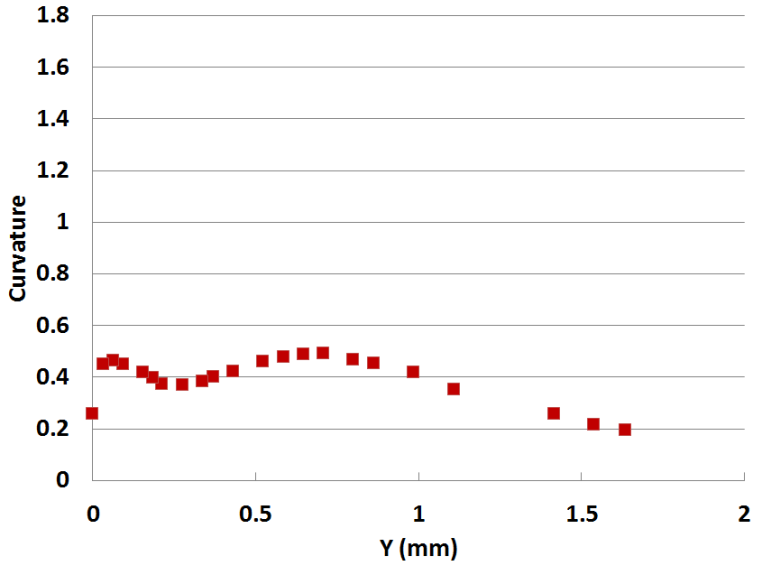

Fig. D3 0.4mm thickness clad metal meniscus of the right side curvature vs. y(x)

Appendix E

Phase field model analysis (Fu et al., 2016, Dehsara et al., 2016)

In the non-reactive spreading case, surface tension and viscosity play a decisive role in controlling the kinetics of the triple line. Phase-field models for multi-phase flows require that mass density be a function of the phase variable. The phase field model for capillary flow presented here is largely based on Lowengrub (1998) analysis. The model from Jacqmin (2000) provides a seamless and consistent diffusional motion of the triple line and it's a part of the overall formulation.

The phase field model is developed in order to verify the behavior of the non-reactive systems and the reactive systems at elevated temperatures Al-Si alloy complemented with particles of potassium-fluoroaluminate salts. The non-reactive isothermal wetting phase field model is built following Jacqmin (2000). In this case, two fluids are considered: liquid L and gas G, both incompressible with respective mass densities of $\rho_L$and ρ_G with viscosities of μ_L and μ_G. The boundary of the domain consists of the solid-fluid interface S and the far-field fluid boundary A, see Fig. E1.

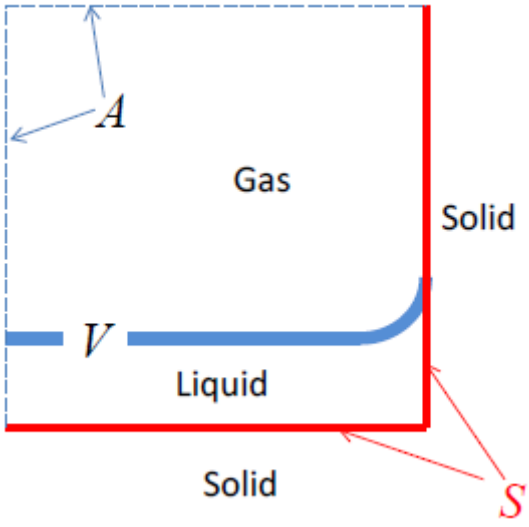

Fig. E1 Illustration of the domain and its boundary for wedge-tee joint area

The liquid and gas are distinguished by the phase-field variable $\phi(\mathbf{x})$, which takes value 1 in the liquid, and value 0 in the gas. The values between 0 and 1 represent a thin interface layer between two fluids. The free energy density of the two-phase system (liquid and gas) can be combined and expressed as:

$$\omega(\phi, \nabla\phi) = f(\phi) + \frac{1}{2}\kappa(\nabla\phi)^2 \tag{E1}$$

where $f(\phi)$ is a double-well potential illustrated in Fig. E2

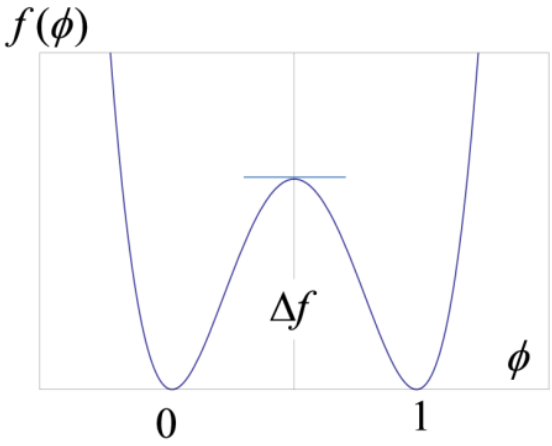

Fig. E2 Double-well potential featuring the energetic barrier

For immiscible fluids the only relevant parameter is the height of the energetic barrier Δf. The material properties: viscosity $\mu(\phi)$, mass density $\rho(\phi)$ and fluid-solid interface energy $\gamma(\phi)$, are interpolated between the known quantities for the liquid and gas phases as:

$$\mu(\phi) = \mu_L\psi_0(\phi) + \mu_G\psi_1(\phi);$$

$$\rho(\phi) = \rho_L\psi_0(\phi) + \rho_G\psi_1(\phi);$$

$$\gamma(\phi) = \gamma_L\psi_0(\phi) + \gamma_G\psi_1(\phi). \tag{E2}$$

The interpolation functions must satisfy

$$\psi_0(\phi) + \psi_1(\phi) = 1; \psi_0(\phi \leq 0) = 0; \psi_0(\phi \geq 1) = 1 \qquad \text{(E3)}$$

The governing equations of the incompressible model consist of the modified Navier-Stokes equations, the incompressibility condition and the 4th order Cahn-Hilliard diffusion equation for the conserved phase field (Fu et al., 2016) as:

$$\rho \frac{D\mathbf{v}}{Dt} = \rho\mathbf{g} + \nabla \cdot [\mu(\mathbf{v}\nabla + \nabla\mathbf{v})] - \nabla\pi + M\nabla\phi; \qquad \nabla \cdot \mathbf{v} = 0;$$

$$\frac{D\phi}{Dt} = B\nabla^2 M; \qquad M = \frac{df}{d\phi} - \kappa\nabla^2\phi. \qquad \text{(E4)}$$

where $\mathbf{v}(\mathbf{x})$ is velocity, $\pi(\mathbf{x})$ is incomplete pressure (including capillary and non-capillary portions), B is the interface mobility, $\phi(\mathbf{x})$ is the phase field, D/Dt is the material derivative, $\mathbf{g}$ is the gravitational acceleration, and the dyadic $\mathbf{v}\nabla$ is a rank-2 tensor with components $(\mathbf{v}\nabla)_{ij} = \partial v_i/\partial x_j$. The total pressure can be computed as:

$$p = \pi - f - \frac{1}{6}\kappa(\nabla\phi)^2 \qquad \text{(E5)}$$

The parameters κ and Δf are computed from the interface energy between the fluids Γ and the chosen width of the fluid-fluid interface (phase-field transition) h :

$$\kappa = \frac{3}{2}\Gamma h, \quad \Delta f = \frac{3}{4}\Gamma/h, \qquad \text{(E6)}$$

where h is chosen to be much smaller than the smallest expected radius of curvature of the fluid-fluid interface. In simulations, interface mobility B range should be first defined, so that the results are insensitive to the order-of-magnitude changes in B. The capillary stress tensor field is as follows:

$$\boldsymbol{\sigma} = (\omega - M\phi)\mathbf{I} - \kappa\nabla\phi\nabla\phi, \qquad \text{(E7)}$$

when integrated across the fluid-fluid interface, gives the surface tension Γ and the portion of the pressure jump across a curved interface (the other potion is contained in π).

On the interface between the solid and the two fluids, the triple line motion is described by the diffusive boundary condition (Jacqmin, 2000):

$$\partial\phi/\partial t = -b(\kappa\mathbf{n}\cdot\nabla\phi + d\gamma/d\phi) \tag{E8}$$

where unit interface normal $\mathbf{n}$ points away from the fluids.

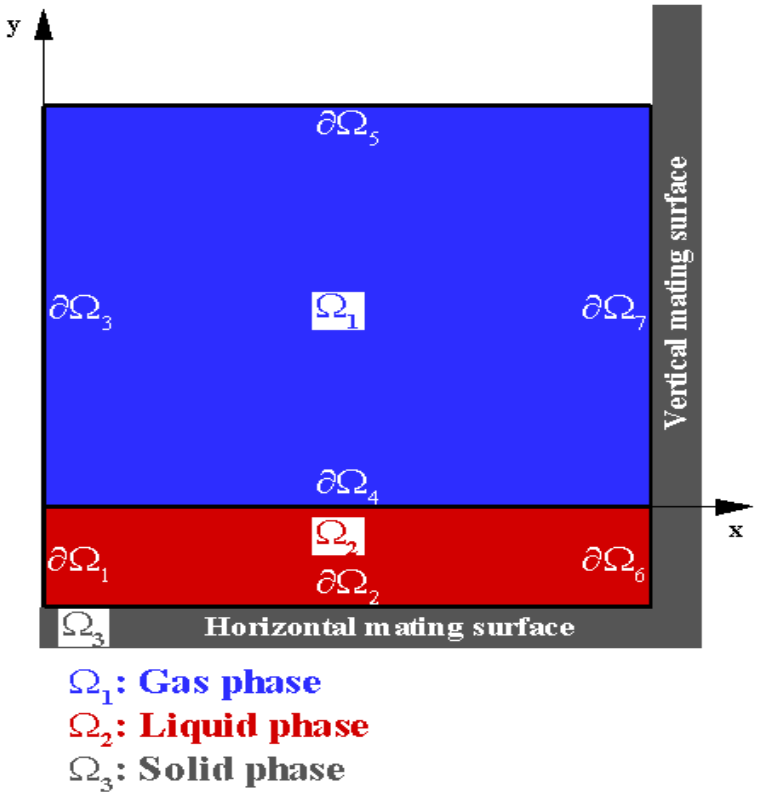

Fig. E3 Schematic of the wedge-tee joint domain

The phase field model formulation has been implemented in both Comsol MultiPhysics 3.5a and Comsol MultiPhysics 4.3. The schematic of the model is shown in Fig. E3. The 2-D model of water with unstructured triangular mesh is generated by the adaptive mesh

method with interfacial refinement for raising the triple line, see Fig. E4. The interface thickness and the minimum element size are 0.1mm and 9×10^{-3}mm, respectively.

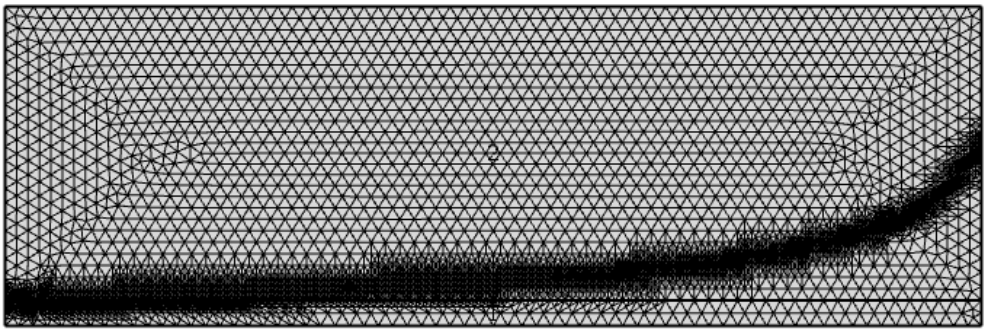

Fig. E4 The final (equilibrium) triangular mesh generated by adaptive mesh method (water).

Based on Fig. E3, the boundary conditions can be summarized as:

$$\mathbf{v} = 0, \text{ at right and bottom}$$

$$\frac{\partial \phi}{\partial t} = -b\left(\kappa \mathbf{n}\cdot\nabla\phi + \frac{d\gamma}{d\phi}\right), \text{ at right side and bottom}$$

$$n \cdot B\nabla^2 M = 0, \text{ at all boundaries}$$

$$\mathbf{n}\cdot\nabla\phi = 0, \text{at left side and top side}$$

$$\mathbf{n}\cdot[\mu(\mathbf{v}\nabla + \nabla\mathbf{v})] = 0, \frac{\partial \pi_3}{\partial y} = -\rho(\phi(y))\text{g, at left side}$$

$$\mathbf{n}\cdot\nabla\mathbf{v} = 0, \pi = 0 \text{ at top}$$

The simulation reproduces the triple line kinetics from experiments, as shown in Fig. E5. As analyzed in Chapter 3, water flows to the joint area quickly until the water film is depleted, and surface tension with viscous force dominates the triple line kinetics. Both experiment and simulation results show the expected process in Fig. E5.

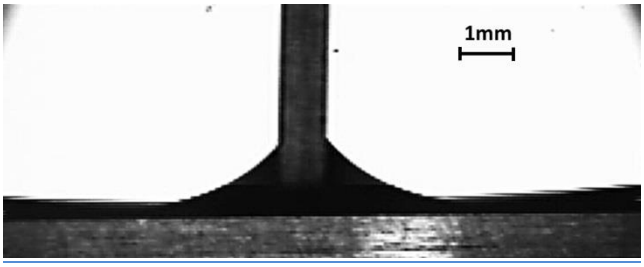

(a)

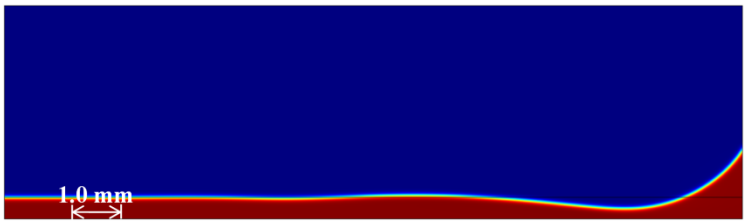

(b)

Fig. E5 The formation of the wave in the water pool following the initial surge of the triple line (a) Experimental (19ms); (b) Computational (20ms)

The triple line mobility *b* is fitted to the initial velocity of the triple line. In this particular experimental setup, the initial motion of the triple line is unimpeded by inertia and viscosity, so that the initial triple line velocity is only dependent on the parameter *b*. The rest of the motion serves at the benchmark for the computational kinetics. The equilibrium shape of the meniscus can be determined analytically (neglecting the mass density of the gas). The kinetics simulation results for both water and silicone oil compared with experiments are shown in Fig. E6. The simulation results show excellent agreement with the experimental results.

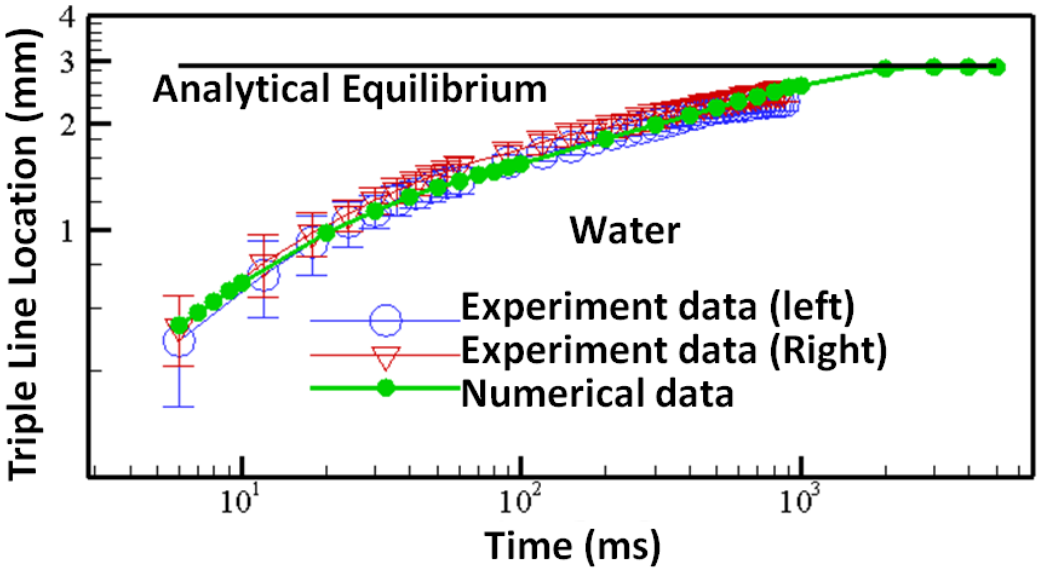

(a)

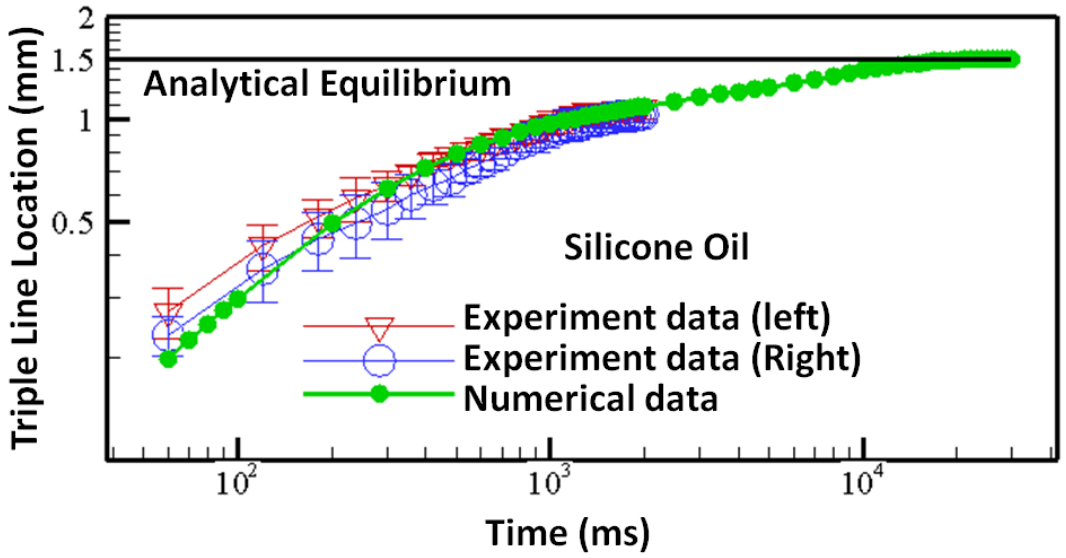

(b)

Fig. E6 Triple line kinetics for (a) water, and (b) Silicone oil comparison between numerical results and experimental result. The triple line mobility *b* is fitted to the initial slope

In the reactive spreading at elevated temperatures for the molten clad metal on aluminum AA3003 (Al-Si alloy in nitrogen atmosphere), it is assumed that diffusion controlled concentration changes do not significantly affect the fluid viscosity, and that their effect on the TPL mobility can be phenomenologically included in the model through the triple line mobility parameter, although the diffusion and concentration changes are not explicitly modeled. The equilibrium contact angle is taken into the numerical analysis from the experiments regardless of the concentration in phases meeting at the triple line location. The simulation meniscus shape and the experimental meniscus comparison can be seen in Fig. E7.

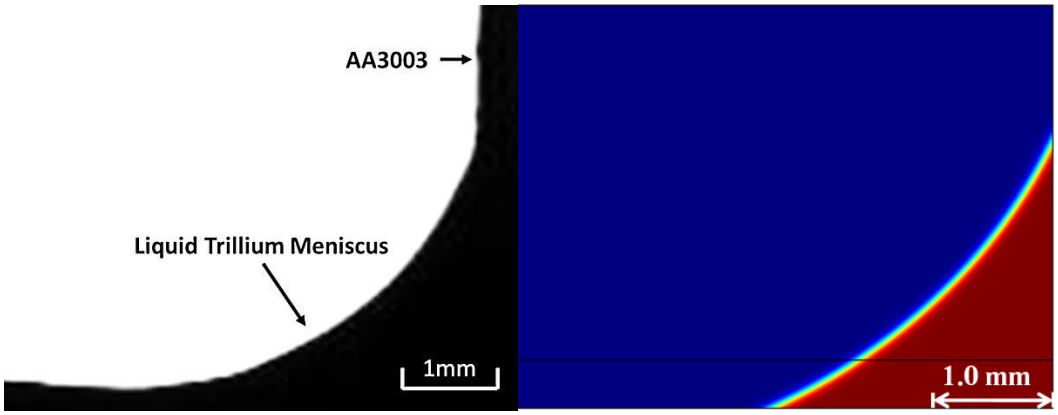

(a) (b)

Fig. E7 (a) Optical Contact Analyzer image Trillium wedged-tee joint formed at 600ºC at 120 second (08142014), (b) Equilibrium shape of trillium meniscus with viscosity 1 mPa-s at 200s.

REFERENCES

- De Gennes, P.-G. (1985). "Wetting: statics and dynamics." Reviews of Modern Physics 57(3): 827
- Voinov, O. (1976). "Hydrodynamics of wetting." Fluid Dynamics 11(5): 714-721.
- Dussan, E. (1979). "On the spreading of liquids on solid surfaces: static and dynamic contact lines." Annual Review of Fluid Mechanics 11(1): 371-400.
- Kistler, S. (1993). "Hydrodynamics of wetting." Wettability 6: 311-430.
- Eustathopoulos, N., et al. (1999). Wettability at high temperatures, Elsevier.
- Quéré, D. (2008). "Wetting and roughness." Annu. Rev. Mater. Res. 38: 71-99.
- Bonn, D., et al. (2009). "Wetting and spreading." Reviews of Modern Physics 81(2): 739.
- Sui, Y., et al. (2014). "Numerical simulations of flows with moving contact lines." Annual Review of Fluid Mechanics 46: 97-119.
- Sekulic, D. P. (2011). "Wetting and spreading of liquid metals through open microgrooves and surface alterations." Heat Transfer Engineering 32(7-8): 648-657.
- Zhao, H. and D. Sekulic (2006). "Diffusion-controlled melting and re-solidification of metal micro layers on a reactive substrate." Heat and Mass Transfer 42(6): 464-469.
- Busbaher, D., et al. (2010). P1–26: High temperature brazing using nano-particles doped filler metal for dispenser cathode applications. Vacuum Electronics Conference (IVEC), 2010 IEEE International.
- Schwartz, M. M. (2003). Brazing, ASM international.
- Ogilvy, A. J. W., Hawkswoth, D. K., Abom, E., "Brazing piece, a method of making a brazing piece, and a method of brazing and components made from said brazing piece." U.S. Patent No. 8,871,356. 28 Oct. 2014.
- Yu, C.-N., et al. (2013). An Analysis of an Impact of the Background Atmosphere on the Aluminum Brazing Joint Formation. ASME 2013 International Mechanical Engineering Congress and Exposition, American Society of Mechanical Engineers.

- Hawksworth, D. K. (2012). Clad Melting and Joint Formation in Aluminum Brazing Under Severe Alterations of the Background Atmosphere: A Superior New Brazing Sheet Material Vs. a Traditional Brazing Sheet. 5th International Brazing and Soldering Conference, Asm.
- Sekulić, D. P. (2013). Advances in brazing: science, technology and applications, Elsevier.
- Fu, H., Dong, F., Sekulic, D. P., Mesarovic, S. D., & Krivilyov, M. (2013). Surface Tension Driven Kinetics of the Triple Line of a Liquid Metal Free Surface. In ASME 2013 International Mechanical Engineering Congress and Exposition , San Diego, USA
- Myers, D. (1999). "Wetting and spreading." Surfaces, Interfaces, and Colloids: Principles and Applications, Second Edition: 415-447.
- De Gennes, P.-G., et al. (2013). Capillarity and wetting phenomena: drops, bubbles, pearls, waves, Springer Science & Business Media.
- Yuan, Y. and T. R. Lee (2013). Contact angle and wetting properties. Surface science techniques, Springer: 3-34.
- Blake, T. and J. Haynes (1973). "Contact-angle hysteresis." Progress in surface and membrane science 6: 125-138.
- Rillaerts, E. and P. Joos (1980). "The dynamic contact angle." Chemical Engineering Science 35(4): 883-887.
- Johnson Jr, R. E., et al. (1977). "Dynamic contact angles and contact angle hysteresis." Journal of Colloid and Interface Science 62(2): 205-212.
- Seebergh, J. E. and J. C. Berg (1992). "Dynamic wetting in the low capillary number regime." Chemical Engineering Science 47(17): 4455-4464.
- Joanny, J. and P.-G. De Gennes (1984). "A model for contact angle hysteresis." The Journal of Chemical Physics 81(1): 552-562.
- Eral, H. and J. Oh (2013). "Contact angle hysteresis: a review of fundamentals and applications." Colloid and polymer science 291(2): 247-260.
- Young, T. (1805). "An essay on the cohesion of fluids." Philosophical Transactions of the Royal Society of London: 65-87.

- Washburn, E. W. (1921). "The Dynamics of Capillary Flow." Physical Review 17(3): 273-283.
- Han, J. and C. Kim (2014). "Theoretical and experimental studies on the contact line motion of second-order fluid." Rheologica Acta 53(1): 55-66.
- Šikalo, Š., et al. (2005). "Dynamic contact angle of spreading droplets: Experiments and simulations." Physics of Fluids (1994-present) 17(6): -.
- Ström, G., et al. (1990). "Kinetics of steady-state wetting." Journal of Colloid and Interface Science 134(1): 107-116.
- Hocking, L. and A. Rivers (1982). "The spreading of a drop by capillary action." Journal of Fluid Mechanics 121: 425-442.
- Schwartz, A. M. and S. B. Tejada (1972). "Studies of dynamic contact angles on solids." Journal of Colloid and Interface Science 38(2): 359-375.
- Fermigier, M. and P. Jenffer (1991). "An experimental investigation of the dynamic contact angle in liquid-liquid systems." Journal of Colloid and Interface Science 146(1): 226-241.
- Sobolev, V., et al. (2000). "Surface tension and dynamic contact angle of water in thin quartz capillaries." Journal of Colloid and Interface Science 222(1): 51-54.
- Biance, A.-L., et al. (2004). "First steps in the spreading of a liquid droplet." Physical Review E 69(1): 016301.
- Lee, J. B. and S. H. Lee (2011). "Dynamic wetting and spreading characteristics of a liquid droplet impinging on hydrophobic textured surfaces." Langmuir 27(11): 6565-6573.
- Calvo, A., et al. (1991). "Dynamic capillary pressure variations in diphasic flows through glass capillaries." Journal of Colloid and Interface Science 141(2): 384-394.
- Stokes, J., et al. (1990). "Harmonic generation as a probe of dissipation at a moving contact line." Physical Review Letters 65(15): 1885.
- Wilhelmy, L. (1863). "Ueber die Abhängigkeit der Capillaritäts-Constanten des Alkohols von Substanz und Gestalt des benetzten festen Körpers." Annalen der Physik 195(6): 177-217.
- Cain, J., et al. (1983). "Dynamic contact angles on smooth and rough surfaces." Journal of Colloid and Interface Science 94(1): 123-130.

- Bracke, M., et al. (1989). The kinetics of wetting: the dynamic contact angle. Trends in Colloid and Interface Science III, Springer: 142-149.
- Adam, N. K. and G. Jessop (1925). "CCL.—Angles of contact and polarity of solid surfaces." Journal of the Chemical Society, Transactions 127: 1863-1868.
- Fowkes, F. M. and W. D. Harkins (1940). "The state of monolayers adsorbed at the interface solid—aqueous solution." Journal of the American Chemical Society 62(12): 3377-3386.
- Smedley, G. T. and D. E. Coles (2005). "A refractive tilting-plate technique for measurement of dynamic contact angles." Journal of Colloid and Interface Science 286(1): 310-318.
- Vagharchakian, L., et al. (2008). "Capillary Bridge Formation and Breakage: A Test to Characterize Antiadhesive Surfaces†." The Journal of Physical Chemistry B 113(12): 3769-3775.
- Restagno, F., et al. (2009). "Contact angle and contact angle hysteresis measurements using the capillary bridge technique." Langmuir 25(18): 11188-11196.
- Hoffman, R. L. (1975). "A study of the advancing interface. I. Interface shape in liquid—gas systems." Journal of Colloid and Interface Science 50(2): 228-241.
- Voinov, O. (1976). "Hydrodynamics of wetting." Fluid Dynamics 11(5): 714-721.
- Tanner, L. (1979). "The spreading of silicone oil drops on horizontal surfaces." Journal of Physics D: Applied Physics 12(9): 1473.
- Schwartz, A. M., & Tejada, S. B. (1970). NASA Contract Rep.
- Jiang, T.-S., et al. (1979). "Correlation for dynamic contact angle." Journal of Colloid and Interface Science 69(1): 74-77.
- Blake, T., et al. (1995). "Models of wetting: Immiscible lattice Boltzmann automata versus molecular kinetic theory." Langmuir 11(11): 4588-4592.
- Meier, A., et al. (1999). "Ceramic-metal interfaces and the spreading of reactive liquids." JOM 51(2): 44-47.
- Saiz, E. and A. P. Tomsia (1998). "Kinetics of Metal-Ceramic Composite Formation by Reactive Penetration of Silicates with Molten Aluminum." Journal of the American Ceramic Society 81(9): 2381-2393.

- Contreras, A., et al. (2003). "Wettability and spreading kinetics of Al and Mg on TiC." Scripta Materialia 48(12): 1625-1630.
- Meier, A., et al. (1998). "Modelling of the spreading kinetics of reactive brazing alloys on ceramic substrates: copper–titanium alloys on polycrystalline alumina." Acta Materialia 46(12): 4453-4467.
- Rado, C., et al. (2000). "The role of compound formation in reactive wetting: the Cu/SiC system." Acta Materialia 48(18): 4483-4491.
- Mortensen, A., et al. (1997). "Kinetics of diffusion-limited spreading of sessile drops in reactive wetting." Scripta Materialia 36(6): 645-651.
- Bailey, G. and H. Watkins (1951). "The flow of liquid metals on solid metal surfaces and its relation to soldering, brazing, and hot-dip coating." Journal of the Institute of Metals 80(2): 57-76.
- Li, J. (1992). "Kinetics of wetting and spreading of Cu-Ti alloys on alumina and glassy carbon substrates." Journal of Materials Science Letters 11(23): 1551-1554.
- Dezellus, O., et al. (2002). "Chemical reaction-limited spreading: the triple line velocity versus contact angle relation." Acta Materialia 50(19): 4741-4753.
- Zhao, H. (2005). Transport Phenomena Involving Molten Clad During Aluminum Brazing Process, University of Kentucky.
- Thorsen, K. A., et al. (1984). "Optical hot stage microscopy for brazing investigations." WELD J 63(11): 393.
- Fujii, H., et al. (1993). "Interfacial reaction wetting in the boron nitride/molten aluminum system." Acta Metallurgica et Materialia 41(10): 2963-2971.
- Weirauch, D. and W. Krafick (1990). "The effect of carbon on wetting of aluminum oxide by aluminum." Metallurgical Transactions A 21(6): 1745-1751.
- Hager, Willi H. (2012). "Wilfrid Noel Bond and the Bond number", Journal of Hydraulic Research 50 (1): 3–9.
- Bashforth, F. and J. C. Adams (1883). An attempt to test the theories of capillary action: by comparing the theoretical and measured forms of drops of fluid, University Press.
- Fu H., Dehsara M., Krivilyov M., Sekulic D.P., Mesarovic S.Dj., “Kinetics of the Molten Al-Si Triple Line Movement during a Brazed Joint Formation”, *Journal of*

Material Science, 2016, 51(4), 1798-1812.

- Chappuis, J., et al. (1982). "Multiphase Science and Technology." Eds. GF Hewitt, JM Delhaye, and N. Zuber, Hemisphere Publishing Corporation 1: 387.
- Rivollet, I., et al. (1990). "Simultaneous measurement of contact angles and work of adhesion in metal-ceramic systems by the immersion-emersion technique." Journal of Materials Science 25(7): 3179-3185.
- Liu, W. and D. P. Sekulic (2011). "Capillary driven molten metal flow over topographically complex substrates." Langmuir 27(11): 6720-6730.
- Zhao, H., et al. (2009). "Wetting Kinetics of Eutectic Lead and Lead-Free Solders: Spreading over the Cu Surface." Journal of Electronic Materials 38(2): 284-291.
- Yu, C.-N., et al. (2013). An Analysis of an Impact of the Background Atmosphere on the Aluminum Brazing Joint Formation. ASME 2013 International Mechanical Engineering Congress and Exposition, American Society of Mechanical Engineers.
- Zhao, H., et al. (2006). Surface tension driven molten metal flow over flat and/or grooved reactive surfaces during brazing and soldering. International Brazing and Soldering Conference, JJ Stephens, and KS Weil, Materials Park, OH: ASM International.
- Wen, L., et al. (2012). "Preferential spreading of molten metal over an anisotropically microstructured surface." EPL (Europhysics Letters) 97(4): 46003.
- Saiz, E. and Tomsia, A.P. (2005). "Kinetics of high-temperature spreading." Current Opinion in Solid State and Materials Science 9(4): 167-173.
- Saiz, E., et al. (2007). "Nonreactive spreading at high temperature: Molten metals and oxides on molybdenum." Physical Review E 76(4): 041602.
- Benhassine, M., et al. (2009). "Nonreactive spreading at high-temperature revisited for metal systems via molecular dynamics." Langmuir 25(19): 11450-11458.
- Champion, J., Keene, B., Sillwood, J. (1969). "Wetting of aluminium oxide by molten aluminium and other metals." Journal of Materials Science 4(1): 39-49.
- Drevet, B. and N. Eustathopoulos (2012). "Wetting of ceramics by molten silicon and silicon alloys: a review." Journal of Materials Science 47(24): 8247-8260.
- Candan, E., et al. (2011). "Wettability of Aluminum–Magnesium Alloys on Silicon Carbide Substrates." Journal of the American Ceramic Society 94(3): 867-874.

- Dezellus, O. and N. Eustathopoulos (2010). "Fundamental issues of reactive wetting by liquid metals." Journal of Materials Science 45(16): 4256-4264.
- Mortensen, A., et al. (1997). "Kinetics of diffusion-limited spreading of sessile drops in reactive wetting." Scripta Materialia 36(6): 645-651.
- Warren, J. A., et al. (1998). "Modeling reactive wetting." Acta Materialia 46(9): 3247-3264.
- Voytovych, R., et al. (2007). "Reactive vs non-reactive wetting of ZrB 2 by azeotropic Au–Ni." Acta Materialia 55(18): 6316-6321.
- Yin, L., et al. (2009). "Reactive wetting in metal–metal systems." Journal of Physics: Condensed Matter 21(46): 464130.
- Dezellus, O., et al. (2002). "Chemical reaction-limited spreading: the triple line velocity versus contact angle relation." Acta Materialia 50(19): 4741-4753.
- Calderon, N. R., et al. (2010). "Wetting dynamics versus interfacial reactivity of AlSi alloys on carbon." Journal of Materials Science 45(8): 2150-2156.
- Lee, J.-I., et al. (2003). "Reactive wetting between molten Sn-Bi and Ni substrate." Journal of Electronic Materials 32(3): 117-122.
- Neumann, A. W., and R. J. Good. "Thermodynamics of contact angles. I. Heterogeneous solid surfaces." Journal of Colloid and Interface Science 38, no. 2 (1972): 341-358.
- Song, X., Bian, X., Zhang, J., Zhang,J. (2009). "Temperature-dependent viscosities of eutectic Al–Si alloys modified with Sr and P." Journal of Alloys and Compounds 479(1): 670-673.
- Neumann, A. W., and R. J. Good. "Thermodynamics of contact angles. I. Heterogeneous solid surfaces." Journal of Colloid and Interface Science 38, no. 2 (1972): 341-358.
- Eustathopoulos, N., et al. (2005). "Measurement of contact angle and work of adhesion at high temperature." Journal of Materials Science 40(9-10): 2271-2280.
- Hawksworth D.K., Sekulic D.P., Yu C.-N., Fu H., Westergard R.G.J., “A Mechanistic Study of Aluminium Controlled Atmosphere Brazing Processes”, (May

10-13, 2015) Vehicle Thermal Management Systems Conference and Exhibition-VTMS 12, Nottingham, England

- http://www.coorstek.com/markets/electronic_equipment/ceramic-substrates.php, Contact: aabeyta@coorstek.com
- http://www.uky.edu/design/index.php/info/category/digital_fabrication/
- Stalder, A. F., et al. (2010). "Low-bond axisymmetric drop shape analysis for surface tension and contact angle measurements of sessile drops." Colloids and Surfaces A: Physicochemical and Engineering Aspects 364(1–3): 72-81.
- Drop Shape Analysis. http://bigwww.epfl.ch/demo/dropanalysis/
- Anson, J. P., et al. (1999). "The surface tension of molten aluminum and Al-Si-Mg alloy under vacuum and hydrogen atmospheres." Metallurgical and Materials Transactions B 30(6): 1027-1032.
- Dorsey, N. E. (1928). A new equation for the determination of surface tension from the form of a sessile drop or bubble. *J. Wash. Acad. Sci*,*18*(19), 505-509.
- T. Iida, R.I.L. Guthrie, The Physical Properties of Liquid metals, Oxford Science Publications, Oxford, 1988.
- J.F. Paddy. "Surface Tension. Part II. The Measurement of Surface Tension." In Surface and Colloid Science. Vol.1. Editted by E. Matijevic. Wiley, New York, 1968.
- Kwok, D. Y. and A. W. Neumann (2000). "Contact angle interpretation in terms of solid surface tension." Colloids and Surfaces A: Physicochemical and Engineering Aspects 161(1): 31-48.
- Goicoechea, J., et al. (1992). "Surface tension of binary and ternary aluminium alloys of the systems Al-Si-Mg and Al-Zn-Mg." Journal of Materials Science 27(19): 5247-5252.
- Aqra, F. and A. Ayyad (2012). "Surface tension (γLV), surface energy (γSV) and crystal-melt interfacial energy (γSL) of metals." Current Applied Physics 12(1): 31-35.
- Keene, B. J. (1993). "Review of data for the surface tension of pure metals." International Materials Reviews 38(4): 157-192.

- Sarou-Kanian, V., et al. (2003). "Surface Tension and Density of Oxygen-Free Liquid Aluminum at High Temperature." International Journal of Thermophysics 24(1): 277-286.
- Mills, K. C. and Y. C. Su (2006). "Review of surface tension data for metallic elements and alloys: Part 1 Pure metals." International Materials Reviews 51(6): 329-351.
- Skapski, A. S. (1956). "A theory of surface tension of solids—I application to metals." Acta Metallurgica 4(6): 576-582.
- Su, Y., et al. (2005). "A model to calculate surface tension of commercial alloys." Journal of Materials Science 40(9-10): 2185-2190.
- Naidich, Y. V., et al. (1998). "The wettability of silicon carbide by Au–Si alloys." Materials Science and Engineering: A 245(2): 293-299.
- Eustathopoulos, N., et al. (1974). "The wetting of carbon by aluminium and aluminium alloys." Journal of Materials Science 9(8): 1233-1242.
- Flint, O. (1965). "Surface tension of liquid metals." Journal of Nuclear Materials 16(3): 233-248.
- Zhivov, I. V. G. "Determination of surface tension of molten aluminum, magnesium, sodium, and potassium." Tr. Vses. alyumino-magn, in-ta 14 (1937): 99.
- Martins, G. P., D. L. Olson, and G. R. Edwards. "Modeling of infiltration kinetics for liquid metal processing of composites." Metallurgical and Materials Transactions B 19.1 (1988): 95-101.
- Utigard, T. and J. M. Toguri (1985). "Interfacial tension of aluminum in cryolite melts." Metallurgical Transactions B 16(2): 333-338.
- Alchagirov, B. B., et al. (2003). "The Surface Tension of Melts of Aluminum–Indium Binary System." High Temperature 41(4)
- Alonso, A., et al. (1993). "Evaluation of the wettability of liquid aluminum with ceramic particulates (SiC, TiC, AI2O3) by means of pressure infiltration." Metallurgical Transactions A 24(6): 1423-1432.
- Hatch, John E. Aluminum: properties and physical metallurgy. Vol. 1. Asm International, 1984.

- T. Iida, R.I.L. Guthrie, The Physical Properties of Liquid metals, Oxford Science Publications, Oxford, 1988.
- Rhee, S. K. "Wetting of ceramics by liquid aluminum." Journal of the American Ceramic Society 53.7 (1970): 386-389.
- Hashim, J., et al. (2001). "The wettability of SiC particles by molten aluminium alloy." Journal of Materials Processing Technology 119(1–3): 324-328.
- Goumiri, L., et al. "Tensions superficielles d'alliages liquides binaires présentant un caractère dimmiscibilité: Al-Pb, Al-Bi, Al-Sn et Zn-Bi." Surface Science 83.2 (1979): 471-486.
- ES Levin, GD Ayushina, High Temp., 1968, vol. 6, p. 416
- Andreas, J. M., E. A. Hauser, and W. B. Tucker. "BOUNDARY TENSION BY PENDANT DROPS1." The Journal of Physical Chemistry 42.8 (1938): 1001-1019.
- s. I. POPEL, V. N. KOZHURKOV, and A. A. ZHUKOV: Izv. Akad.Nauk SSSR, Met., 1975, (5), 69.
- Iida, T. and R. Guthrie (2009). "Performance of a Modified Skapski Model for the Surface Tension of Liquid Metallic Elements at Their Melting-Point Temperatures." Metallurgical and Materials Transactions B 40(6): 967-978.
- Egry, I., et al. "Surface tension measurements of high temperature metallic melts." TRANSACTIONS-JWRI 30.SPI (2001): 195-200.
- Goumiri, L. and J. C. Joud (1982). "Auger electron spectroscopy study of aluminium-tin liquid system." Acta Metallurgica 30(7): 1397-1405.
- Pamies, The measurement of surface tension of liquid aluminum by means of the maximum bubble pressure method: the effect of surface oxidation, 1984
- Lu, H. M. and Q. Jiang (2005). "Surface Tension and Its Temperature Coefficient for Liquid Metals." The Journal of Physical Chemistry B 109(32): 15463-15468.
- Liu, W., Lu L., Li, Y., Cai, Y., Sekulic, D.P. (2012). Preferential spreading of molten metal over an anisotropicallymicrostructured surface. EPL (Europhysics Letters) 97(4): 46003.
- Lowengrub, J, Truskinowsky, L. 1998 Quasi-incompressible Cahn-Hilliard fluids and topological transition. *Proc. R. Soc. Lond. A* 454, 2617-2654.

- Jacqmin, D. 2000 Contact-line dynamics of a diffuse fluid interface. *J. Fluid Mech.* 402, 57-88.
- Gao, F., Zhao, H., Sekulic, D.P., Qian, Y., Waller, L., (2002), "Solid state Si diffusion and joint formation involving aluminum brazing sheet", Materials Science and Engineering, A337: 228-235

VITA

Hai Fu

Education

- MSME, 2008
  Refrigeration and Cryogenics Engineering, Shanghai Jiao Tong University, Shanghai, China
- BSME, 2005
  Refrigeration and Cryogenics Engineering, Southeast University, Nanjing, Jiangsu, China

Research Experience

- Research Assistant/Teaching Assistant (University of Kentucky, 2012-Present)
- Research Assistant/Teaching Assistant (University of Cincinnati, 2009-2011)

Certification

- Advanced-Level English Interpretation Accreditation of Shanghai HR Credentials for Special Expertise, The Organization Department of the CPC Shanghai Committee, The Shanghai Municipal Personnel Bureau, The Shanghai Education Commission and The Shanghai Adult Education Commission. License Number: D19739. 2007

Journal Publications

1. Fu H., Dehsara M., Krivilyov M., Sekulic D.P., Mesarovic S.Dj., "Kinetics of the Molten Al-Si Triple Line Movement during a Brazed Joint Formation", Journal of Material Science, 2016, 51(4), 1798-1812.
2. Dehsara, M, Fu, H, Mesarovic, S Dj, Sekulic, DP & Krivilyov, Phase-field models for capillary flows. Submitted, April 2016 to Journal of Computational Physics
3. D. P. Sekulic, H. Fu, A. Rabinkin, D. Busbaher, E. Leone, T. Preuss, "Microstructure Refining of a Mo-Ni Brazing Filler Metal by a SiC Nanoparticles Doping", Welding Journal, submitted, 2016
4. Sekulic, Dusan P., Rahul Nehete, Cheng-Nien Yu, and Hai Fu. "An energy sustainability metric." Energy 74 (2014): 37-44.
5. Hai Fu, Jingyi Wu, Ru-zuo Wang, "Experimental Analysis on Heat and Power Supply Performance of Movable Miniature CCHP System", Energy Technology, 2008, Vol. 29(2), p79-82.

Conference Proceedings

1. Winter, M., Bickel, R., Sekulic, D., Koch, H., Fu, H., Butler, B. “Spectral, Directional Emittance at Elevated Temperature for Various Materials”, AIAA Science and Technology Forum and Exposition (SciTech 2016), accepted, 4-8, Jan, 2016.
2. Dehsara M., Mesarovic S.Dj., Fu H., Sekulic D.P., Krivilyov M., “Kinetics of the Molten Metal Triple Line Movement: Phase Field Models and Experiments”, International Conference on High Temperature Capillarity HTC-2015, May 17-21, 2015, Bad-Herrenalb, Germany.
3. D.P. Sekulic, H. Fu, A. Rabinkin, D. Busbaher, E. Leone, and T. Preuss, “Positive Changes in the Mocrostructure Morphology of the Mo-Ni Eutectiv Brazing Filler Metal Caused by Additions of SiC Nano-Particle Powder”, International Brazing and Soldering Conference 2015, AWS, ASM, Pap. 0477-000059, Apri 19-22, 2015, Long Beach, USA
4. D.P. Sekulic, H. Fu, A. Rabinkin, D. Busbaher, E. Leone, and T. Preuss, “Mechanical Properties of Mo Joints Brazed Using Mo-Ni Brazing Filler Metal Powder Doped by SiC Nano-Particles”, International Brazing and Soldering Conference 2015, AWS, ASM, Pap. 0477-000058, pp. 1-6, Apri 19-22, 2015, Long Beach, USA
5. Hawksworth D.K., Sekulic D.P., Yu C.-N., Fu H., Westergard R.G.J., “A Mechanistic Study of Aluminium Controlled Atmosphere Brazing Processes”, Vehicle Thermal Management Systems Conference and Exhibition-VTMS 12, May 10-13, 2015, Nottingham, England.
6. Fazleena Badurdeen, Dusan Sekulic, Robert Gregory, Adam Brown, Hai Fu, “Developing and Teaching a Multidisciplinary Course in Systems Thinking for Sustainability: Lessons Learned through Two Iterations”, “Best Paper Award”: 121st ASEE Annual Conference & Exposition, June 15-18, 2014, Indianapolis, IN, USA
7. Hai Fu, Fangxiao Dong, D P. Sekulic, S. Dj. Mesarovic, M. Krivilyov, "Surface Tension Driven Kinetics of the Triple Line of a Liquid Metal Free Surface", IMECE2013-62945, ASME 2013 International Mechanical Engineering Congress & Exposition, November 13-21, 2013, San Diego, California, USA.
8. Rahul Nehete, Cheng-Nien Yu, Hai Fu, Dusan P. Sekulic, “Energy Resource Use: Sustainability Metric of a Manufacturing Process”, 26th International Conference on Efficiency, July 16-19, 2013, Guilin, China.
9. Fazleena Badurdeen, Robert Gregory, Gregory Luhan, Margaret Schroder, Dusan Sekulic, Leslie Vincent, Adam Brown, Hai Fu, “Experiences from Developing and Teaching a Multi-disciplinary Course”, Kentucky Innovations Conference, May 16-17, 2013, Lexington, Kentucky, USA.
10. Badurdeen, F., A. Brown, R. Gregory, H. Fu, M. Schroeder, D. Sekulic, L. Vincent, and G. A. Luhan. "Reframing Interdisciplinary Approaches to Systems Thinking for Sustainability." In Proceedings of the International Symposium on Sustainable Systems & Technologies. 2013.
11. Hai Fu, D P. Sekulic, Triple Line Kinetics of Liquid Metal Free Surface Poster,

Forum on Sustainable Manufacturing, August 9th, 2013, Lexington, Kentucky, USA.
12. Sang Young Son, Jae Yong Lee, Hai Fu, Sushant Anand, Francisco Romay, Aaron Collins, “Personal and Wearable Ultrafine Particle Counter”, AAAR 30th Annual Conference, October 3-7, 2011, Orlando, Florida, USA.